Theory and Simulation of Texture Formation in Mesophase Carbon Fibers

by

Jun Yan

Department of Chemical Engineering
Mcgill University, Montreal, Canada

Date: June 3, 2001

A Thesis submitted to the Faculty of Graduate Studies and Research in Partial fulfiment of the requirements for the degree of Master of Science

National Library
of Canada

Acquisitions and
Bibliographic Services

395 Wellington Street
Ottawa ON K1A 0N4
Canada

Bibliothèque nationale
du Canada

Acquisitions et
services bibliographiques

395, rue Wellington
Ottawa ON K1A 0N4
Canada

Your file Votre référence

Our file Notre référence

0-612-79104-1

Canada

To my parents and sister

Abstract

Carbonaceous mesophases are discotic nematic liquid crystals that are spun into high performance carbon fibers using the melt spinning process. The spinning process produces a wide range of fiber textures and cross-sectional shapes. The circular planar polar (PP), circular planar radial (PR), ribbon planar radial (RPR), and ribbon planar line (RPL) textures are the most frequently observed in industrial fiber making. This thesis presents, solves, and validates models of mesophase fiber texture formation based on the classical Landau-de Gennes theory of liquid crystals, adapted here to carbonaceous mesophases. The model captures the microstructure and the formation of the four (PP, PR, RPR, RPL) textures. In cylindrical fibers, the computed PP and PR textures phase diagram, given in terms of temperature and fiber radius, establishes the processing conditions and geometric factors that lead to the selection of these textures. The influence of elastic anisotropy to the textures' formation and structure is thoroughly characterized. The multi-stage formation process of the PP texture is reproduced, including defect nucleation, defect migration, and overall texture geometry. The mechanisms that control the PP texture geometry are characterized using analytical methods. The role of elasticity and flow-induced orientation on texture selection mechanism in ribbon-shaped mesophase fibers are characterized using an anisotropic viscoelastic model. The model is able to predict the formation of the commonly observed line defect in the RPL texture, and the fine structure of the line is reproduced and explained in terms of classical liquid crystal defect physics. The results of this thesis provide new knowledge on how to optimize and control mesophase fiber textures.

RÉSUMÉ

Les mésophases carboniques sont des cristaux liquides nématiques distiques, utilisés pour la fabrication des fibres de carbones à haute performance en utilisant le procédé d'extrusion. Le procédé d'extrusion produit une gamme variée des textures des fibres et des différentes formes des sections transversales. Les textures circulaires planaires polaires (PP), circulaires planaires radiales (PR), les textures ruban planaires radiales (RPR), et ruban planaires ligne (RPL) sont très répandues. Cette thèse pressent, résolut et valide les modèles pour la formation des textures de fibres de mésophases, basés sur la théorie classique Landau-deGennes pour cristaux liquides, adaptée dans ce cas pour l'étude des mésophases carboniques. Dans les fibres cylindriques, les diagrammes des phases pour les textures PP et PR données en fonction de la température et du rayon de la fibre, sont présentées pour déterminer les conditions du procédé et les facteurs géométriques conduisant à une certaine sélection de la texture. L'influence de l'anisotropie élastique sur la formation et la structure des textures est aussi étudiée. Le procédé de la formation de texture PP est très bien reproduit, en incluant l'apparition des défauts, la dynamique des défauts et la géométrie de la texture. La géométrie calculée de la texture PP est très bien expliquée à l'aide des méthodes analytiques. Aussi on caractérise le rôle de l'élasticité et de l'orientation induite par l'écoulement sur le mechanism de sélection de la texture ruban. Ce modèle est capable prédire la formation de la texture ligne observée souvent dans la texture RPL. La structure fine de cette ligne est reproduite et expliquée en fonction de la physique classique des défauts du cristal liquide. Les résultats obtenus apportent des nouvelles connaissances dans le domaine de l'optimisation et du control des textures des mésophases carboniques.

Acknowledgements

It is with great pleasure that I express my gratitude to my research supervisor, Professor Alejandro D. Rey, for his sincere research guidance, continuous support and encouragement throughout the course of this thesis and my graduate studies. I will always be indebted regarding what I learnt from him about dedication, perseverance and hard work. His continuous strive to teach me "by example" on how to be a good researcher, and kindness are highly appreciated.

I would like to extend my appreciation to the followings:

My parents and sister for their love, support, encouragement.

Researchers in the Complex Fluids/Computational Materials Research group: Dana Grecov Radu, Ae-Gyeong Cheong, Gino de Luca, Luiz R. P. de Andrade Lima, Susanta K. Das, Dinesh Sharma for their help, lively discussion, and most of all making theoretical research an enjoyable experience.

The Donors of Petroleum Research Fund (PRF), administered by the American Chemical Society, for support of this research.

Contents

List of Figures

List of Tables

Nomenclature

$\mathbf{n}$	Unit vector indicate the director in liquid crystals	---
θ	The angle between director and unit normal of disc-like molecular orientation angle (chapter 5)	---
f_n	Free energy density of nematic liquid crystals	$J{\cdot}L^{-3}$
K_{11}, K_{22}, K_{33}, K_{24}	Frank elastic constants	$J{\cdot}L^{-1}$
ϕ	Director angle in the certain coordinate	---
α	Position angle with respect to the x axis	---
s	Defect strength	---
W	The energy of deformation of an isolated disclination in a circular layer of radius R and of unit thickness	$J{\cdot}L^{-1}$
W_c	The energy of the central defect region	$J{\cdot}L^{-1}$
r_c	The radius of defect core	---
$\mathbf{Q}$	Tensor order parameter.	---
S	Uniaxial scalar order parameter	---
P	Biaxial scalar order parameter	---
$\mathbf{m}$, $\mathbf{l}$	Biaxial director	---
f_0	Free energy density of the isotropic state	$J{\cdot}L^{-3}$
f_s	Short-range free energy density	$J{\cdot}L^{-3}$
f_ℓ	Long-range free energy density	$J{\cdot}L^{-3}$
f_s^*	Dimensionless short-range free energy density	Dimensionless
$f_{\ell 2}^*$	Dimensionless 2nd order long-range free energy density	Dimensionless
$f_{\ell 3}^*$	Dimensionless 3rd order long-range free energy density	Dimensionless
A, B, C	Coefficients of short-range energy density expression	$J{\cdot}L^{-3}$

L_1, L_2, L_3	Coefficients of long-range energy density expression	$J \cdot L^{-1}$
$\gamma(\mathbf{Q})$	Rotational viscosity coefficient	$J \cdot s \cdot L^{-3}$
c	Number density of the discs	L^{-3}
k	Boltzmann constant	$J \cdot T^{-1}$
T^*	Reference temperature below the phase transition temperature	T
T^+	Reference temperature above the phase transition temperature	T
U	Dimensionless temperature $3T^*/T$	Dimensionless
$\varphi_i(i=1,2,3)$	Basis functions in finite element method	---
a_i, b_{ij}, c_i, c_i^*	Known coefficients of adaptive time integration	---
Δ	Error in adaptive time integration (chapter 2) Dissipation function (chapter 5)	---
h	Time step	---
$\mathbf{I}$	3×3 Unit matrix	---
R	Fiber radius	L
$\mathbf{S}$	Short-range contribution	---
$\mathbf{L}$	Long-range contribution	---
$\overline{D_r}$	Microstructure dependent rotational diffusivity	s^{-1}
D_r	Isotropic diffusivity	s^{-1}
η	Viscosity	$J \cdot s \cdot L^{-3}$
t^*	Dimensionless time	Dimensionless
ξ	Molecular length scale	L
$\tilde{L}_2$, $\tilde{L}_3$	Dimensionless elastic coefficients	Dimensionless
$\mathcal{R}$	Dimensionless fiber radius	Dimensionless
$\mathcal{R}_c$	Critical dimensionless fiber radius	Dimensionless
τ_i, τ_e, τ_f	Internal time scale, external time scale, external flow time scale	s
L_i, L_e	Internal length scale, and external length scale	L

F^*	Total dimensionless free energy density	Dimensionless
F	Total free energy density	$J\cdot L^{-3}$
A^*	Area of the computational domain	---
μ_n, μ_m, μ_l	Eigenvalues of **Q** on **n**, **m**, and **l** direction	L^2
b^*	Dimensionless distance along a line that is perpendicular to the line connecting the two +1/2 defects and goes through one of the two equivalent defects	Dimensionless
φ	Orientation angle	---
x	Distance between defect and fiber center	Dimensionless
ℓ	Distance between the origin and the image of each defect	Dimensionless
d^*	Dimensionless defects separation distance The thickness of inversion wall (chapter 5)	Dimensionless
ε	Dimensionless elastic anisotropy	Dimensionless
$\mathcal{F}_{12}$	The force between two +1/2 defects	$J\cdot L^{-1}$
$\mathbf{v}$	Velocity	$L\cdot s^{-1}$
$\mathbf{t}^s$	Stress tensor	$J\cdot L^{-3}$
$\mathbf{W}$	Vorticity tensor	s^{-1}
$\mathbf{H}$	Molecular field	---
$\mathbf{A}$	Deformation tensor	s^{-1}
$\mathbf{F}$	Flow contribution	---
D_e	Deborah number	Dimensionless
$\dot{\gamma}$	Characteristic deformation rate	s^{-1}
A_r	Aspect ratio of the ribbon fiber	---
β	Molecular shape factor	---
λ	Reactive parameter	---
γ_1, γ_2	Rotational viscosity, and irrotational torque coefficient	$J\cdot s\cdot L^{-3}$
θ_L	Leslie angle	---

$\dot{\varepsilon}$	Deformation rate	---
ψ	Position angle (chapter 5)	---
E_e	The dimensionless ratio of flow effect to elastic effect	Dimensionless

Chapter 1

Introduction

1.1 Thesis Motivation

High performance mesophase carbon fibers are often used as reinforcing agents for polymers, ceramics, and metals in future generations. They exhibit ultra high Young's modulus, low density, extremely large thermal conductivity, and negative coefficient of expansion [1]. The superior set of product property profile of mesophase carbon fibers depends on their microstructure which emerges during the fiber melt spinning process. The melt spinning process and the mesophase carbon fiber microstructure are a strong function of the operating conditions, the geometry, and the material properties [1]. There has been a great interest in understanding the texture evolution during the fiber formation melt spinning process, in which the carbonaceous mesophases are subjected to non-homogeneous mixed shear and extensional flows, with the aim of controling and optimizing the product property profile. Figure 1.1 shows thermal conductivity and electrical resistivity for a number of metals and Amoco series of mesophase pitch-based (suffix "P") and PAN-based (polyacrylonitrile) carbon fibers [2]. The thermal conductivity of mesophase carbon fibers is considerably higher than that of copper and PAN carbon fibers, which is due to the inherent graphitic crystallinity in the well ordered textures of the mesophase carbon fibers. On the other hand, the lack of extended structure makes PAN-based carbon fibers less flaw-sensitive, allowing them to develop higher tensile strengths than mesophase pitch-based carbon fibers (see fig.2). Therefore while PAN is the preferred precursor for the carbon fibers used in structural composites [3], mesophase pitch is the superior precursor for carbon fibers used in composites and printed-circuit substrates when heat transfer is critical. This thesis focuses on the study of mesophase pitch-based carbon fiber.

Although during the past decade some important advances have been made in understanding polymer melt viscoelasticity, relatively less is known for material systems that include mesophases such as liquid crystals. The present theories of polymer melt rheology need to be extended to include liquid crystals to further our understanding of the underlying principles governing microstructure-viscoelasticity responses, and thus to ultimately improve product property-profiles. Modeling and simulation provides economical research alternatives to more expensive and time-consuming experimental work, and it’s employed in this thesis to understand the microstructural behavior of carbonaceous mesophase, a liquid crystal currently being employed to manufacture high performance carbon fiber.

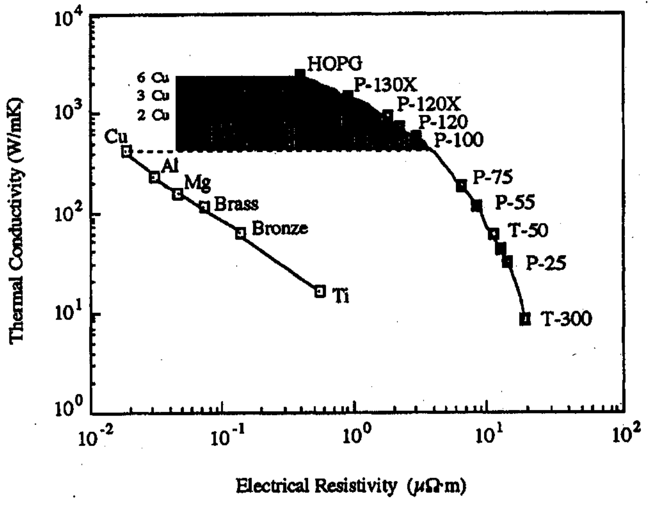

Figure 1.1: thermal conductivity versus electrical resistivity product property phase plane for various metals and carbon fibers. The thermal conductivity of mesophase carbon, P-130X, P-120X etc., is considerably higher than that of the most conductive metals like copper. Adapted from [2]

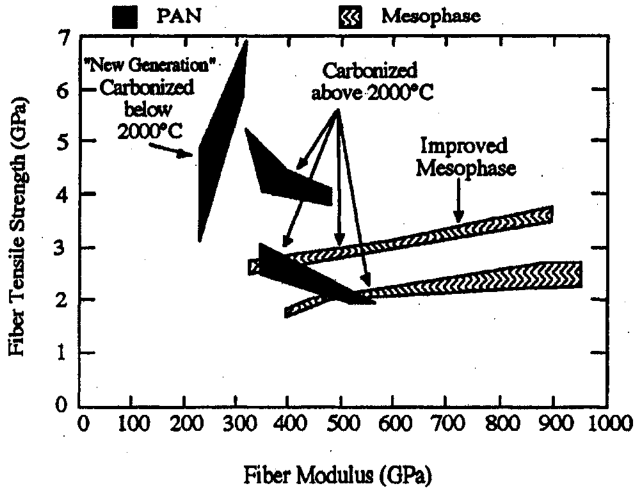

Figure 1.2: tensile strength versus modulus of elasticity (stiffness) product property phase plane of various carbon fibers. The PAN-based carbon fibers have considerably in terms of stiffness. The stiffness of mesophase carbon fibers reaches the theoretical limits of pure graphite. Adapted from [3].

1.2 Introduction of Liquid Crystals

For many organic compounds the phase transition between the solid state and liquid state is not simple phase transition, and an intermediate state called mesophase (i.e. intermediate phase) exists between solid and liquid [4,5,6]. Mesomorphic materials possess both liquid-like fluidity and solid like molecular order. Based on the partial ordering two basically different types of mesophases have been observed. The first type shows a transition from a strongly ordered state to a phase where each molecule commutes between several equivalent orientations. The positional order is still present but the orientational order has disappeared or is strongly reduced, and this phase is called disordered crystal mesophase or plastic crystal [4]. The second type shows a low temperature phase where the positional order is reduced or even completely absent but exhibits long orientatonal order. The phase is called ordered fluid mesophase or liquid crystal [4]. Materials, which form a stable liquid crystalline phase, are, in general, composed of relatively rigid anisotropic molecules. At higher temperature, liquid crystals undergo a transition to a conventional (isotropic) liquid. The shape of the molecule is an important factor for mesomorphism to occur. Two main types of liquid crystals compounds characterized by the shape of their molecules are most widely studied [5], the rod-like crystals and disk-like liquid crystals, also known as discotic liquid crystals, which are studied in this thesis.

1.2.1 Classification of Liquid Crystals

Two main methods are used to classify the liquid crystals: based on their physical composition or behavior (i.e. thermotropic and lyotropic) and based on the molecular order or orientation (nematic, cholesteric, smectic). There are two other classifications based on the qualitative differences in the molecules: shape of molecules (rod-like, disc-like) and weight of the constitutive molecules (polymeric liquid crystals and low molecular weight liquid crystals).

1.2.1.1 Classification based on physical composition or behavior

(a) Thermotropic liquid crystals

Single component systems that show mesomorphic behaviors in a definite temperature range are called thermotropic liquid crystals, which are primarily associated with low molecular weight liquid crystals [4]. Every molecule in the thermotropic liquid crystalline participates in the long range ordering. This kind of LC is of interest for applications in electro-optical displays, temperature and pressure sensors, etc.. Most computer and watch displays use mixture of low molecular weight liquid crystals, such as 8CB(p-octyl-p'-cyanobiphenyl).

(b) Lyotropic liquid crystals

Lyotropics show mesomorphic behavior in solution and are usually the solutions of rigid, high molecular weight molecules in various solvents, in which the concentration (rather than temperature) is the main force of the mesophase formation [4]. A well-known example is Kevlar, which is the solution of (poly-p-phenylene terepthalmide) in sulphuric acid. The temperature range in which lytropics exist is mainly determined by the rod-like molecules (solute). Lyotropic liquid crystals are of great interest biologically and appear to play an important role in living systems.

1.2.1.2 Classification based on structure or arrangement of molecules

(a) Nematic order

Figure 1.3 shows the schematic representation of the nematic phase. The molecules tend to align parallel to each other and along some common axis called director **n**, which is a unit vector (**n**·**n**=1) and gives the average preferred orientation. Long-range orientational order and cylindrical (or uniaxial) symmetry are exhibited by this liquid crystalline phase. The centers of gravity of the molecules are distributed at random. Thus they show orientational order like crystals and positional disorder like viscous fluid.

The degree of alignment of the individual molecules along the director **n** is given by a scalar known as scalar order parameter S [4,5,6]:

$$S = \left\langle \frac{3}{2}\cos^2\theta - \frac{1}{2} \right\rangle \tag{1.1}$$

where θ is the angle between the director **n** and the long axis of each rod-like molecule in the rod-like nematics, and between the director **n** and unit nomal of disc like molecule in discotic nematics. The brackets denote an average over all of the molecules in the sample. For isotropic liquid, the order parameter $S \to 0$, and for a perfect ordering $S \to 1$. Typical values for the order parameter of a liquid crystal range between 0.3 and 0.9.

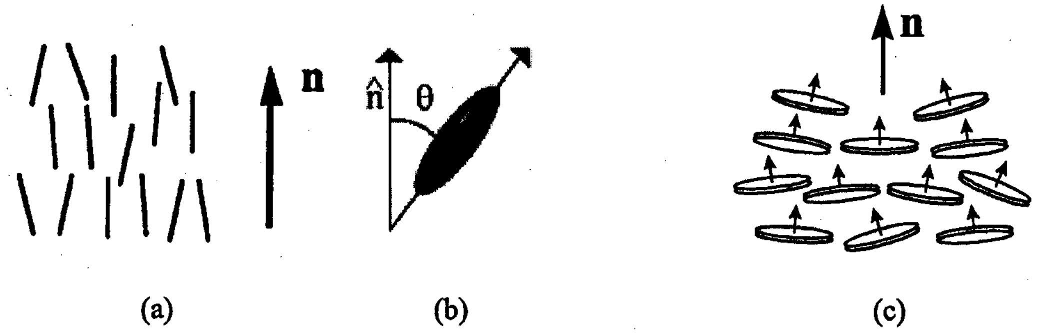

Figure 1.3: Schematic representation of (a) rod-like nematic liquid crystals, and (c) discotic nematic liquid crystals. The director **n** represents the average preferred orientation of the molecules for (b) rod-like nematics, whereas in discotic nematics **n** is the average preferred orientation of the unit normals to the disc-like molecules. The molecular degree of alignment is given by scalar order parameter S, which is a measure of alignment of individual molecule along the director **n**. Adapt from [7].

(b) Cholesteric order

Figure 1.4 shows the schematic of the equilibrium structure of the cholesteric phase. The lack of long-range translational order imparts fluidity to the cholesteric phase. On a local scale, the cholesteric order is similar to the nematic order, since the molecules tend to align along the director **n**. on a larger scale, the cholesteric director follows a helical path as shown.

(c) Smectic order

A smectic phase (see fig. 1.5) has, in addition to the orientation order of nematics and cholesterics, a single degree of translational order, which results in a layered structure. Smectics phases always occur at temperatures below the nematic range, since they are more ordered. In smectic ordering, the molecules are tilted away from the normal in each layer [6]. The layer spacing is of the order of 20 Å [6].

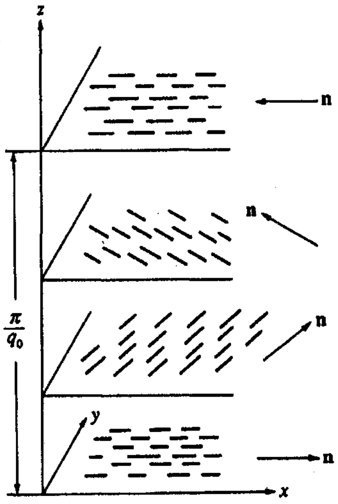

Figure 1.4: schematic arrangement of rod-like molecules in a cholesteric liquid crystalline phase. The localized director **n** follows a helical trajectory along the z-axis. Note that the successive planes are drawn for convenience, and don't have any physical meaning. Adapted from [6].

1.3 Carbonaceous Pitches (Mesophase Pitches)

In the production of commercial mesophase carbon fiber, carbonaceous mesophase (CM) or mesophase pitch (MP) is the usual raw material. It is a uniaxial discotic nematic liquid crystal thermodynamically stable phase, which forms during the liquid phase pyrolysis of coal or petroleum pitches [8]. Figure 1.6 shows the thermodynamic and structural changes brought by heating a non-volatile organic compound, such as coal or petroleum pitch. In the absence of air, the organic component melts in heating and becomes an isotropic pitch or liquid. As the temperature rises over 350°C, optically anisotropic spheres, known as spherules, appear in the isotropic matrix [9,10]. The formation of the carbonaceous mesophase follows a nucleation and growth process. Attractive forces among the spherules give rise to droplet coalescence and overall growth of the mesophase. As the polymerization reactions continue, the molecules get larger and the mesophase becomes more viscous. The transformation was observed first by Brooks and Taylor in 1965 as an intermediate phase of spherules with a mosaic structure [11]. The droplets or spherules are easily observed because of their optical anisotropy. Selected area electron diffraction patterns indicated that each mesophase spherule possesses at its center a single direction of preferred orientation. During the pyrolysis, the spherules grow, due to growth of the aromatic molecules, and coalesce until a phase inversion takes place, after which the mesophase becomes the continuous phase. The characteristic mesophase mechanism, which is involved in establishing the mesophase morphology, is spherule precipitation, coalescence of spherules to form a bulk mesophase, and distortion of mesophase by mechanical deformations.

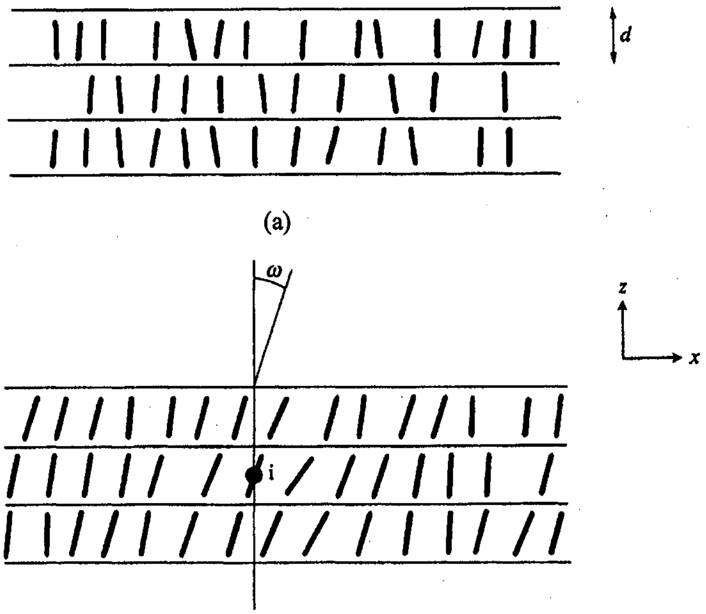

(a)

(b)

Figure 1.5: Schematic arrangement of rod-like molecules in (a) Smectic A, and (b) Smectic C liquid crystalline phases. The shown smectic phases have 2-D layered structure. In smectic C phase the constituting molecules are tilted at an angle ω normal to the smectic plane. Adapted from [6].

Besides the pyrolysis of aromatic pitch, different methods, such as solvent extraction and supercritical fluid extraction, have been employed by a number of researchers [14] worldwide to produce mesophase pitches with few impurities, which result in carbon fibers with superior properties. Recently mesophase pitch has also been prepared by catalytic polymerization of synthetic precursors, such as naphthalene or methylnaphthalene[15]. However, the resulting mesophase pitch, derived from all of these processes, consists of aromatic disc-like molecules exhibiting discotic liquid crystalline properties.

The carbonaceous mesophase consists of disc-like molecules (fig.1.7) that display long-range orientational order, so that the molecules lie approximately parallel to each other with no point-to-point registry between adjacent molecules. A schematic model of carbonaceous mesophase stacking in the bulk is given in figure 1.8. The model suggests that the stacking size and the possible shapes of the disc like molecules may be quite irregular and that the material may have vacant sites and holes.

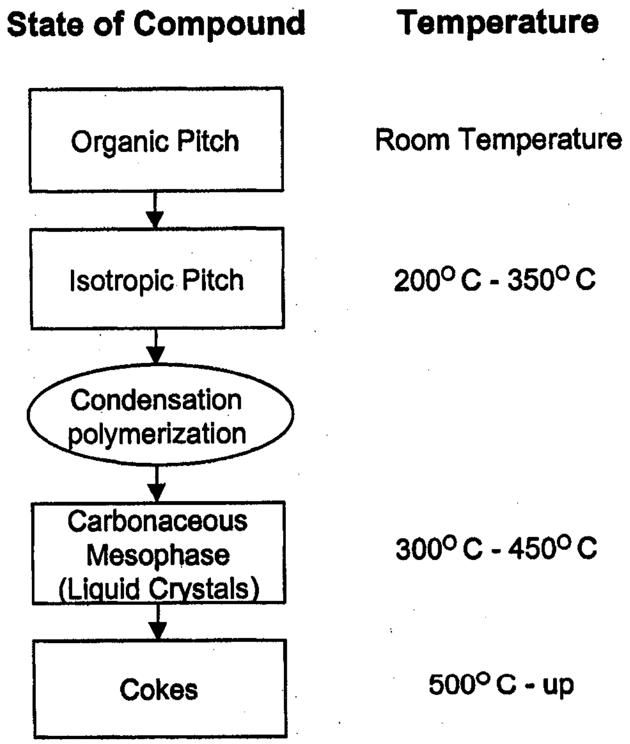

Figure 1.6: changes in the non-volatile organic compounds like coal or petroleum pitches brought about by heating in the absence of air. Adapted from [13].

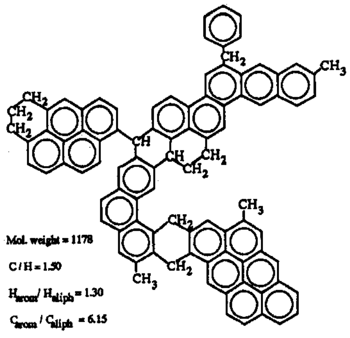

Figure 1.7: Typical molecule of a heat soaked mesophase pitch. Adapted from [12].

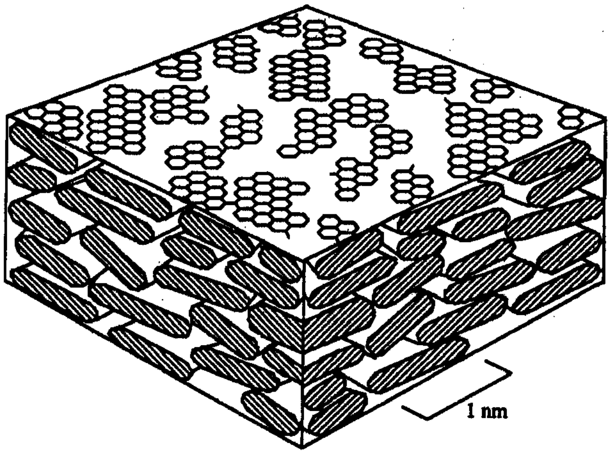

Figure 1.8: schematic model representing stacking arrangement of polyaromatic molecules in carbonaceous mesophases or mesophase pitches. The disc-shaped molecules lie more or less parallel to each other. Adapted from [10].

1.4 Processing of Carbonaceous Mesophases

Mesophase carbon fibers are manufactured from mesophase pitch in mainly three steps: melt spinning, stabilization and heat treatment. In the melt-spinning step, the fibers are drawn using the molten mesophase pitch to achieve preferred orientation in the as-spun fibers [1]. Some types of cross-section texture of carbon fibers can be seen in the process. The texture depends on a number of variables such as the composition of the pitch, the spin temperature, whether or not the melt pool is stirred, the geometry of the orifice, etc [1, 16]. These textures across the fiber diameter can be random, radial, and radial with a wedge like crack in the length of the fiber. onion skin, oriented core, or mixtures of these textures across a fiber radius may also be appeared.

The melt-spinning process used to convert mesophase pitch into fibers is essentially similar to that used for thermotropic polymers. Figure 1.9 shows the schematic representing the different steps [1] used in the manufacturing of mesophase pitch-based carbon fiber. Typically the precursor is melted in an extruder, and which then pumps the melt into the spin pack. The molten pitch is then filtered, to remove solid impurities, before being extruded through a multi-holed spinneret. The pitch is subjected to high extensional shear stresses as it approaches and flows through the spinneret capillaries. The associated flow-induced torque tends to orient the disk-shaped molecules in a regular transverse pattern. Upon emerging from the spinneret capillaries, the as-spun fibers are drawn to improve axial orientation and are collected on a wind–up device.

After the MP is formed into fibers, it must then be stabilized to prevent the fibers from melting or fusing together during the high temperature heat treatment required to form carbon fibers of high strength and modulus. The as-spun fiber has low strength and low reactivity as a result of the need for a thermally stable pitch during the spinning operation. For these reasons, it is desirable to have a fiber with a high T_g (glass transition temperature) in order to allow higher stabilization temperatures, higher rates of oxygen diffusion, and thus lower reaction times. The purpose of oxidation is to prevent the fiber from melting during the subsequent carbonization process, thus to "lock in" the structure developed during the extrusion process. The stabilization is accomplished by exposing the fibers to flowing air at a temperature of approximately 300°C for several hours. During this process, oxygen tends to react first with aliphatic side groups, cross-linking and adding weight to the fiber. If insufficient time is allowed for stabilization, there is a gradient of oxygen across the filament radius, and a skin core texture may be resulted. Fibers thinner than 10μm do not exhibit a skin-core texture because of rapid oxygen diffusion, unless the oxygen content of the stabilizing atmosphere is reduced [16].

Carbonization or high temperature heat treatment of the stabilized fiber may consist of two separate steps: first to around 1000°C in order to reduce the rate of gas evolution and then to temperatures between 1200 to 3000°C, depending upon the increases with heat treatment temperature in contrast to PAN-based fiber. The high temperature MP fibers have, the higher modulus and usually lower tensile strength compared to PAN-based fibers it has at the same temperature [16].

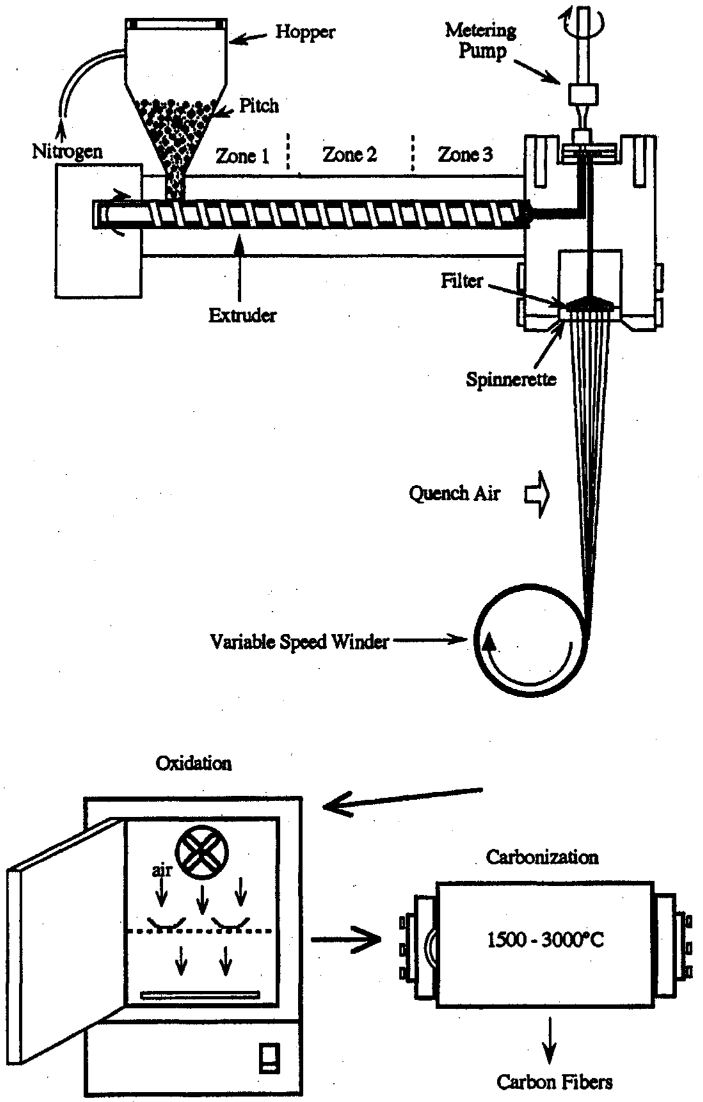

Figure 1.9: processing sequence of mesophase carbon fibers, showing continuous conventional melt spinning of mesophase pitch, and subsequent batch processes: oxidization stabilization. Adapted from [1].

1.5 Morphology of Mesophase Pitch-based Carbon Fibers

As we mentioned before, the carbon fibers melt-spun from mesophase pitch exhibit a variety of transverse textures [16,20]. Table 1.1 shows the influence of the mesophase fiber texture to the properties of the end product. The microstructure is defined by the spatial arrangement of the flat disc-like molecules in the fibers. The commonly observed transverse textures are random, radial, polar, onion-like, and oriented core or a mixture of these textures across a fiber radius. In the radial texture, the discotic molecules oriented with their unit normal describing a circles concentric with the fiber axis, while in the planar polar texture the dicotic molecules alignment perfectly in the center region of the fiber with two disorder region on the edge of the fiber collinear with the fiber center. The morphology or cross section texture of mesophase pitch-based carbon fibers is controlled by the pretreatment of the mesophase pitches, the constitution and spinnability of pitches, the spinning conditions, the fiber diameter, the spinning tension, the temperature, etc. figure 1.10 shows SEM and optical micrographs for two of these textures.

Bright and Singer compared the electrical resistivities of mesophase pitch-based carbon fibers with those of radial and random textures [21]. They found that, fibers with radial textures developed lower resistivities than those with random textures. Since electrical resistivity and thermal conductivity are inversely related, one would expect fibers with radial textures to be good candidates for thermal management applications.

Unfortunately, circular fibers with a radial texture tend to crack and split during high temperature treatment. One possible solution for developing high thermal conductivities while avoiding fiber cracking is changing the shape of fiber from circle to ribbon [22,23,24]. Figure 1.11 shows the scanning electron micrographs of the ribbon shaped carbon fiber.

In this thesis, the experimentally observed textural features will be elucidated by doing thorough investigation of the parametric and geometrical effects (i.e. circular and non-circular fiber cross-sections) or orientation patterns.

Code	Texture	Dim^1 (μm)	Δl^2 (%)	$D_0{}^3$ (%)	Lc(002) (nm)	δt^4 (GP)	Et^5 (GP)	δC^6 (GP)
1-A	Radial with open wedge	11.0	0.30	95.4	22	2.8	740	--
1-B	Skin radial-core random	8.1	0.42	94.2	21	3.4	800	0.4
1-C	Random	9.2	0.45	94.2	20	3.6	780	0.7
1-D	Quasi-onion	10.4	0.32	95.0	21	2.6	720	--

Table 1.1: The influence of fiber textures to the properties of end product. (1) Diameter of fiber. (2) Strain to break. (3) Degree of preferred orientation. (4) Tensile strength. (5) Young's modulus (6) Compression strength (Vf 60 vol%). Adapted from [20].

(a) (b)

Figure 1.10: SEM images of cylindrical mesophase pitch-based cabon fibers with (a) radial texture, (b) planar polar texture. Adapted from [16].

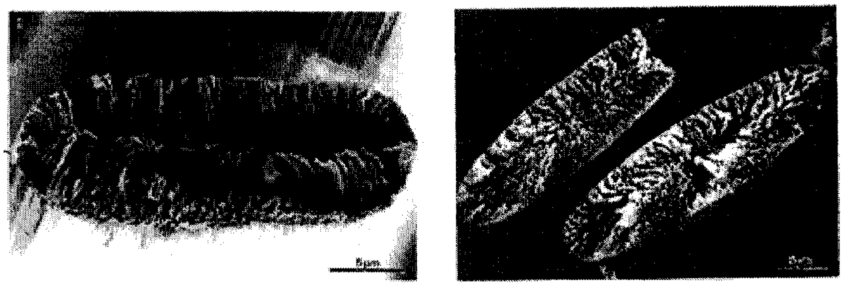

(a) (b)

Figure 1.11: SEM images of ribbon shape mesophase pitch-based carbon fibers with (a) Line texture in center. (b) Radial-like texture. Adapted from [23,24].

1.6 Objectives

The specific objectives of this thesis are:

(1) To formulate, solve, and validate a model of transient texture formation for mesophase carbon fibers;

(2) To simulate the transient formation process of planar radial and planar polar textures (Figs. 1.10) observed in carbon fibers of circular cross-section using large scale computer simulations based on well-established theories about discotic nematic liquid crystals;

(3) To simulate the transient formation process of line and radial-like textures (Figs. 1.11) observed in ribbon-shaped carbon fibers using large scale computer simulations based on well-established theories about discotic nematic liquid crystals;

(4) To identify the fundamental principles which govern the pattern selection process of mesophase carbon fiber texture.

(5) To discover processing pathways for targeted carbon fiber texture production.

1.7 Thesis organization

This Masters Thesis is organized as follows:

Chapter 1 presents the necessary background concepts on masophase carbon fiber. including the motivation of this thesis, and an introduction to mesophase carbon fibers.

Chapter 2 presents the theory used to model and simulate the disk like nematic liquid crystalline behavior in mesophase carbon fiber, including the Frank elasticity theory, the Landau-de Gennes theory, and the concepts of defects in liquid crystalline materials.

Chapter 3 presents the modeling and simulation of the transient planar radial and planar polar texture formation process using the Landau-de Gennes mesoscopic theory for discotic liquid crystals. The computed planar polar and planar radial textures phase diagram, given in terms of temperature and fiber radius, is presented to establish the processing conditions and geometric factors that lead to the selection of these textures. The influence of elastic anisotropy to the textures' formation and structure is thoroughly characterized.

Chapter 4 presents the theory and simulations of defect phenomena during the formation process of the planar polar texture in elastic isotropy, including defect nucleation, defect migration, and overall texture geometry.

Chapter 5 presents the application of the Landau-de Gennes mesoscopic theory to model the texture formation of ribbon shape mesophase carbon fiber. The mechanism of texture selection in terms of fiber cross-section shape is discussed.

Chapter 6 presents the conclusions of this thesis.

Bibliography

[1] McHugh J. J., 1994, *PHD Thesis*, Clemson University

[2] Kowalsky I. M., 1987, *Advanced Materials Technology'87*, Volume 32 of the International SAMPE Symposium, Editors: R. Calrson et al., Anaheim, 953.

[3] Bacon R., Nelson L. C., Singer L. S., Schulz D. A., Wagoner G., Lewis I. C., Lewis R. T., Strong S. L., Rosen B. W. and Sullivan B. J., 1989, *Naval Surface Warfare Center Transcript 89-169*, Silver Spring, MD.

[4] Priestley E. B., Wojtowicz P. J. and Sheng P., 1975, *Introduction to Liquid Crystals*, Plenum Press, New York.

[5] Chandrasekhar S., 1992, *Liquid Crystals*, 2nd edition, Cambridge University Presss, Cambridge.

[6] De Gennes P. G. and Prost J., 1993, *The Physics of Liquid Crystal* 2nd edn (Oxford: Clarendon).

[7] Singh A. P., 2000, *Ph.D Thesis,* Mcgill University.

[8] Hurt R. H. and Chen Z. Y., 2000, *Physics Today,* **March,** 39.

[9] Singer L. S., 1977, *U.S. patent 4,005,183.*

[10] Zimmer J. E. and White J. L., 1982, *Advances in Liquid Crystals*, **5**, 157, Editor: Brown H. G., Academic Press, New York.

[11] Brooks J. D. and Taylor G. H., 1965, *Carbon*, **3**(2), 185; 1965, *Nature*, **206**, 697.

[12] Fitzer E., Kompalik D. and Mayer B., 1986, *Carbon'86: Proceedings of International Carbon Conference*, Baden-Baden, Germany, 842.

[13] Otani S. and Oya A., 1986, *ACS Symp. Ser.*, **303**(22), 323.

[14] Huchenson K. W., Roebers J. R. and Thies M. C., 1991, *Carbon*, **29**(2), 215.

[15] Korai Y., Nakamura M. and Mochida I., 1991, *Carbon*, **29**(5), 561.

[16] Peebles L. H. Jr., 1995, *Carbon Fibers-Formation, Structure, and Properties* (Boca Raton, FL: CRC)

[17] Edie D. D. and Dunham M. G., 1986, *Carbon*, **24**(4), 477.

[18] Edie D. D., Fox N. K., Barnett B. C. and Fain C. C., 1986, *Carbon*, **24**, 477.

[19] Edie D. D. and Stoner E. G., 1993, *Carbon-carbon Materials and Composites*, 41, Editor: Buckley J. D. and Edie D. D., Noyes, Park Ridge, NJ.

[20] Mochida I., Yoon S.-H., Takano N., Fortin F., Korai Y. and Yokogawa K., 1996, *Carbon*, **34**, 941.

[21] Bright A. A. and Singer L. S., 1979, *Carbon*, **17**, 59.

[22] Edie D. D., Robinson K. E., Fleurot O., Jones S. P. and Fain C. C., 1994, *Carbon*, **32**(6), 1045.

[23] Robinson K. E. and Edie D. D., 1996, *Carbon*, **34**(1), 13.

[24] Edie D. D., Fain C. C., Robinson K. E., Harper A. M. and Rogers D. K., 1993, *Carbon*, **31**(6), 941.

Chapter 2

Continuum Theory of Liquid Crystals

2.1 Continuum Theory of Liquid Crystals

The melt spinning of carbonaceous mesophases is a complex process involving viscous, elastic, and thermal processes. This thesis is mainly concerned with the characterizing the role elasticity in the texture formation processes during the melt spinning of carbonaceous mesophases using the continuum theory for liquid crystal properly adapted to discotic nematic mesophases. This chapter presents the theoretical framework as well as a full derivation model used to simulate transient mesophase texture formation under anisotropic elastic deformations. Simulation results are shown in the following chapters.

2.1.1 Frank Orientation Distortion Elasticity

The simplest nematic state is that of a uniform orientation domain, known as monodomain. This uniform orientation state is easily perturbed under the influence of bounding surface conditions, defects, and external fields such as shear, electric and magnetic fields. For example, the textures shown in Fig1.10-1.11 clearly show the presence of orientational distortions due to boundary conditions in a circular domain, as well as defects. The distorted orientation state is described by minimizing the orientation distortion energy, also known as Frank elastic energy or long range energy.

Frank identified three possible independent distortion modes according to which the director **n** can vary in the neighborhood of the origin, as shown in the fig. 2.1 [1,2,3]. In the first one, the "splay" mode, the curvature is represented by the components $\partial n_x/\partial x$ and $\partial n_y/\partial y$, in the second, the "twist" mode, the curvature is represented by $-\partial n_y/\partial x$ and $\partial n_x/\partial y$, and in the third, the "bend" mode by $\partial n_x/\partial z$ and $\partial n_y/\partial z$. Based on this physical picture, and using material symmetry (i.e., corresponding to the absence of polarity and enantiomorphy) and material objectivity (i.e., corresponding to invariance with respect to rotation around the z-axis), Frank showed that, within the quadratic limit, the curvature or distorted orientation elasticity in terms of **n** could be represented for nematic liquid crystals in coordinate free notation as [1,2,3]:

$$\begin{aligned} f_n &= \frac{1}{2}K_{11}(\nabla \bullet \mathbf{n})^2 + \frac{1}{2}K_{22}(\mathbf{n} \bullet \nabla \times \mathbf{n})^2 + \frac{1}{3}K_{33}\left|(\mathbf{n} \bullet \nabla)\mathbf{n}\right|^2 \\ &- \frac{1}{2}(K_{22} + K_{24})\left[(\nabla \bullet \mathbf{n})^2 + \left|\nabla \times \mathbf{n}\right|^2 - \nabla\mathbf{n} : \nabla\mathbf{n}\right] \end{aligned} \tag{1}$$

where K_{11} (splay mode) , K_{22} (twist mode) K_{33} (bend mode) and K_{24} (saddle-splay mode) are four, in general non-vanishing, elastic moduli, f_n is the change of Helmholtz free energy density between the LC with perfect alignment and with distortions. The elastic moduli are subject to the inequalities [3]:

$$K_{11} \geq 0,\ K_{22} \geq \left|K_{24}\right|,\ K_{33} \geq 0,\ 2\,K_{11} \geq K_{22} + K_{24} \tag{2}$$

so that the homogeneous state corresponds to a minimum of the free energy. As the last term in eqn. (1) represents a total differential, it can be accounted for by a surface integral. Therefore, when ignoring the surface energy contribution, eqn. (1) can be reduced to [1,2,3]:

$$f_n = \frac{1}{2}K_{11}(\nabla \bullet \mathbf{n})^2 + \frac{1}{2}K_{22}(\mathbf{n} \bullet \nabla \times \mathbf{n})^2 + \frac{1}{3}K_{33}\left|(\mathbf{n} \bullet \nabla)\mathbf{n}\right|^2 \tag{3}$$

thus in the description of the bulk phenomena, eqn.(3) is applied as the definition of the free energy density of nematic liquid crystals. According to the thermodynamic stability, the following restriction should be obeyed [3]:

$$K_{11} \geq 0,\ K_{22} \geq 0,\ K_{33} \geq 0 \tag{4}$$

which is corresponding to the three distortion modes mentioned before: splay, twist and bend. For disk like nematic liquid crystal [4,5]:

$$K_{22}>K_{11}>K_{33} \tag{5}$$

2.1.2 Disclinations

The name " nematic " means thread in the Greek language, and is used due to the thin black brushes that can be seen within the fluid under a microscope. The threads originate from points corresponding to the 'line singularities' perpendicular to the nematic layer [6] being observed under the optical microscope. Similar to dislocations in crystals, Frank proposed the term 'disinclinations', which has been modified to disclinations in current usage.

The strength of a disclination is defined as $s=\frac{1}{4}$(number of brushes), which indicates the amount of orientation distortion, and the sign (+/-) corresponds to the sense of orientation rotation while circling the defects. Only disclinations of strengths +1/2, -1/2, +1, -1 are generally observed.

Consider the planar structure in which the director is confined to the xy plane (the z axis being normal to the film). Taking the components of the director to be $n_x = \cos\phi$, $n_y = \sin\phi$, $n_z=0$ (ϕ is the orientation angle with respect to x direction), and making the simplifying assumption that the medium is elastically isotropic, i.e. $K_{11}=K_{22}=K_{33}=k$, equation (3) reduces to:

$$f_n = \frac{1}{2}k(\nabla\phi)^2 \tag{6}$$

And the system tend to minimize the free energy f_n when the director angle obeys Laplaces' equation:

$$\nabla^2\phi = 0 \tag{7}$$

Seeking a simple solution independent of $r = (x^2 + y^2)^{\frac{1}{2}}$, the solutions of eqn (7) are:

$$\phi = s\alpha + c \ \left(s = \pm\frac{1}{2}, \pm 1, \ldots\ldots..\right) \tag{8}$$

where α is the position angle with respect to the x axis and c is a constant. The solutions' plots of eqn (8) are shown in fig. 2.2.

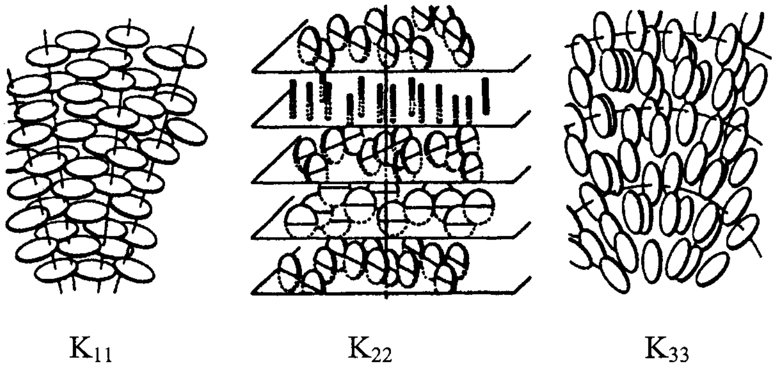

Figure 2.1: Schematics of the elastic splay (left), twist (centre), and bend (right) deformation for uniaxial discotic nematics. Note that the splay (bend) mode involves bending (splaying) of the disk's trajectories, in contrast to the case of uniaxial rod-like nematics. A disk trajectory is a curve locally orthogonal to the director. Adapted from [4].

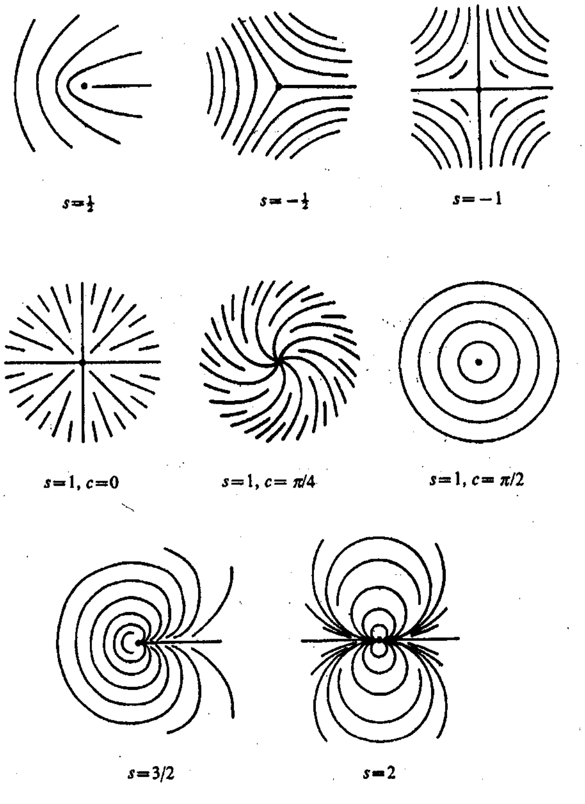

Figure 2.2: molecular orientation in the neighborhood of a disclination. Adapted from [6].

The energy of deformation of an isolated disclination in a circular layer of radius R and of unit thickness is:

$$W = W_c + \pi k s^2 \ln(R/r_c) \tag{9}$$

where r_c is the radius of disclination core, and W_c is the energy of the central defect region. Eqn. (9) shows that the energy of a single defect is proportional to s^2 according to the planar model, so that usually the defects of strength $|s| > \frac{1}{2}$ should be unstable and dissociate into $|s| = \frac{1}{2}$ defects.

Due to the long range elastic distortions, defects interact with each other as charged particles do. The interaction between two disclinations of strength s_1 and s_2 is:

$$W = \pi k(s_1 + s_2)^2 \ln(R/r_c) - 2\pi k s_1 s_2 \ln(r_{12}/2r_c) \tag{10}$$

where r_{12} is the distance between the two defects, and $r_c << r_{12} << R$. Accordingly, the force between two defects is:

$$F = 2\pi k s_1 s_2 / r_{12} \tag{11}$$

Disclinations of same sign repel and those of opposite signs attract, the force being inversely proportional to the distance [6]. Note that all the derivations above are based on the elastic isotropic case. When considering the elastic anisotropic case ($K_{11} \neq K_{22} \neq K_{33}$), the equation for the defect interaction force becomes much more complicated.

2.1.3 Orientational Ordering

To fully capture nematic ordering both the amount of molecular ordering along the preferred orientation (i.e., the director **n**) and the prefered orientation must be specified. Thus, in general the vector **n** is insufficient and a second order tensor **Q** has to be used to fully describe nematic ordering. The nematic phase has a lower symmetry than the high-temperature isotropic liquid. In order to experss this in a quantitative way we introduce a tensor order parameter **Q** [7,8], such that:

(1) **Q**=0 in the isotropic phase;

(2) **Q**≠0 in the nematic phase;

All macroscopic response functions of the bulk material, such as the dielectric permittivity or the diamagnetic susceptibility, are anisotropic and can be applied as the order parameter. In order to include all the information of order and orientation into **Q**, the most general form of **Q** is a second order, traceless, symmetric tensor given as:

$$\mathbf{Q}=S\,(\mathbf{nn}-\frac{1}{3}\mathbf{I})+\frac{1}{3}P\,(\mathbf{mm}-\mathbf{ll}) \tag{12}$$

where the following restrictions apply:

$$\mathbf{Q}=\mathbf{Q}^{T};\ \mathrm{Tr}(\mathbf{Q})=0;\ -\frac{1}{2}\leq S\leq 1; -\frac{3}{2}\geq P\geq\frac{3}{2} \tag{13}$$

$$\mathbf{n}\cdot\mathbf{n}=\mathbf{m}\cdot\mathbf{m}=\mathbf{l}\cdot\mathbf{l}=1;\ \mathbf{nn}+\mathbf{mm}+\mathbf{ll}=\mathbf{I};$$

where **n**, **m**, **l**(=**n**×**m**) are unit orientation vectors which form orthogonal director triad ; **n** is known as the (unaxial) director and **m**, **l** are termed as the biaxial directors, S is the uniaxial scalar order parameter and P is the biaxial scalar order parameter. On the principal axes, the tensor order parameter is written as:

$$\mathbf{Q}=\begin{bmatrix} -\frac{1}{3}(S-P) & 0 & 0 \\ 0 & -\frac{1}{3}(S+P) & 0 \\ 0 & 0 & \frac{2}{3}S \end{bmatrix} \tag{14}$$

where $\frac{2}{3}S$, $-\frac{1}{3}(S-P)$, and $-\frac{1}{3}(S+P)$ are the eigenvalues corresponding the eigenvectors **n**, **m**, and **l** respectively. If all the eigenvalues of the tensor order parameter **Q** are zero (i.e. S=0,P=0) then the phase is defined as isotropic. If two eigenvalues are equal (i.e. S≠0, P=0) then the phase is termed as uniaxial nematic, and the uniaxial scalar order parameter S is sufficient to define the order of alignment of the molecules in the phase. If all the eigenvalues are different (i.e. S≠0, P≠0), the phase is called biaxial nematic [16,27].

In the case of perfect axially symmetric molecules (for example rigid rods or rigid circular disks), no molecular interactions can result in a macroscopic ordering that is less symmetric than the molecules themselves. Thus an external cause, such as an external field perpendicular to **m**, is necessary to produce ordering in a plane normal to **n**. The presence of an external field is referred to as field-induced biaxility. In the absence of an external field, the biaxial nematic phase is expected only for molecules that are geometrically biaxial or do not possess axial symmetry [7,8]. On the other hand, the cores of the defects shown in fig. 2.2 are known to be biaxial.

As mentioned in chapter one, S is known as the uniaxial scalar order parameter or uniaxial alignment, and is a measure of degree of alignment of the unit normals to the disc like molecules in the direction of director **n**. Similar to S, the biaxial scalar order parameter P is a measurement of the degree of alignment of the preference of the molecular normal along the biaxial director **m**, which is in the plane orthogonal to the uniaxial director **n**. In other words, the biaxial scalar order specifies the amount of transverse ordering.

Since the complete description of nematic ordering requires the specification of **Q**, the Frank elastic energy is inadequate when changes in the order parameters, biaxiality and/or defects are present. Since all these three phenomena occur during texture formation, a theory based on the tensor order parameter must be specified. The Landau-de Gennes tensor order parameter theory is such a theory and is described in the next section.

2.1.4 Landau-de Gennes Tensor Order Parameter Theory

Ignoring the surface energy and the influence of external fields, the Landau-de Gennes total energy density is expressed as [1]:

$$f_b = f_0 + f_s + f_\ell \tag{15}$$

where f_0 is the free energy density of the isotropic state, f_s is the short-range energy density, which is responsible for the nematic-isotropic phase transition, and f_ℓ is the long-range energy. The short-range free energy density $f_s(\mathbf{Q})$ can be expressed as [1,2,3,7]:

$$f_s = f_0 + \frac{1}{2}A(\mathbf{Q}:\mathbf{Q}) + \frac{1}{3}B(\mathbf{Q}:(\mathbf{Q}\cdot\mathbf{Q})) + \frac{1}{4}C(\mathbf{Q}:\mathbf{Q})^2 + \ldots\ldots \tag{16}$$

where the A, B, C are phenomenological coefficients, and f_0 is the free energy density for a given temperature and pressure of the state with **Q**=0. To have a minimum in the short range free energy, C must be positive. Under uniaxial ordering (P=0), f_s is only a function of S. Fig. 2.3 shows the short range energy f_s as a function of the scalar order parameter S for B<0, for different temperatures. Four temperature regions can be distinguished [7]:

(1) $T > T^+$: the minimum corresponds to an isotropic phase (S=0);

(2) $T_{NI} < T < T^+$: the minimum corresponds to an isotropic phase. In addition, there is a local minimum corresponding to a possible superheated nematic state;

(3) $T^* < T < T_{NI}$: the minimum corresponds to a nematic phase. There is a local minimum corresponding to a possible supercooled isotropic state.

(4) $T < T^*$: the minimum corresponds to a nematic phase.

Below T^* the isotropic phase is completely unstable with respect to the nematic state; the local minimum at S=0 does not exist anymore. Above T^+ the nematic phase is completely unstable with respect to the isotropic phase; the local minimum at $S \neq 0$ does not exit anymore.

In order to generalize the Frank distortion elasticity description close to the clearing point, de Gennes proposed a Landau-Ginzburg type of expansion for long-range energy density f_ℓ in terms of the derivatives of the tensor order parameter $\nabla\mathbf{Q}$. In absence of electric and magnetic fields, the expression of f_ℓ becomes [3,9,10]:

$$f_\ell = \frac{1}{2}L_1(\nabla\mathbf{Q} \vdots \nabla\mathbf{Q}) + \frac{1}{2}L_2(\nabla\cdot\mathbf{Q})\cdot(\nabla\cdot\mathbf{Q}) + \frac{1}{2}L_3\mathbf{Q}:(\nabla\mathbf{Q}:\nabla\mathbf{Q}) + \ldots \tag{17}$$

where L_1, L_2 and L_3 are elastic moduli. Up to second order terms in **Q**, only L_1 and L_2 appear in the expression of f_ℓ. In the uniaxial case (P=0) L_1 and L_2 can be correlated to the Frank elastic moduli K_{11}, K_{22}, and K_{33} as follows [3]:

$$L_1 = \frac{K_{22}}{2S^2}\ ,\ L_2 = \frac{K_{11} - K_{22}}{S^2} \tag{18a,b}$$

Thermodynamic stability restrictions impose the following inequality [10]:

$$L_1 > 0,\ 3L_1 + 5L_2 > 0 \tag{19}$$

In addition, the molecular geometry involved in the discotic nematic phase requires that [5,8]:

$$L_2 < 0 \tag{20}$$

In this case, de Gennes's theory, as expressed by eqn. (17), gives very simple expressions for the Frank elasticity constants. The expansion (17) implies that $K_{11}=K_{33}$, in clear contradiction to experiments. The $K_{11}=K_{33}$ relation arises because only second order **Q** terms were retained in the free energy. To remove this restriction from the tensor theory, it suffices to include higher order terms in **Q.** However, the final expression is no longer unique. One of the simplest extensions involves inclusion of the L_3 term in the free energy. In actuality there are six independent L_3 terms. One of this six terms is: $Q_{\alpha\beta}Q_{\gamma\delta,\alpha}Q_{\gamma\delta,\beta}$ (shown in eqn.17) which is able to reproduce experimental data. In this research [11], only this term is added in our model. So the relation between the Landau-de Gennes elastic constants L_1, L_2 and L_3 and the Frank elastic constants K_{11}, K_{22}, and K_{33}, under uniaxial ordering (P=0) are:

$$L_1 = \frac{3K_{22} - K_{11} + K_{33}}{6S^2}, \; L_2 = \frac{K_{11} - K_{22}}{S^2}, L_3 = \frac{K_{33} - K_{11}}{2S^3} \qquad (21a, b, c)$$

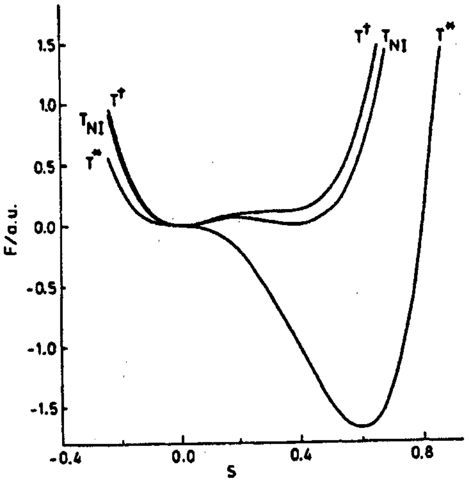

Figure 2.3: the free energy F as a function of the scale order parameter S, for the special temperatures T^*, T_{NI}, T^+, for S_{NI}=0.4.

De Gennes shows that the dynamics of nematics is essentially described by the Landau theory of phase transitions, as we show in the previous section and proposed a phenomenological nonlinear equation for the kinetics of order parameter tensor **Q** [12]:

$$-\gamma(\mathbf{Q})\frac{d\mathbf{Q}}{dt} = \frac{\delta F}{\delta \mathbf{Q}} = \left(\frac{\partial f_b}{\partial \mathbf{Q}} - \nabla \cdot \frac{\partial f_b}{\partial \nabla \mathbf{Q}}\right)^{[s]} \qquad (22)$$

where [s] indicates the symmetric and traceless, $\gamma(\mathbf{Q})$ is the rotational viscosity coefficient, and $\frac{\delta F}{\delta \mathbf{Q}}$ is the functional derivative of the total energy F. Equation (22) is a gradient system, where evolution is dictated by energy minimization. On the other hand, Doi proposed the following expression for coefficients A, B, C that appear in the short range energy, given in equation [12]:

$$A = ckT\frac{1}{2}\left(1 - \frac{U}{3}\right), B = -ckT\frac{U}{3}, C = ckT\frac{U}{4} \tag{23}$$

where c is the number density of the discs, k is the Boltzmann's constant, and $U = \frac{3T^*}{T}$ is the nematic potential or dimensionless temperature. Note that as U increases, the temperature T decreases. T* is a reference temperature just below the isotropic-nematic phase transition temperature introduced in the previous section.

Specific models based on this theory will be formulated, solved, and validated in chapter 3, 4, and 5. In chapter 3, we explain the effect of L_2 and L_3 anisotropy to the fiber texture. In chapter 4, the model shows the transient process of fiber formation in which $L_3=0$. In chapter 5, we explain the application of the model with different initial conditions to the non-circular fiber geometry.

2.2 Computational Method

2.2.1 Finite Element Method

Virtually every phenomenon in nature, whether biological, geological, or mechanical, can be described with the aid of the laws of physics, in terms of algebraic, differential, or integral equations relating various quantities of interest. While the derivation of the governing equations for these problems is not difficult, their solution by exact methods of analysis is a formidable task. In such cases approximate methods of analysis provide alternative means of finding solutions. The methods of weighted residual such as the the Galerkin finite element method is frequently used in the literature.

The finite element method provides a systematic procedure for the derivation of the approximation functions. The method is endowed with two basic features, which account for its superiority over other competing methods. First, a geometrically complex domain of the problem is represented as a collection of geometrically simple subdomains, called finite elements. Second, over each finite element the approximation functions are derived using the basic idea that any continuous function can be represented by a linear combination of algebraic polynomials. The approximation functions are derived using concepts from interpolation theory, and are therefore called interpolation functions. Thus, the finite-element method can be interpreted as a piecewise application of the variational methods (eg., weighted residual methods), in which the approximation functions are algebraic polynomials and the undetermined parameters represent the values of the solution at a finite number of preselected points, called nodes, on the boundary and in the interior of the element. From interpolation theory the order of the interpolation function depends on the number of the nodes in the element [15].

There are certain steps to solve the partial differential equations using Garlerkin finite element methods:

- Finite-element discretization (mesh)

First, the continuous region (i.e. circle) needs to be represented as a collection of a finite number n of subregions, for example rectangular. Each subregion is called an element. There are lots of different mesh generation methods, like the tree structure method. A typical mesh generation program locates and numbers the nodal points, numbers the elements, and determines the element incidences. The number of elements used in a problem depends mainly on the element type and accuracy desired.

- Derivation of element equations

To apply the finite element method, the variational form of the original model (eqn. (22)) over a typical element needs to be derived. For example, the equation of $\frac{dQ_{11}}{dt}$ in eqn. (22) can be written as:

$$\int_e \left(\gamma(\mathbf{Q}) \frac{dQ_{11}}{dt} + \left(\frac{\partial f_b}{\partial \mathbf{Q}} - \nabla \cdot \frac{\partial f_b}{\partial \nabla \mathbf{Q}} \right)_{11}^{[s]} \right) \varphi_i dxdy = 0 \tag{24}$$

where φ_i (i=1,2,…,N) is the known basis function. Expand the approximate solution in terms of unknown coefficients and known basis functions:

$$Q_{11} = \sum_1^N Q_{11j}(t)\varphi_j(x,y,z) \tag{25}$$

where φ_j (j=1,2,3,4) are the known basis function (the same as which is in eqn (24)), N is the number of nodes in the finite element mesh, and Q_{11j} is the solution vector. Replacing eqn (25) into eqn (24) gives:

$$\gamma(\mathbf{Q}) \frac{dQ_{11j}}{dt} \int_e \varphi_i \varphi_j dxdy = -\int_e \left(\left(\frac{\partial f_b}{\partial \mathbf{Q}} - \nabla \cdot \frac{\partial f_b}{\partial \nabla \mathbf{Q}} \right)_{11}^{[s]} \right) \varphi_i dxdy \equiv \underline{B} \tag{26}$$

Defining the mass matrix M_{ij} as:

$$M_{ij} \equiv \int_{e} \varphi_i \varphi_j dxdy \tag{27}$$

the equation can be written finally as:

$$\underline{Q_{11}}(t_{n+1}) = \frac{\Delta t_{n+1}}{\gamma} \underline{B} \cdot \underline{\underline{M}}^{-1} + \underline{Q_{11}}(t_n) \tag{28}$$

where t_n is the time of n iteration, Δt_{n+1} is the time step adopted in n+1 time step. All the terms in the right hand of eqn (2.28) are evaluated at the time level t_n and are known functions of the boundary conditions and initial conditions. The unknown on the left hand side of eqn.(28) can be easily evaluated by performing the matrix-vector multiplication. The equations for the other components Q_{11j}; j=2,3,...,N, of the solution vector are computed in a similar fashion.

- Convergence and error

For an unknown exact solution, it's better to do the computation using different mesh densities (mesh refinement) and compare the solutions on the same nodes' location in order to get a mesh independent solution.

2.2.2 Runge-Kutta Time Adaptive Method

Real world engineering processes are characterized by several disparate time constants, with the result that the models that describe these processes give rise to stiff equations. (For example the model of a convection-reaction process with fast flow and slow reaction leads to a stiff equation). Stiff problems are not suitable to solve using constant time step integration methods, but are effectively solved using adaptive methods. The purpose of the adaptive time step-size control is to achieve some predetermined accuracy in the solution with minimum computational effort. Many small steps should tiptoe through treacherous terrain, while a few great strides should speed through smooth uninteresting countryside.

A stepsize adjustment algorithm used in this thesis is based on the embedded Runge-Kutta formulas. The general forma of a fifth-order Runge-Kutta formula is [16]:

$$
\begin{aligned}
&k_1 = hf(x_n, y_n)\\
&k_2 = hf(x_n + a_2h, y_n + b_{21}k_1)\\
&\cdots\cdots\\
&k_6 = hf(x_n + a_6h, y_n + b_{61}k_1 + \cdots + b_{65}k_5)\\
&y_{n+1} = y_n + c_1k_1 + c_2k_2 + c_3k_3 + c_4k_4 + c_5k_5 + c_6k_6 + O(h^6)
\end{aligned}
\tag{29}
$$

the embedded fourth-order formula is:

$$y^*_{n+1} = y_n + c^*_1k_1 + c^*_2k_2 + c^*_3k_3 + c^*_4k_4 + c^*_5k_5 + c^*_6k_6 + O(h^6) \tag{30}$$

and so the error estimate is:

$$\Delta \equiv y_{n+1} - y^*_{n+1} = \sum_{i=1}^{6}(c_i - c^*_i)k_i \tag{31}$$

where h is the time step. a_i and b_{ij} are known coefficients.

At this stage we know, at least approximately, what our error is. To find the relation between Δ and h, according to eqn (29) and eqn (30), Δ scales as h^5. If a step h_1 produces an error Δ_1, the step h_0 that would have given some other value Δ_0 is readily estimated as:

$$h_0 = h_1\left|\frac{\Delta_0}{\Delta_1}\right|^{0.2} \tag{32}$$

Henceforth we will let Δ_0 denote the desired accuracy. Then equation (32) is used in two ways: if Δ_1 is larger than Δ_0 in magnitude, the equation tells how much to decrease the step size when we retry the present (failed) step. If Δ_1 is smaller than Δ_0, on the other hand, the equation tells how much we can safely increase the step size for the next step, so that the time step is fully controlled during the time integration.

Bibliography

[1] De Gennes, P. G. and Prost, J., 1993, *The Physics of Liquid Crystal* 2^{nd} edn (Oxford: Clarendon).

[2] Priestley E. B., Wojtowicz P. J. and Sheng P., 1975, *Introduction to Liquid Crystals*, Plenum Press, New York.

[3] Beris A. N. and Edwards B. J., 1994, *Thermodynamics of flowing systems* (Oxford: Claredon).

[4] Sokalski K. and Ruijgrok T. W., 1982, *Physica,* **113A**, 126.

[5] Osipov M. A. and Hess S., 1993, *Molecular Physics*, **78**, No. 5, 1991

[6] Chandrasekhar S., 1992, *Liquid Crystals* 2^{nd} *edn* (Cambridge University Press).

[7] Gramsbergen E. F., Longa L. and de Jue W. H., 1986, *Physics Reports (Review Section of Physics Letters)*, 135(4), 195.

[8] Singh A. P., 2000, *Ph.D Thesis,* Mcgill University.

[9] Berreman D. W. and Meiboom S., 1984, *Physical Review A*, vol. **30**, no. 6, 1955

[10] Longa L., Monselesan D. and Trebin H. R., 1987, *Liquid Crystals,* vol. **2,** no. 6, 769.

[11] Schiele K. and Trimper S., 1983, *Phys. Stat. Sol. (b),* **118**, 267

[12] Doi M. and Edwards B. J., 1986, *The Theory of Polymer Dynamics* (Oxford: Clarendon).

[13] Tsuji T. and Rey A. D., 1997, *J. Non-Newtonian Fluid Mech.*, **73,** 127.

[14] Sonnet A., Kilian A. and Hess S., 1995, *Physical Review E,* **52,** 52.

[15] Reddy J. N., 1984, *An Introduction to the Finite Element Method*, McGraw-Hill Inc.

[16] Press W. H., Teukolsky S. A., Vetterling W. T., and Flannery B. P., 1992, Numerical Recipes in Fortran 77, The Art of Scientific Computing, 2nd edition, Cambridge University Press.

Chapter 3

Texture Formation in Carbonaceous Mesophase Fibers

3.1 Abstract

Carbonaceous mesophases are discotic nematic liquid crystals that are spun into high performance carbon fibers using the melt spinning process. The spinning process produces a wide range of different fiber textures. Planar polar (PP) and planar radial (PR) textures are two ubiquitous ones. This paper presents theory and simulation of the texture formation process using the Landau-de Gennes mesoscopic theory for discotic liquid crystals. The computed PP and PR textures phase diagram, given in terms of temperature and fiber radius, is presented to establish the processing conditions and geometric factors that lead to the selection of these textures. Thin fibers adopt the PR texture, while thicker fibers and lower temperatures adopt the PP texture. The influence of elastic anisotropy to the textures' formation and structure is thoroughly characterized.

3.2 Introduction

Carbonaceous mesophases, such as coal tar and petroleum pitches, are used in the industrial manufacturing of high performance carbon fibers. This relatively new carbon fiber is more competitive than the conventional one made from the acrylic precursors in several application areas [1]. The thermodynamic phase that describes carbonaceous mesophases is the discotic nematic liquid crystal (DNLC) state [2]. Liquid crystals are intermediate (i.e. mesophase) phases, typically found for anisodiametric organic molecules, which exist between the higher temperature isotropic liquid state and the lower temperature crystalline state. Carbonaceous mesophases are composed of disk-like molecules. Figure 3.1 shows the molecular geometry, positional disorder, and uniaxial orientational order of discotic nematic liquid crystals. The partial orientational order of the molecular unit normal **u** is along the average orientation or director **n** (**n**·**n**=1). The name discotic distinguishes the molecular geometry and the name nematic identifies the type of liquid crystalline orientational order.

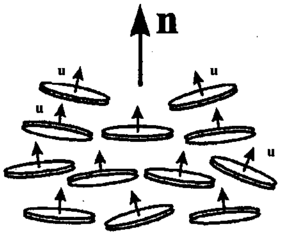

Figure 3. 1: Definition of director orientation of a uniaxial discotic nematic liquid crystalline material. The director n is the average orientation of the unit normals to the disk-like molecules in a discotic nematic phase.

The industrial fabrication of mesophase carbon fiber using the conventional melt spinning process typically produces micrometer-sized cylindrical filaments whose cross sectional area displays a variety of transverse textures [3], that is, different spatial arrangements of the average orientation **n** on the plane perpendicular to the fiber axis. The selection mechanisms that drive the texture formation pattern are at present not well understood, but due to the strong structure-properties correlations, they are essential for product optimization [1,3].

A question of fundamental importance to the melt spinning of carbonaceous mesophases is to determine how elastic and viscous mechanisms affect the fiber process-induced structuring and cross-sectional fiber textures' selection. When considering elastic mechanisms, it is necessary to identify the three fundamental elastic modes of these materials. Figure 3.2 shows the three types of elastic deformations, splay, twist, and bend, and the corresponding modulus K_{11}, K_{22}, and K_{33}, known as Frank elasticity constants [5]. The bulk free energy density is given by:

$$f_n = \frac{1}{2}K_{11}(\nabla \cdot \mathbf{n})^2 + \frac{1}{2}K_{22}(\mathbf{n} \cdot \nabla \times \mathbf{n})^2 + \frac{1}{2}K_{33}|\mathbf{n} \times (\nabla \times \mathbf{n})|^2 \tag{1}$$

Thermodynamic stability requires:

$$K_{11} > 0; K_{22} > 0; K_{33} > 0 \tag{2}$$

In contrast to rod-like nematics, for disc-like nematics the bending disc's trajectories give rise to a splay deformation, and the splaying disc's trajectories give rise to a bend deformation; by disc trajectory it means the curve locally orthogonal to the director. For DNLCs, the following inequalities hold [6]:

$$K_{22} > K_{11}; \quad K_{22} > K_{33} \tag{3}$$

which indicates that planar deformations are favored.

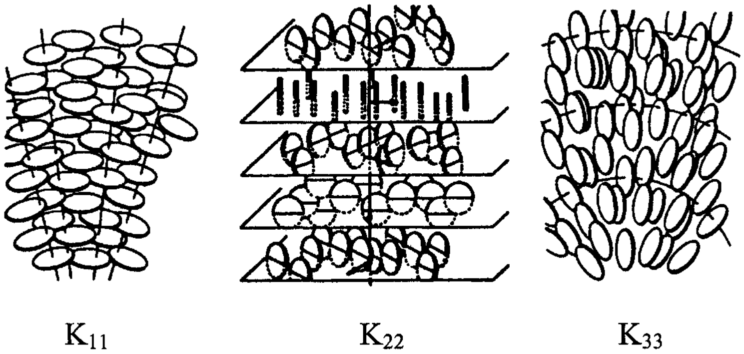

Figure 3.2: Schematics of the elastic splay (left), twist (centre), and bend (right) deformation for uniaxial discotic nematics. Note that the splay (bend) mode involves bending (splaying) of the disk's trajectories, in contrast to the case of uniaxial rod-like nematics. A disk trajectory is a curve locally orthogonal to the director. Adapted from [6].

It is known [3,4] that the observed cross-section fiber textures belong to a number of families, such as onion, radial, mixed, PAN-AM, to name a few. Figure 3.3 shows the schematics of two cross-sectional textures most commonly seen in mesophase carbon fibers. The dashed line indicates the trajectories of the molecular planes, (a) shows the planar radial (PR) texture, in which only the pure bend mode exists with one defect in the centre of strength s=+1, and (b) shows the planar polar (PP) texture, in which two modes of deformation, splay and bend, exist with two defects of the strength s=+1/2. Figure 3.3 (c), (d) are the corresponding director fields' schematics of the PP and PR textures. The defects arise due to the constraints of tangential boundary conditions and a planar 2D orientation field. Defects are singularities in the director field and are characterized by strength (1/2, 1, …) and sign (±)[5]. The strength of a disclination determines the amount of orientation distortion and the sign corresponds to the sense (i.e. clockwise or anti-clockwise) of orientation rotation while circling the defects. Since the energy of a defect scales with the square of the defect strength [5], the planar polar texture would seem to emerge, so as to minimize the elastic energy associated with orientation distortions. In addition, defects of equal sign repel each other, while defects of different sign attract. As shown below, in the PP texture, defect-defect interaction plays a critical role in the geometry of the texture. For discussions and references on rod-like nematics in cylindrical geometries, see for example [7,8]. The phase diagram of nematic textures in cylindrical geometries as a function of temperature and fiber radius in the absence of elastic anisotropy has been given by Sonnet et al [9].

Theory and simulation of liquid crystalline materials continues to be performed using macroscopic, mesoscopic, and molecular models [5]. Macroscopic models based on the Leslie-Ericksen director equations are unsuitable to simulate texture formation because defects are singularities in the orientation field. On the other hand, mesoscopic models based on the second moment of the orientation distribution function is well suited to capture the formation of liquid crystalline textures, because defects are non-singular solutions to the governing equations. A very well established mesoscopic model in liquid crystalline materials is based on the Landau-de Gennes free energy [5] and is used in this work.

The objectives of this paper are:

(1) To simulate the transient formation of the PR and PP texture which is commonly observed during the melt spinning of carbonaceous mesophase.

(2) To characterize the mechanisms of PR and PP texture selection in DNLCs.

(3) To compute a texture phase diagram, given in terms of temperature and fiber radius, and to establish the geometric and operating conditions that lead to the characteristic textures.

(4) To discuss the influence of elastic anisotropy ($K_{11} \neq K_{22} \neq K_{33}$) on the formation of fiber texture.

This paper is organized as follows. Section 2 presents the theory and the Landau-de Gennes governing equations. Section 3 discusses the computational methods to solve the model. Section 4 shows the numerical solutions of our model, and also, discusses the characteristics of the texture phase diagram and the effect of elastic anisotropy. Finally conclusions are presented.

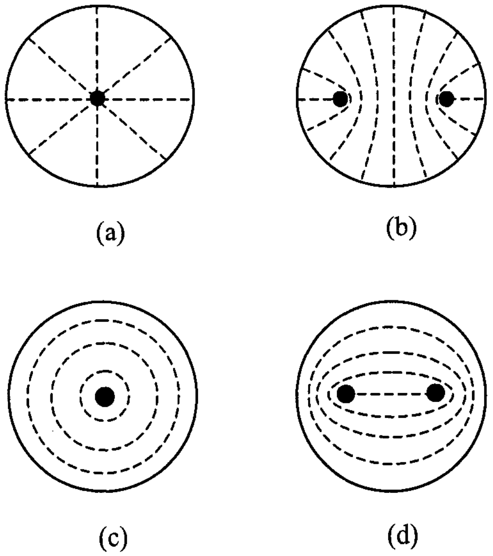

Figure 3.3: Schematics of two cross-sectional textures most commonly seen in mesophase carbon fibers. The dashed line indicates the trajectories of the molecular planes, (a) shows the planar radial (PR) texture, in which only the pure bend mode exists with one defect in the centre of strength s=+1, and (b) shows the planar polar (PP) texture, with splay and bend, and two defects of the strength s=+1/2. Figure 3 (c), (d) are the corresponding director fields' schematics of the PP and PR textures. The defects arise due to the constraints of tangential boundary conditions and a planar 2D orientation field.

3.3 Theory and Governing Equations

In this section, we present the Landau-de Gennes theory for nematic liquid crystals, and the parametric equations used to describe mesophase fiber texture formation. As mentioned above, the theory is well suited to simulate texture formation since defects are non-singular solutions to the governing equations.

3.3.1 Definition of Orientation and Alignment

The microstructure of DNLCs is characterized by a second order symmetric and traceless tensor, known generally as tensor order parameter **Q** [15]:

$$\mathbf{Q} = S(\mathbf{nn} - \frac{1}{3}\mathbf{I}) + \frac{1}{3}P(\mathbf{mm} - \mathbf{ll}) \tag{4}$$

where the following restrictions apply:

$$\mathbf{Q} = \mathbf{Q}^T;\ \mathrm{tr}(\mathbf{Q}) = 0; -\frac{1}{2} \le S \le 1; -\frac{3}{2} \le P \le \frac{3}{2} \tag{5}$$

$$\mathbf{n} \cdot \mathbf{n} = \mathbf{m} \cdot \mathbf{m} = \mathbf{l} \cdot \mathbf{l} = \mathbf{1};\ \mathbf{nn} + \mathbf{mm} + \mathbf{ll} = \mathbf{I} = \begin{bmatrix} 1 & 0 & 0 \\ 0 & 1 & 0 \\ 0 & 0 & 1 \end{bmatrix} \tag{6}$$

the uniaxial director **n** corresponds to the maximum eigenvalue $\mu_n = \frac{2}{3}S$, the biaxial director **m** corresponds the second largest eigenvalue $\mu_m = -\frac{1}{3}(S - P)$, and the second biaxial director **l** (=**n**×**m**) corresponds to the smallest eigenvalue $\mu_\ell = -\frac{1}{3}(S + P)$. The orientation is defined completely by the orthogonal director triad (**n**, **m, l**). The magnitude of the uniaxial scalar order parameter S is a measure of the molecular alignment along the uniaxial director **n**, and is given as $S = \frac{3}{2}(\mathbf{n} \cdot \mathbf{Q} \cdot \mathbf{n})$. The magnitude of the biaxial scalar order parameter P is a measure of the molecular alignment in a plan perpendicular to the direction of uniaxial director **n**, and is given as $P = \frac{3}{2}(\mathbf{m} \cdot \mathbf{Q} \cdot \mathbf{m} - \mathbf{l} \cdot \mathbf{Q} \cdot \mathbf{l})$. On the principal axes, the tensor order parameter **Q** is represented as:

$$\mathbf{Q} = \begin{bmatrix} -\frac{1}{3}(S-P) & 0 & 0 \\ 0 & -\frac{1}{3}(S+P) & 0 \\ 0 & 0 & \frac{2}{3}S \end{bmatrix} \tag{7}$$

both S and P are positive for normal DNLCs. The Landau-de Gennes model uses the tensor order parameter to describe nematic ordering. According to equation (7), the model is able to describe biaxial ($S \neq 0,\ P \neq 0$), uniaxial ($S \neq 0$, P=0), and isotropic (S=0, P=0) states.

3.3.2 Landau-de Gennes Mesoscopic Model for Liquid Crystalline Materials

According to the Landau-de Gennes model, the bulk energy density of nematic liquid crystals (NLC) in the absence of external fields is given by [10,11]:

$$\mathrm{f_b = f_0 + f_s + f_\ell \quad ; \quad f_\ell = f_{\ell 2} + f_{\ell 3}} \tag{8a,b}$$

$$\mathrm{f_s} = \mathrm{A}\mathbf{Q}:\mathbf{Q} + \mathrm{B}\mathbf{Q}:(\mathbf{Q}\cdot\mathbf{Q}) + \mathrm{C}(\mathbf{Q}:\mathbf{Q})^2 \tag{8c}$$

$$\mathrm{f_{\ell 2}} = \mathrm{L_1}\nabla\mathbf{Q}:(\nabla\mathbf{Q})^{\mathrm{T}} + \mathrm{L_2}(\nabla\cdot\mathbf{Q})\cdot(\nabla\cdot\mathbf{Q}) \tag{8d}$$

$$\mathrm{f_{\ell 3}} = \mathrm{L_3}\mathbf{Q}:(\nabla\mathbf{Q}:\nabla\mathbf{Q}) + \cdots \tag*{8(e)}$$

where A, B, C, L_1, L_2, L_3, … are coefficients of the specified terms. f_0 is the free energy density of the isotropic state. The term is related to the conventional thermodynamic parameters, like temperature and pressure, and independent to **Q**. f_s is the short-range energy density, which is responsible for the nematic-isotropic phase transition, f_ℓ is the long range energy, $f_{\ell 2}$ is the second order long range free energy density, and $f_{\ell 3}$ is the third order contribution to the long range free energy density. By assuming that **Q** is uniaxial and comparing $f_{\ell 2}$ with f_n (eqn.(1)) it is found that K_{11}=K_{33}. To remove this restriction $f_{\ell 3}$ must be non-zero. It is known that there are six different third-order expressions. For rod-like nematics it was shown that representative experimental {K_{ii}}; (ii=11, 22, 33) data is well captured by retaining only the term $\mathrm{L_3}\mathbf{Q}_{\alpha\beta}\,\mathbf{Q}_{\gamma\delta\ ,\alpha}\mathbf{Q}_{\gamma\delta\ ,\beta}$ in the $f_{\ell 3}$ expression [12]. The same approach will be used in this paper. Using the one parameter Doi model for f_s [17], the dimensionless free energy densities are given by:

$$\mathrm{f_s^*} = \frac{3}{\mathrm{U}}\left(\frac{1}{2}\left(1-\frac{1}{3}\mathrm{U}\right)\mathbf{Q}:\mathbf{Q} - \frac{1}{3}\mathrm{U}\mathbf{Q}:(\mathbf{Q}\cdot\mathbf{Q}) + \frac{1}{4}\mathrm{U}(\mathbf{Q}:\mathbf{Q})^2\right) \tag{9a}$$

$$\mathrm{f_{\ell 2}^*} = \frac{\mathrm{L_1}}{2\mathrm{ckT^*R^2}}\left[\tilde{\nabla}\mathbf{Q}:\left(\tilde{\nabla}\mathbf{Q}\right)^{\mathrm{T}}\right] + \frac{\mathrm{L_2}}{2\mathrm{ckT^*R^2}}\left(\tilde{\nabla}\cdot\mathbf{Q}\right)\cdot\left(\tilde{\nabla}\cdot\mathbf{Q}\right) \tag{9b}$$

$$\mathrm{f_{\ell 3}^*} = \frac{\mathrm{L_3}}{2\mathrm{ckT^*R^2}}\left[\mathbf{Q}:\left(\tilde{\nabla}\mathbf{Q}:\tilde{\nabla}\mathbf{Q}\right)\right] \tag{9c}$$

where U is the nematic potential, which is inversely proportional to the temperature in a thermotropic liquid crystal, and c, k, T* are the number density of discs, the Boltzmann's constant, and an absolute reference temperature just below the isotropic-nematic phase transition temperature, respectively. Comparing eqn.(1) the Landau coefficients $\{L_i\}, i=1,2,3$ are related to the Frank's constant of uniaxial LCs in the following way [12,16]:

$$L_1 = \frac{3K_{22} - K_{11} + K_{33}}{6S^2}, \quad L_2 = \frac{K_{11} - K_{22}}{S^2}, L_3 = \frac{K_{33} - K_{11}}{2S^3} \tag{10a, b, c}$$

$$K_{11} = S^2\left(2L_1 + L_2 - \frac{2}{3}SL_3\right) \tag{11a}$$

$$K_{22} = S^2\left(2L_1 - \frac{2}{3}SL_3\right) \tag{11b}$$

$$K_{33} = S^2\left(2L_1 + L_2 + \frac{4}{3}SL_3\right) \tag{11c}$$

Using eqns.(11) and inequalities (2) the following restrictions have to be obeyed under uniaxial ordering:

$$2L_1 + L_2 - \frac{2}{3}SL_3 \geq 0;\ 2L_1 - \frac{2}{3}SL_3 \geq 0;\ 2L_1 + L_2 + \frac{4}{3}SL_3 \geq 0 \tag{12a, b, c}$$

In addition, since twist is the highest elastic constant in DNLCs, the Landau coefficient L_2 is negative [14, 15]:

$$L_2<0 \tag{13}$$

Using the classical gradient flow model, the time dependent equation in terms of $\mathbf{Q}$ and $\nabla\mathbf{Q}$ is found to be [17]:

$$-\gamma(\mathbf{Q})\frac{d\mathbf{Q}}{dt} = \frac{\delta F}{\delta \mathbf{Q}} = \left(\frac{\partial f_b}{\partial \mathbf{Q}} - \nabla \cdot \frac{\partial f_b}{\partial \nabla \mathbf{Q}}\right)^{[s]} \tag{14}$$

where [s] indicates the symmetric and traceless, $\gamma(\mathbf{Q})$ is the rotational viscosity coefficient, and $\frac{\delta F}{\delta \mathbf{Q}}$ is the functional derivative of the total energy F. Substituting equation (9) into equation (14) yields the following governing equations of $\mathbf{Q}(\mathbf{x},t)$:

$$\begin{aligned}\frac{d\mathbf{Q}}{dt} &= -6\overline{Dr}\left[\frac{\partial f_b^*}{\partial \mathbf{Q}} - \nabla\cdot\frac{\partial f_b^*}{\partial \nabla\mathbf{Q}}\right]^{[s]} \\ &= -6\overline{Dr}\left\{\begin{array}{l}\frac{3}{U}\left[\left(1-\frac{1}{3}U\right)\mathbf{Q} - U\left(\mathbf{Q}\cdot\mathbf{Q}-\frac{1}{3}(\mathbf{Q}:\mathbf{Q})\mathbf{I}\right)+U(\mathbf{Q}:\mathbf{Q})\mathbf{Q}\right] \\ +\frac{L_3}{2ckT^*}\left[(\nabla\mathbf{Q}:\nabla\mathbf{Q})-\frac{1}{3}\mathrm{tr}(\nabla\mathbf{Q}:\nabla\mathbf{Q})\mathbf{I}\right]\end{array}\right\} \\ &+ 6\overline{D_r}\left[\begin{array}{l}\frac{L_1}{ckT^*}\nabla^2\mathbf{Q}+\frac{L_2}{2ckT^*}\left(\nabla(\nabla\cdot\mathbf{Q})+[\nabla(\nabla\cdot\mathbf{Q})]^T-\frac{2}{3}\mathrm{tr}[\nabla(\nabla\cdot\mathbf{Q})]\mathbf{I}\right) \\ +\frac{L_3}{ckT^*}((\nabla\cdot\mathbf{Q})\cdot\nabla\mathbf{Q})+\frac{L_3}{ckT^*}(\mathbf{Q}:(\nabla\nabla\mathbf{Q}))\end{array}\right]\end{aligned} \tag{15a}$$

$$\overline{D_r} \approx D_r\frac{1}{(1-(3/2)\mathbf{Q}:\mathbf{Q})^2},\ D_r = \frac{ckT}{6\eta} \tag{15b}$$

where $\overline{D_r}$ is the microstructure dependent rotational diffusivity, D_r is the preaveraged rotational diffusivity or isotropic diffusivity, which is independent of **Q**, and η is a viscosity. The relation between $\overline{D_r}$ and $\gamma(\mathbf{Q})$ can be read off by comparing eqns. (14,15a). Non-dimensioning equation (15) yields:

$$\frac{d\mathbf{Q}}{dt^*} = \mathbf{S}+\mathbf{L} \tag{16a}$$

$$\mathbf{S} = -\frac{1}{U}\frac{3}{U}\left[1-\frac{3}{2}(\mathbf{Q}:\mathbf{Q})\right]^{-2}\left[\left(1-\frac{1}{3}U\right)\mathbf{Q} - U\left(\mathbf{Q}\cdot\mathbf{Q}-\frac{1}{3}(\mathbf{Q}:\mathbf{Q})\mathbf{I}\right)+U(\mathbf{Q}:\mathbf{Q})\mathbf{Q}\right] \tag{16b}$$

$$\begin{aligned}\mathbf{L} &= \frac{\xi^2}{R^2}\frac{1}{U}\left[1-\frac{3}{2}(\mathbf{Q}:\mathbf{Q})\right]^{-2}\left\{\begin{array}{l}\tilde{\nabla}^2\mathbf{Q}+\frac{\tilde{L}_2}{2}\left[\tilde{\nabla}(\tilde{\nabla}\cdot\mathbf{Q})+\left[\tilde{\nabla}(\tilde{\nabla}\cdot\mathbf{Q})\right]^T-\frac{2}{3}\mathrm{tr}\left[\tilde{\nabla}(\tilde{\nabla}\cdot\mathbf{Q})\right]\mathbf{I}\right] \\ +\tilde{L}_3\left((\tilde{\nabla}\cdot\mathbf{Q})\cdot\tilde{\nabla}\mathbf{Q}\right)+\tilde{L}_3\left(\mathbf{Q}:(\tilde{\nabla}\tilde{\nabla}\mathbf{Q})\right)\end{array}\right\} \\ &-\frac{\xi^2}{R^2}\frac{1}{U}\frac{\tilde{L}_3}{2}\left[1-\frac{3}{2}(\mathbf{Q}:\mathbf{Q})\right]^{-2}\left[(\tilde{\nabla}\mathbf{Q}:\tilde{\nabla}\mathbf{Q})-\frac{1}{3}\mathrm{tr}(\tilde{\nabla}\mathbf{Q}:\tilde{\nabla}\mathbf{Q})\mathbf{I}\right]\end{aligned} \tag{16c}$$

where $t^* = t\frac{3ckT^*}{\eta}$ is dimensionless time, $U = \frac{3T^*}{T}$ is dimensionless temperature, $\xi = \sqrt{\frac{L_1}{ckT^*}}$ is molecular length scale, $\tilde{L}_2 = \frac{L_2}{L_1}$ and $\tilde{L}_3 = \frac{L_3}{L_1}$ are ratios of elastic coefficients, and R is geometry length scale (i.e. the fiber radius), **S** is the short-range contribution, and **L** is the long-range distribution.

The dimensionless parameters of the model are: U, $\mathcal{R}=\frac{R}{\xi}$, $\tilde{L}_2$ and $\tilde{L}_3$. The nematic potential U is a dimensionless temperature that controls the equilibrium order parameter S_{eq} at the phase transition. According to the Doi model of the short-range energy, the temperature dependence of S at equilibrium is [17]:

$$S_{eq}=\frac{1}{4}+\frac{3}{4}\sqrt{\left(1-\frac{8}{3U}\right)},\ U=\frac{3T^*}{T} \tag{17a,b}$$

where T* is a reference temperature just below the isotropic-nematic phase transition temperature like we defined before. For U<8/3 the stable phase is isotropic, for $8/3 \leq U \leq 3$ there is biphasic equilibrium, and for higher values of U the phase is uniaxial nematic. In this work, we have used $2.7 \leq U \leq 6.55$. The parameter $\mathcal{R}=\frac{R}{\xi}$ is the ratio of the fiber radius to the internal length scale (ξ). The internal length scale represents the characteristic size of a defect core and is usually much smaller than the system size R. In this work, we have used $0<\mathcal{R}<250$. When $\mathcal{R}<<1$, long-range energy dominates, spatial gradients are costly and homogeneous states are selected. On the other hand, when $\mathcal{R}>>1$, long-range elasticity is insignificant with respect to short-range elasticity and defects proliferate, since spatially, non-homogeneous states are energetically not costly. The elastic constants ratios $\tilde{L}_2=\frac{L_2}{L_1}$ and $\tilde{L}_3=\frac{L_3}{L_1}$ are two measures of elastic anisotropy. When $\tilde{L}_2$, $\tilde{L}_3$ are equal to zero, all elastic modes (K_{11}, K_{22}, K_{33}) have the same elastic modulus. To satisfy the thermodynamic restrictions (12,13), we set $\tilde{L}_2=-0.5$ throughout and limit the range of $\tilde{L}_3$ to: $-1.125 \leq S\tilde{L}_3 \leq 2.25$. The governing equation (16) is solved in the circle ($\tilde{r}$ =0.5) with the following boundary conditions:

t*>0, $\tilde{r}$ =0.5, **Q=Q**$_{eq}$

$$\mathbf{Q}_{eq}=S_{eq}\left(\boldsymbol{\alpha\alpha}-\frac{1}{3}\mathbf{I}\right) \tag{18}$$

where $\tilde{r}$ is the dimensionless radial distance ($\tilde{r}$=r/R), and $\tilde{r}$=0 is the centre of the computational domain (i.e. fiber axis). The Dirichlet boundary condition sets the eigenvalues of uniaxial tensor order parameter equal to its equilibrium value ($S=S_{eq}$), and the distinct eigenvector **n** parallel to the azimuthal ($\boldsymbol{\alpha}$) direction of the cylindrical coordinates system ($\tilde{r}, \alpha$). The symbol $\boldsymbol{\alpha}$ represents the unit vector along the azimuthal α direction. The initial conditions are:

$$t^*=0,\ \mathbf{Q}_{ini} = S_{ini}(\mathbf{n}_{ini}\mathbf{n}_{ini} - \frac{1}{3}\mathbf{I}) + \frac{1}{3}P_{ini}(\mathbf{m}_{ini}\mathbf{m}_{ini} - \mathbf{l}_{ini}\mathbf{l}_{ini}) \tag{19}$$

where S_{ini} and P_{ini} are infinitesimally small random numbers, and $\mathbf{n}_{ini}$, $\mathbf{m}_{ini}$, and $\mathbf{l}_{ini}$ are corresponding three random eigenvectors. The initial conditions represent an isotropic state (S=0, P=0) with thermal fluctuations in order (S, P) and orientation (**n, m, l**).

3.4 Computational Methods

The model equation (16) is a set of six coupled non-linear parabolic partial differential equations, solved in the circle, subjected the auxiliary conditions (see equations (18, 19)). The equations are solved using Galerkin Finite Elements with Lagrangean linear basis functions for spatial discretization and a fifth order Runge-Kutta-Cash-Karp time adaptive method. Convergence and mesh-independence were established in all cases using standard methods. Spatial discretization was judiciously selected taking into account the length scale of our model. As mentioned above, the Landau-de Gennes model for nematic liquid crystals has an external length scale L_e and an internal length scale L_i as follows:

$$L_e=R,\ L_i = \xi = \sqrt{\frac{L_1}{ckT^*}} \tag{20a,b}$$

where R is the fiber radius, and where in the length scale obeys $L_e \gg L_i$. If defects are present, the mesh size has to be commensurate with L_i. It should be noted that the external length scale governs the directors' orientation (**n, m, l**) while the internal length scale governs the scalar order parameter (S, P). In addition, care should be taken to select an appropriate time integration technique to overcome the intrinsic stiffness of the system. The model equations contain an internal time scale τ_i and an external time scale τ_e. The internal time scale governs the evolution of the scalar order parameters (S, P) and is given by

$$\tau_i = \frac{\eta}{ckT^*} \tag{21}$$

A much longer external time scale τ_e controls the evolution of the directors and is given by:

$$\tau_e = \frac{\eta L_e^2}{L_1} \tag{22}$$

The selected adaptive time integration scheme is able to efficiently take into account the stiffness that rises due to the disparity between time scale: $\tau_i << \tau_e$.

3.5 Results and Discussion

To visualize the fiber textures we use the solution tensor **Q**, and represent the discotic mesophase by a cuboid **C** whose axes are normal to the directors (**n**, **m**, **l**) and sides are proportional to its eigenvalues. Since **Q** has negative eigenvalues, we use $\mathbf{M} = \mathbf{Q} + \frac{1}{3}\mathbf{I}$ instead of **Q**.

3.5.1 Representative Planar Radial and Planar Polar Textures

Figures 3.4 and 3.5 show visualizations of representative PP and PR obtained by solving eqns. (16). Figure 3.4a and figure 3.5a shows the computed texture phase diagram, given in terms of nematic potential $\frac{1}{U} = \frac{T}{3T^*}$ as a function of dimensionless fiber radius $\mathcal{R} = \frac{R}{\xi}$, with the auxiliary conditions (18,19) and $2.7 \le U \le 6.55$, $0 \le \mathcal{R} \le 300$, $\tilde{L}_2 = -0.5$, $\tilde{L}_3 = 0$. The phase diagram identifies the stability of the textures as a function of temperature and fiber radius. Nanofiber favors the PR texture while lower temperature and larger fiber favors the PP texture. The full line indicates the PP and PR texture transition line, defined by critical values of the temperature and fiber size ($1/U_c$, $\mathcal{R}_c$). For the parameters used here a good fit to the transition line is:

$$\frac{-1}{\frac{1}{U} - \frac{3}{8}} = \left(\mathcal{R} - \mathcal{R}_c\right)^n; n = 0.65, \mathcal{R}_c = 37 \tag{23}$$

For large U, the transition is effected by $\mathcal{R}$ (long range), and for large $\mathcal{R}$, the transition is effected by U (short range). At large U the long range effects at the transition include changes of director distortions and biaxiality. At large $\mathcal{R}$ the short range effects on the transition include changes in the scalar order parameter and defect core size. The dots on the diagrams represent the parametric conditions applied in obtaining the solution shown in Figs. 3.4b and 3.5b. For U<8/3, the fiber is isotropic.

Figure 3.4b is a representative typical steady state visualization of **M** corresponding to the PP texture for U=6.55, $\mathcal{R}$=67, $\tilde{L}_2$=-0.5, $\tilde{L}_3$=0. It clearly shows the molecular orientation of planar polar texture, with the two s=+1/2 defects collinear with the fiber axis. The orientation of the defect-defect axis is arbitrary since the system evolves from an isotropic state that contains no texture information. The simulations show the bending distortions close to the two defects and an aligned region between the two defects. Figures 3.4c,d shows a grey-scale plot and a surface plot of the uniaxial scalar order parameter S as a function of dimensionless position (x*, y*). In the grey-scale plot a low order parameter ($S \approx 0$) is black and high order parameter ($S \approx 1$) is white. The dark dots in the figure correspond to the two s=+1/2 defects. The narrow peaks in the surface plots indicate the difference in scale between defect cores and fiber radius. At the defects' core S is small, as expected. Figures 3.4e,f show the corresponding grey-scale and surface plots of the biaxial order parameters P as a function of dimensionless position (x*, y*). In the grey-scale plot, $P \approx 0$ corresponds to black and $P \approx 1$ to white. The figure clearly shows the biaxial eigenvalues of **Q** at the two defect cores. The corresponding surface plot shows that at the defects core $P \approx 0.4$. Far from the disclination the state is uniaxial. Biaxiality arises because it reduces long range elasticity. Figure 3.5b shows a representative typical steady state visualization of the tensor order parameter **M** corresponding to the PR texture for U=2.80, $\mathcal{R}$=67, $\tilde{L}_2$=-0.5, $\tilde{L}_3$=0. There is only one defect in the centre, with the strength s=+1. The only deformation mode exist in PR texture is bend (K_{33}), because the average molecular tranjectories shown on the visualization denote splay. Figure 3.5c,d shows a grey-scale plot and a surface plot S as a function of dimensionless position (x*, y*). It's shown that in the centre of the fiber S is small. Figures 5e,f show that P increases at the centre of fiber. At the disclination center the state is almost negatively uniaxial, and the core is biaxial. Far from the disclination the state is uniaxial.

3.5.2 Effect of Twist-Driven Anisotropy on Fiber Texture Selection

In this section we set $\tilde{L}_3$=0 and characterize the effect of $\tilde{L}_2$ on fiber texture selection. The magnitude of $\tilde{L}_2$ determines the difference between twist mode (K_{22}) and the equivalent splay-bend modes ($K_{11}= K_{33}$). The thermodynamically consistent range of $\tilde{L}_2$ is found from equations (12, 13). To characterize the role of twist elastic anisotropy on texture selection mechanisms the following dimensionless total energy F* per unit length is analyzed:

$$F^* = \frac{F}{ckT^*} \cdot A^* = \int_{A^*} \left(f_s^* + f_\ell^*\right) dA^* \tag{24}$$

where A* is the area of the computational domain (circle: r*=0.5), F is the total energy density. Figure 3.6 shows the dimensionless short-range energy (top), long-range energy (middle) and total energy (bottom) as a function of dimensionless fiber radius, $\mathcal{R}$, for: U=3.05, $\tilde{L}_2$=0 (left column) and U=3.05, $\tilde{L}_2$=-0.5(right column). The discontinuity at $\mathcal{R}=\mathcal{R}_c$ corresponds to the texture PP $\Leftrightarrow$ PR transition. Since we perform transient simulations only stable solutions are captured. The left branch of each plot corresponds to the PR texture, and the right bottom branch corresponds to the PP texture. The main effect of decreasing $\tilde{L}_2$ is an horizontal shift of the energy profiles towards smaller $\mathcal{R}$ values and hence $\mathcal{R}_c(\tilde{L}_2=0)>\mathcal{R}_c(\tilde{L}_2=-0.5)$. Increasing $\mathcal{R}$ decreases short and long range energy in the PR textures, but only long range in the PP textures. The rate of these changes increases with decreasing $\tilde{L}_2$.

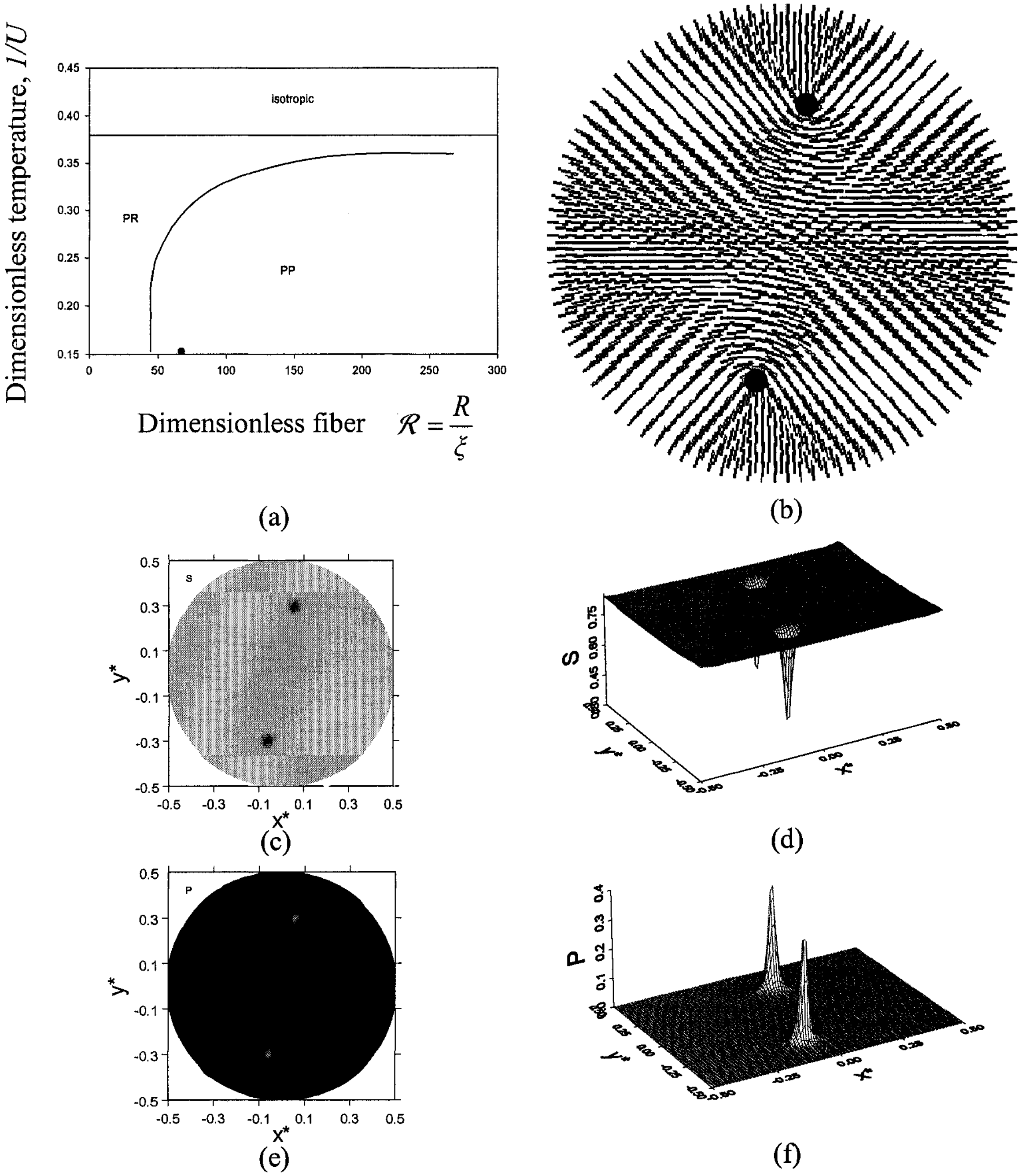

Figure 3.4: (a) Computed texture phase diagram, given in terms of nematic potential $1/U = T/3T^*$ as a function of dimensionless fiber radius $\mathcal{R} = R/\xi$, with the auxiliary conditions (18,19) and $2.7 \leq U \leq 6.55$, $0 \leq \mathcal{R} \leq 300$, $\tilde{L}_2 = -0.5$, $\tilde{L}_3 = 0$. The full line indicates the PP and PR texture transition line, defined by critical values of the temperature and fiber size ($1/U_c$, $\mathcal{R}_c$). The dot on the diagrams represent the parametric conditions applied in obtaining the solution shown in Figs. 3.4b. (b) Representative steady state visualization of M corresponding to the PP texture for U=6.55, $\mathcal{R}$=67, $\tilde{L}_2$=-0.5, $\tilde{L}_3$=0. (c-d) Grey-scale plot and a surface plot of the uniaxial scalar order parameter S as a function of dimensionless position (x*, y*). In the grey-scale plot a low order parameter ($S \approx 0$) is black and high order parameter ($S \approx 1$) is white. (e-f) Grey-scale and surface plots of the biaxial order parameters P as a function of dimensionless position (x*, y*). In the grey-scale plot, $P \approx 0$ corresponds to black and $P \approx 1$ to white.

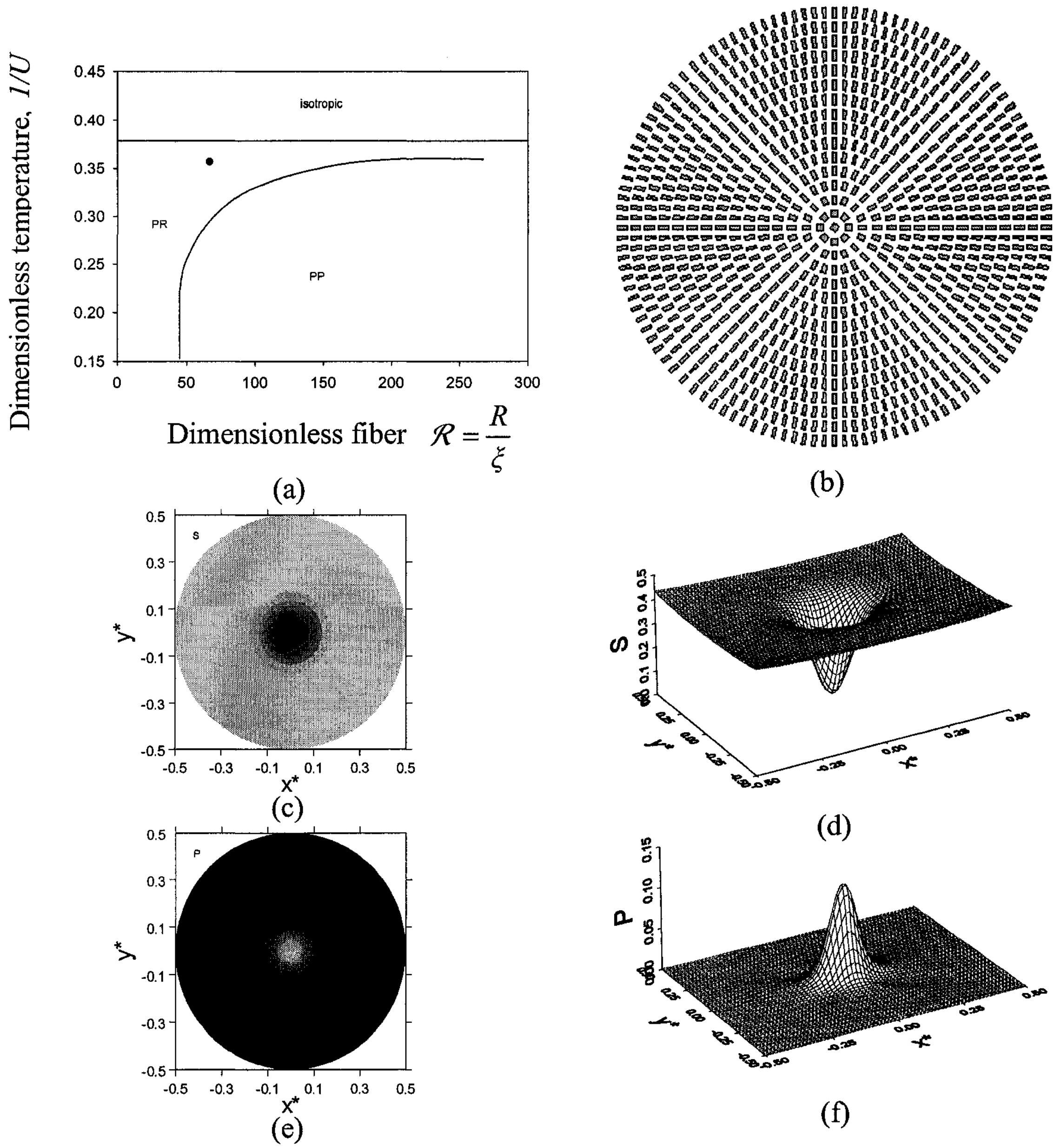

Figure 3.5: (a) Computed texture phase diagram, given in terms of nematic potential $1/U = T/3T^*$ as a function of dimensionless fiber radius $\mathcal{R} = R/\xi$, with the auxiliary conditions (18,19) and $2.7 \le U \le 6.55$, $0 \le \mathcal{R} \le 300$, $\tilde{L}_2 = -0.5$, $\tilde{L}_3 = 0$. The full line indicates the PP and PR texture transition line, defined by critical values of the temperature and fiber size ($1/U_c$, $\mathcal{R}_c$). The dot on the diagrams represent the parametric conditions applied in obtaining the solution shown in Figs. 3.5b. (b) Representative steady state visualization of tensor order parameter M corresponding to the PR texture for U=2.80, $\mathcal{R}$=67, $\tilde{L}_2$=-0.5, $\tilde{L}_3$=0. (c-d) Grey-scale plot and a surface plot of the uniaxial scalar order parameter S as a function of dimensionless position (x*, y*). In the grey-scale plot a low order parameter ($S \approx 0$) is black and high order parameter ($S \approx 1$) is white. (e-f) Grey-scale and surface plots of the biaxial order parameters P as a function of dimensionless position (x*, y*). In the grey-scale plot, $P \approx 0$ corresponds to black and $P \approx 1$ to white.

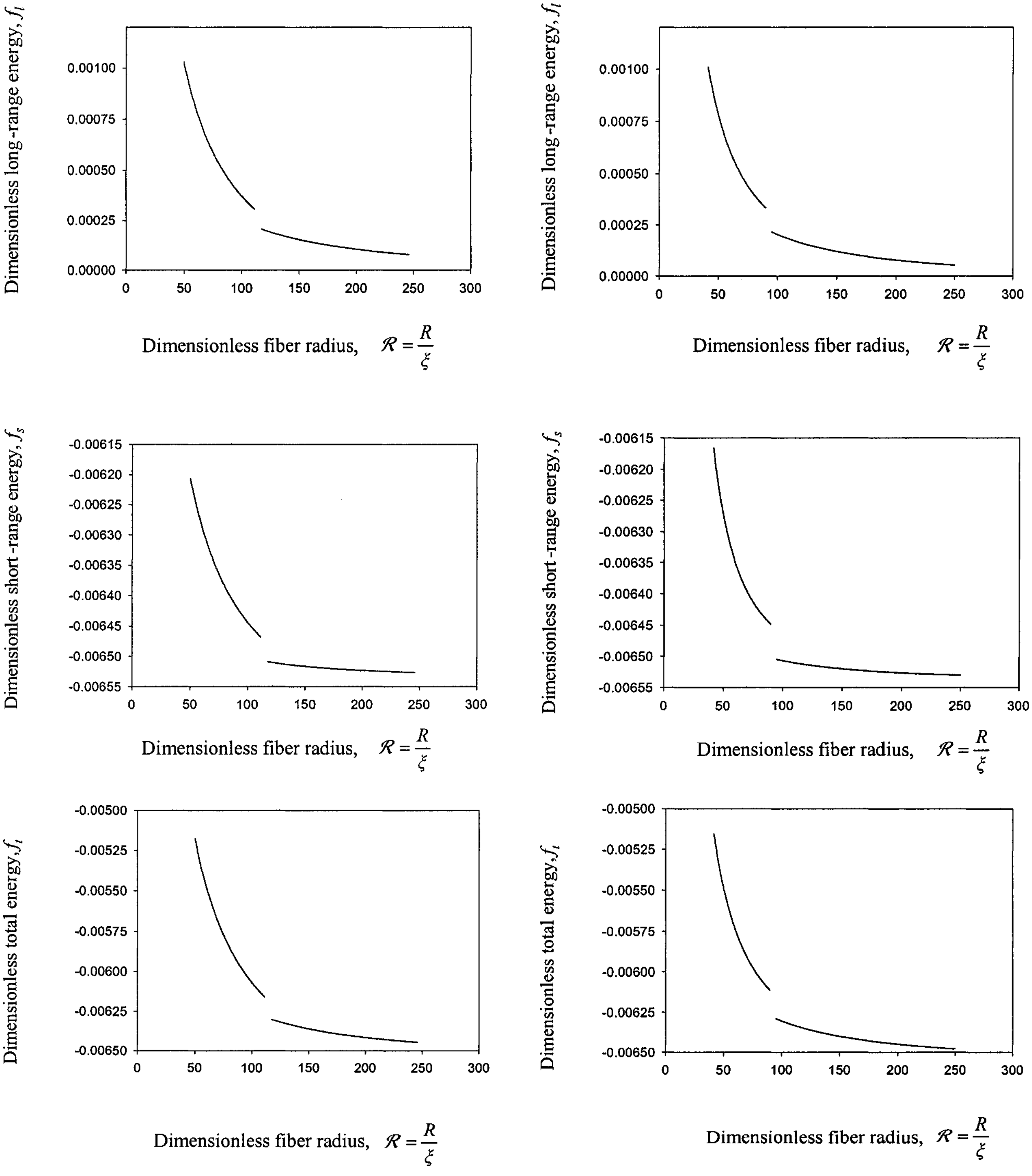

Figure 3.6: Dimensionless short-range energy (top), long-range energy (middle) and total energy (bottom) as a function of dimensionless fiber radius $\mathcal{R}$, for: U=3.05, $\tilde{L}_2$=0 (left column) and U=3.05, $\tilde{L}_2$=-0.5 (right column). The discontinuity at $\mathcal{R}=\mathcal{R}_c$ corresponds to the texture PP ⟺ PR transition.

Figure 3.7 shows the corresponding texture phase diagram for $\tilde{L}_2$=0 and $\tilde{L}_2$=-0.5. The phase transition line of $\tilde{L}_2$=-0.5 shifts left and up in comparison to the $\tilde{L}_2$=0 case. The figure shows that significant influence of $\tilde{L}_2$ on the texture transition only exists for intermediate values of U and $\mathcal{R}$. At low $\mathcal{R}$ the transition line diverges and is independent of U (i.e., vertical line). Since at low $\mathcal{R}$ the transition is sensitive to long range elasticity, and the main difference in the PR and PP textures is the difference between splay and bend deformations, no significant effect is detected because $\tilde{L}_2$ does not introduce splay-bend anisotropy. On the other hand, at high $\mathcal{R}$ the transition line asymptotes to nematic-isotropic transition line and the texture transition is independent of long range in general, including the $\tilde{L}_2$ contribution.

Figures 3.8 shows the influence of $\tilde{L}_2$ on the defect core structure for the PR and PP textures, in terms of the three eigenvalues of **Q** as a function of distance. The PR has azimuthal symmetry in the orientation field and the PP has mirror symmetry with respect to the line connecting the two s=+1/2 defects. Thus for the PR we show the eigenvalues along the radial direction while for the PP texture we show the eigenvalues as a function of dimensionless distance b* along a line that is perpendicular to the line connecting the two s=+1/2 defects and goes through one of the two equivalent defects. Figures 3.8a-b show the three eigenvalues of the tensor order parameter **Q** as a function of dimensionless distance b* for U=6.55, $\mathcal{R}$=67, $\tilde{L}_3$=0.0, $\tilde{L}_2$=0.0 (a), and U=6.55, $\mathcal{R}$=67, $\tilde{L}_3$=0.0, $\tilde{L}_2$=- 0.5 (c), corresponding to the PP textures. In both cases the state at defect center is uniaxial with $\mu_n = \mu_m > 0, \mu_l < 0$. The main effect of L_2 is the decrease in defect core size. Figures 3.8b-d show the three eigenvalues of the tensor order parameter **Q** as a function of dimensionless radial distance r* for U=2.8, $\mathcal{R}$=67, $\tilde{L}_2$=0.0, $\tilde{L}_3$=0.0 (b), and U=2.8, $\mathcal{R}$=67, $\tilde{L}_2$=-0.5, $\tilde{L}_3$=0.0 (d), corresponding to the PR textures. In both cases the state at defect center is uniaxial with $\mu_n = \mu_m > 0, \mu_l < 0$. The main effect of L_2 is the decrease in defect core size. To analyze the computed defect core features, the long range and short range energies given in eqns.(8) are expressed in terms of eigenvalues and eigenvectors. For brevity we only discuss the following expression for the PR texture:

$$f_s = -3B\mu_n\mu_m(\mu_n + \mu_m) + 2A(\mu_n^2 + \mu_n\mu_m + \mu_m^2) + 4C(\mu_n^2 + \mu_n\mu_m + \mu_m^2)^2 \tag{25a}$$

$$f_\ell = \frac{L_1}{2}\left[\mu_{n,r}^2 + \mu_{m,r}^2 + (\mu_{n,r} + \mu_{m,r})^2 + \frac{2(\mu_n - \mu_m)^2}{r^2}\right] + \frac{L_2}{2}\left[\mu_{n,r} + \frac{(\mu_n - \mu_m)}{r}\right]^2 \tag{25b}$$

where μ_i (i=m.n) are two independent eigenvalues of the tensor **Q**, and $\mu_{i,r} = \partial\mu_i/\partial r$ (i=m,n;). At the defect center the state is uniaxial [9], with $\mu_n = \mu_m > 0, \mu_l < 0$, since otherwise the long range energy diverges. In addition the common term between L_1 and L_2:

$$\left(L_1 + \frac{L_2}{2}\right)\left[\mu_{n,r} + \frac{(\mu_n - \mu_m)}{r}\right]^2 \tag{26}$$

shows that when L_2 is negative sharper gradients and smaller defect core sizes can be accommodated, as observed when comparing Figs. (3.8b,3.8c).

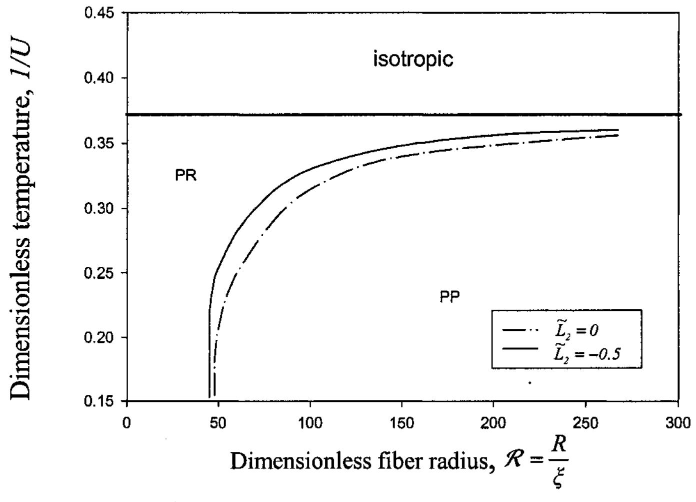

Figure 3.7: Computed texture phase diagram, given in terms of nematic potential $1/U = T/3T^*$ as a function of dimensionless fiber radius $\mathcal{R} = R/\xi$, with the auxiliary conditions (18,19) and $2.7 \le U \le 6.55$, $0 \le \mathcal{R} \le 300$, $\widetilde{L}_3 = 0$, $\widetilde{L}_2 = 0$ and $\widetilde{L}_2$=-0.5. The phase transition line of $\widetilde{L}_2$=-0.5 shifts left and up in comparison to the $\widetilde{L}_2$=0 case. The figure shows that significant influence of $\widetilde{L}_2$ on the texture transition only exists for intermediate values of U and $\mathcal{R}$.

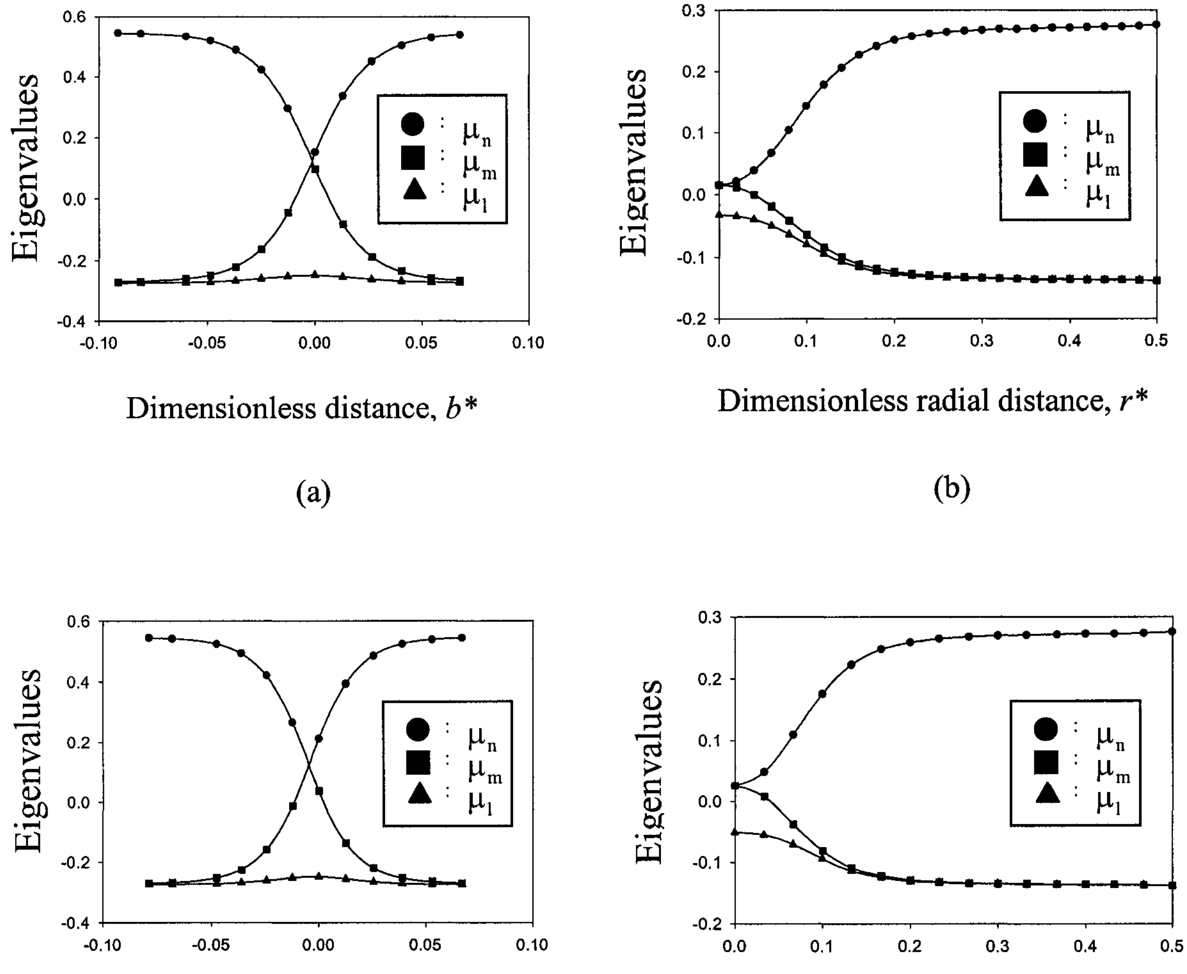

(a) (b)

(c) (d)

Figure 3.8: Eigenvalues of the tensor order parameter Q as a function of dimensionless distance b* for U=6.55, $\mathcal{R}$=67, $\tilde{L}_3$=0.0, $\tilde{L}_2$=0.0 (a), and U=6.55, $\mathcal{R}$=67, $\tilde{L}_3$=0.0, $\tilde{L}_2$=- 0.5 (c), corresponding to the PP textures. In both cases the state at defect center is uniaxial with $\mu_n = \mu_m > 0, \mu_l < 0$. The main effect of L_2 is the decrease in defect core size. Figures 3.8b-d show the three eigenvalues of the tensor order parameter Q as a function of dimensionless radial distance r* for U=2.8, $\mathcal{R}$=67, $\tilde{L}_2$=0.0, $\tilde{L}_3$=0.0 (b), and U=2.8, $\mathcal{R}$=67, $\tilde{L}_2$=-0.5, $\tilde{L}_3$=0.0 (d), corresponding to the PR textures.

3.5.3 Effect of Splay-Bend Anisotropy on Fiber Texture Selection

In this section we characterize the effect of splay-bend elastic anistropy, using $\tilde{L}_2$=-0.5 and $\tilde{L}_3 \neq 0$. Figure 3.9 shows the texture phase diagram in terms of 1/U and $\mathcal{R}$, for three values of $\tilde{L}_3$. The figure shows that as $|\tilde{L}_3|$ increases the texture transition line shifts up and left in the phase diagram. The texture transition lines retain the same features regardless of the value of $|\tilde{L}_3|$, such that at lower $\mathcal{R}$ the transition lines diverges and at high $\mathcal{R}$ the transition line asymptotes towards the nematic-isotropic transition line. As before, at high $\mathcal{R}$ long range is insignificant and hence the transition lines coalesce. On the other hand at low $\mathcal{R}$ the figure shows that the diverging transition lines do not coalesce and the effect of $\tilde{L}_3$ persists. The reason is that planar uniaxial textures are sensitive to the splay-bend anisotropy that is created when $\tilde{L}_3 \neq 0$.

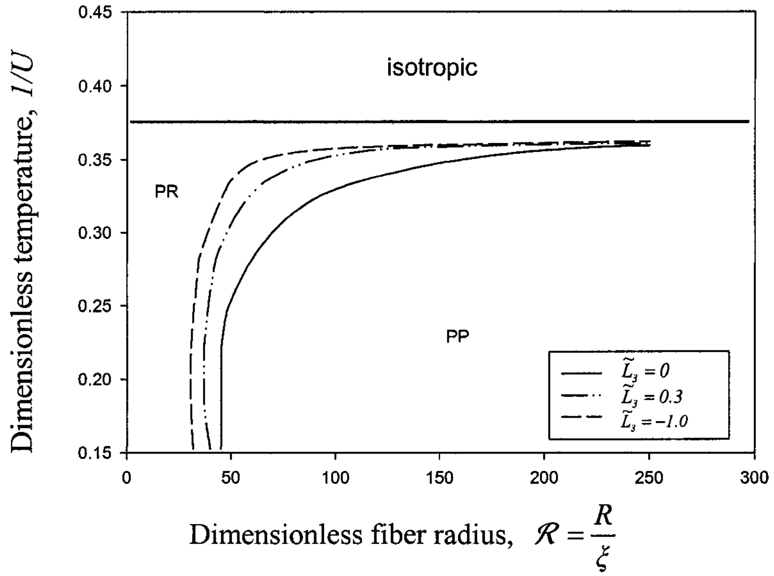

Figure 3.9: Computed texture phase diagram, given in terms of nematic potential $1/U = T/3T^*$ as a function of dimensionless fiber radius $\mathcal{R} = R/\xi$, with the auxiliary conditions (18,19) and $2.7 \leq U \leq 6.55$, $0 \leq \mathcal{R} \leq 300$, $\tilde{L}_2$=-0.5. For three values of $\tilde{L}_3$, the figure shows that as $|\tilde{L}_3|$ increases the texture transition line shifts up and left in the phase diagram.

3.5.4 Effect of Splay-Bend Anisotropy on Planar Polar Textures

The geometry of the PP textures is defined by the defect separation distance d. Using simple arguments and the Frank energy of uniaxial NLCs (see eqn.(1)) we can establish the dependence of defect separation distance d as a function of splay-bend anisotropy $d=d(K_{11}-K_{33})$ for certain limiting conditions of the vector model, which is then be tested by the numerical solutions to tensor model (eqns.(16)). In this texture the director is tangential to the boundary.

3.5.4.1 Predictions of the Vector Model

The effect of splay-bend anisotropy on isolated wedge disclination has been characterized [18]. The free energy density f_n around a defect may be written as [18]:

$$f_n = \frac{K}{2}\varphi_\alpha^2\left[1+\varepsilon\cos 2(\varphi-\alpha)\right]/r^2 \tag{27}$$

where φ, α are the orientation angle and the polar angle at a point in polar cylindrical coordinates, $\varphi_\alpha = \partial\varphi/\partial\alpha$, $K=\frac{1}{2}(K_{11}+K_{33})$, and $\varepsilon=(K_{11}-K_{33})/(K_{11}+K_{33})$ is the elastic anisotropy. Minimization of f_n leads to:

$$\varphi_{\alpha\alpha} = -\varepsilon\left[\varphi_{\alpha\alpha}\cos 2(\varphi-\alpha)+\varphi_\alpha(2-\varphi_\alpha)\sin 2(\varphi-\alpha)\right] \tag{28}$$

where $\varphi_{\alpha\alpha}=\partial^2\varphi/\partial\alpha^2$. Analytical limiting defect solutions to eqn.(28) for wedge s=+1/2, +1 disclinations can then be used to estimate d(ε).

(i) Negligible Bend: $K_{33}\to 0, \varepsilon\to +1$

A solution where the director field trajectories are all circles or parallel lines around the s=+1/2 defect is:

$$-\frac{\pi}{2}<\alpha<\frac{\pi}{2}\,,\quad \varphi=0 \quad\text{and}\quad \frac{\pi}{2}<\alpha<\frac{3\pi}{2}\,,\quad \varphi=\alpha-\frac{\pi}{2} \tag{29}$$

and a pair of these solutions can not satisfy the boundary conditions. On the other hand the s=+1 solution: $0<\alpha<2\pi$, $\varphi=\alpha+\frac{\pi}{2}$, satisfies the boundary conditions and hence in a DNLC fiber geometry this s=+1 solution corresponds to the PR texture and the defect separation distance is d (ε=+1)=0.

(ii) Splay-Bend Isotropy $K_{11} = K_{33}, \varepsilon = 0$

Sufficient increase of ε produces the decay of the s=+1 defect into two s=+1/2 defects, since some bend is replaced by splay. The location of the defects can be found by using the known boundary conditions and performing a disclination force balance between the two s=+1/2 defects and the two images lying outside the fiber [5]. If ℓ is the distance between the origin and the image of each defect, then to satisfy the director boundary conditions at r=R, the distance x between each defect and the fiber center is:

$$xR = \ell^2 \tag{30}$$

In addition a force balance between each defect and the images gives:

$$\frac{1}{\ell - x} = \frac{1}{2x} + \frac{1}{\ell + x} \tag{31}$$

which gives the following defect-defect distance d=2x:

$$d^* = \frac{d}{2R} = \frac{1}{\sqrt[4]{5}} \tag{32}$$

(iii) Negligible splay: $K_{11} \to 0, \varepsilon \to -1$

A defect s=+1/2 solution consists of straight lines director field trajectories:

$$-\frac{\pi}{2} < \alpha < \frac{\pi}{2}\ , \quad \varphi = \alpha \quad \text{and} \quad \frac{\pi}{2} < \alpha < \frac{3\pi}{2}\ , \quad \varphi = \frac{\pi}{2} \tag{33}$$

A pair of such solutions can only satisfy the boundary conditions at two points when the defects lie next to the fiber rim. Thus some bending is necessary. In addition to minimize the necessary bending to join straight lines the defects should be as far apart as possible. In a DNLC fiber geometry the solution that best avoids bending corresponds to the PP texture and d(ε→-1)=R-r_c. In summary, the inequalities driven by splay-bend elastic anisotropy are:

$$d^*(\varepsilon \to -1) = 1 > d^*(\varepsilon = 0) = \frac{1}{\sqrt[4]{5}} > d^*(\varepsilon = +1) = 0 \tag{34}$$

Splay-avoidance leads to the PR texture and bend avoidance to the PP textures. The vector model can not predict the elastic-anisotropy driven texture transitions because the defect reaction $s = +1 \leftrightarrow 2\,s = +1/2$ takes place.

3.5.4.2 Numerical Solutions to the Tensor Model

As mentioned above $\tilde{L}_3$ defines the K_{11} - K_{33} difference:

$$K_{11} - K_{33} = -2L_3S^3 \tag{35}$$

When $\tilde{L}_3 < \tilde{L}_{3c}$, $K_{11} > (1+ c^2)\ K_{33}$, the system will avoid the splay mode, and the preferred fiber texture is PR; c denotes a constant. On the other hand when $\tilde{L}_3 > \tilde{L}_{3c}$, $K_{11} > (1+ c^2)\ K_{33}$, the system will try to avoid the bend mode, and the preferred fiber texture is PP with two defects on the rim collinear with the fiber axis.

Figure 3.10 shows the dimensionless defect distance d* as a function of $\tilde{L}_3$ for $\mathcal{R}$=67, $\tilde{L}_2$=-0.5, and U=6.55(top), 5.55(middle), and 4.55(bottom). The dots for $\tilde{L}_3 < \tilde{L}_{3c}$ correspond to the PR texture and the full line corresponds to the PP texture. Note that in Figure 3.10 the minimum value of $\tilde{L}_3$ is set by the thermodynamic stability restriction $-1.125 \le S\tilde{L}_3$. The horizontal line indicates the case of $\tilde{L}_3$=0, when $d^* = 1/\sqrt[4]{5}$ [19]. The numerical solutions confirm the theoretical result for all values of U. The computations confirm the expected inequalities (34). When $\tilde{L}_3$ increases, the distance of two defects also increases and eventually asymptotes to the edge of the fiber. Since the boundary conditions are fixed the defects' location cannot be right on the edge. The critical value of $\tilde{L}_3 = \tilde{L}_{3c} \approx -1.2$ and is within our computational scheme nearly independent of U. In terms of the vector model, using S=0.8, the critical splay-bend anisotropy is ε=-0.75.

Figure 3.11a shows the visualization of the **M** tensor order parameter for $\tilde{L}_3<0$ (U=6.55, $\mathcal{R}$=67, $\tilde{L}_2$=-0.5, $\tilde{L}_3$=-1.3), corresponding to the PR texture with only bend present. Figure 3.11b shows the visualization of the **M** tensor order parameter for $\tilde{L}_3>0$ (U=6.55, $\mathcal{R}$=67, $\tilde{L}_2$=-0.5, $\tilde{L}_3$=1.5) corresponding to the PP texture with an aligned center region and strong splay next to the s=+1/2 defects, now located next to the fiber rim.

In contrast to the texture transitions driven by (U, $\mathcal{R}$) discussed above, the transition here is driven by splay-bend elastic anisotropy ($\tilde{L}_3 \neq 0$). Figure 3.12 shows the second order long-range energy ($f_{2\ell}(\nabla \mathbf{Q})$) profile in terms of $\tilde{L}_3$ with the same parametric conditions of figure 10. The dots correspond to PR and the curve to the PP texture. The dramatic change of long-range energy at $\tilde{L}_3$=-1.2 corresponds to the texture transition point due to splay-bend elastic anisotropy. The minimum long-range energy happens when $\tilde{L}_3$ is close to 0.

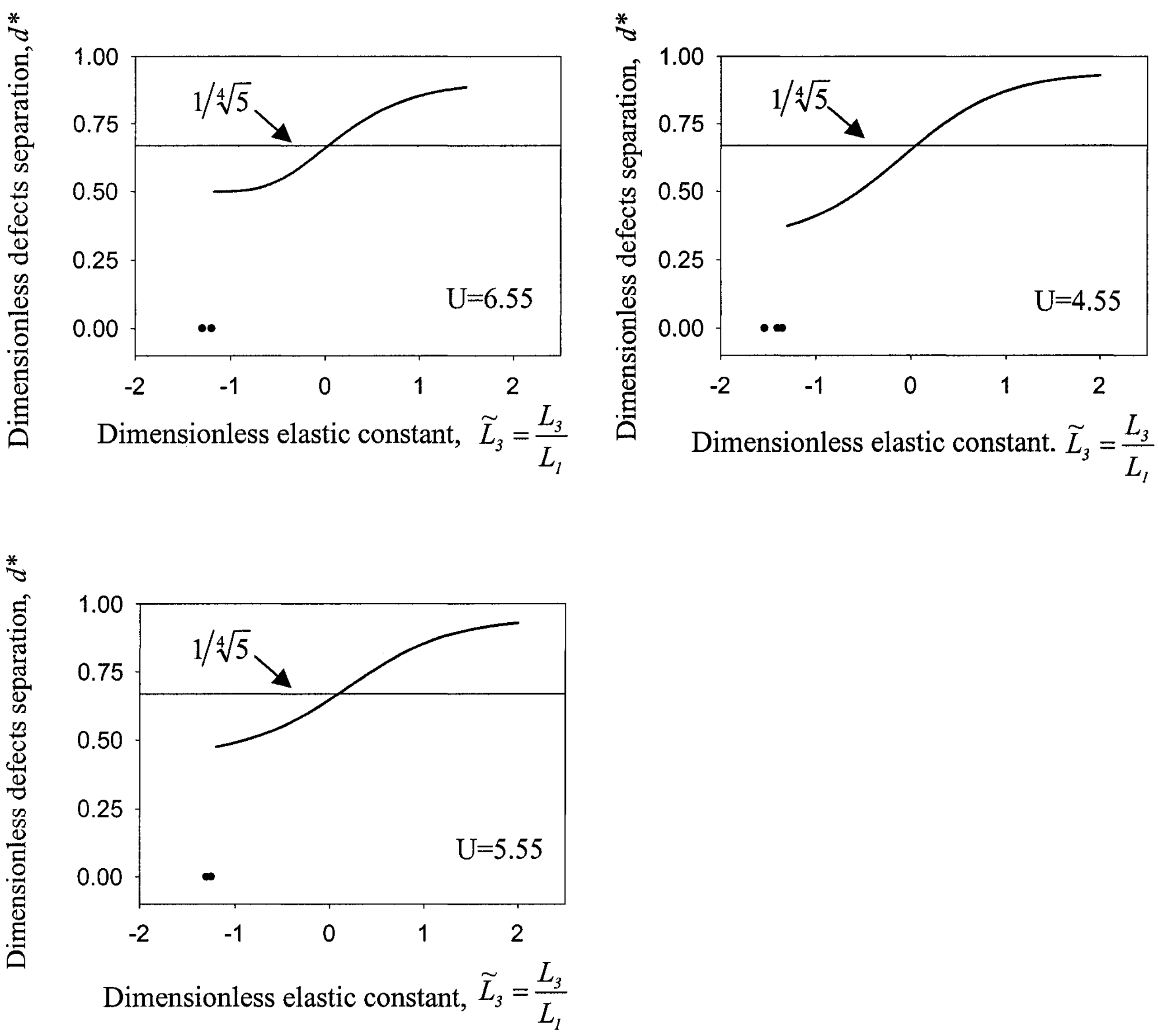

Figure 3.10: Dimensionless defect distance d* as a function of $\tilde{L}_3$ for $\mathcal{R}$=67, $\tilde{L}_2$=-0.5, and U=6.55(top), 5.55(middle), and 4.55(bottom). The dots for $\tilde{L}_3 < \tilde{L}_{3c}$ correspond to the PR texture and the full line corresponds to the PP texture. Note that in Figure 3.10 the minimum value of $\tilde{L}_3$ is set by the thermodynamic stability restriction $-1.125 \le S\tilde{L}_3$. The horizontal line indicates the case of $\tilde{L}_3$=0, when d*=$1/\sqrt[4]{5}$ [19]. The numerical solutions confirm the theoretical result for all values of U. The computations confirm the expected inequalities (33). When $\tilde{L}_3$ increases, the distance of two defects also increases and eventually asymptotes to the edge of the fiber. Since the boundary conditions are fixed, the defects' location cannot be right on the edge. The critical value of $\tilde{L}_3 = \tilde{L}_{3c} \approx -1.2$ and is within our computational scheme nearly independent of U. In terms of the vector model, using S=0.8, the critical splay-bend anisotropy is ε=-0.75.

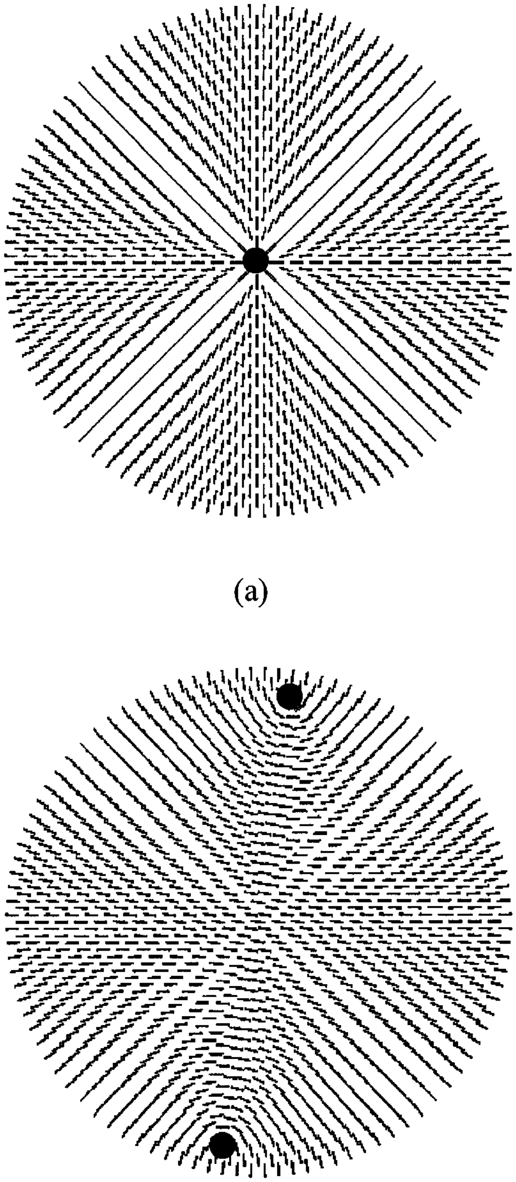

(a)

(b)

Figure 3.11: (a) Computed visualization of the M tensor order parameter for $\tilde{L}_3<0$ (U=6.55, $\mathcal{R}$=67, $\tilde{L}_2$=-0.5, $\tilde{L}_3$=-1.3), corresponding to the PR texture with only bend present. (b) Computed visualization of the M tensor order parameter for $\tilde{L}_3>0$ (U=6.55, $\mathcal{R}$=67, $\tilde{L}_2$=-0.5, $\tilde{L}_3$=1.5) corresponding to the PP texture with an aligned center region and strong splay next to the s=+1/2 defects, now located next to the fiber rim.

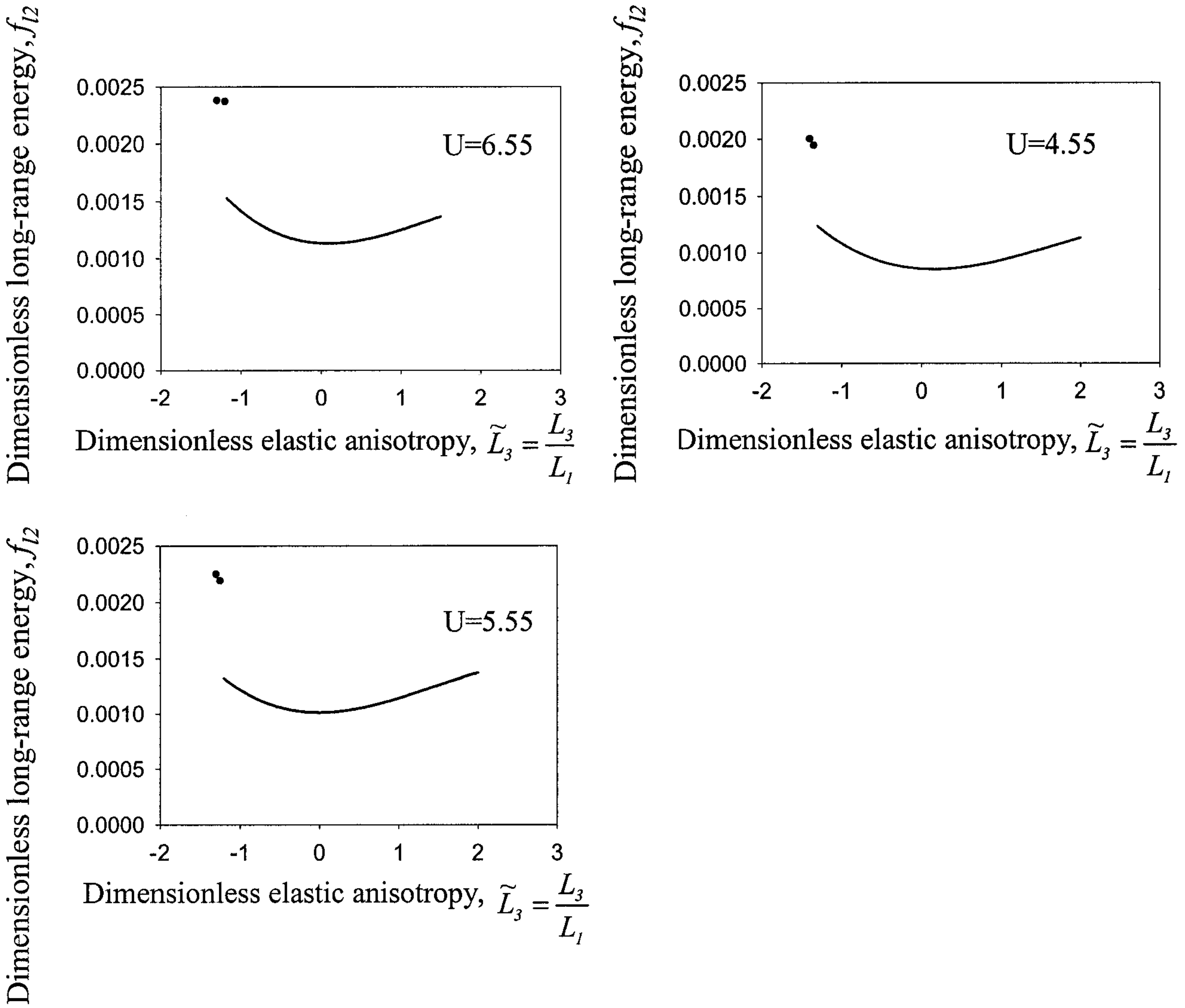

Figure 3.12: Second order long-range energy ($f_{2\ell}(\nabla \mathbf{Q})$) profile as a function of $\tilde{L}_3$ with the same parametric conditions of figure 3.10. The dots correspond to PR and the curve to the PP texture. The dramatic change of long-range energy at $\tilde{L}_3$=-1.2 corresponds to the texture transition point due to splay-bend elastic anisotropy. The minimum long-range energy happens when $\tilde{L}_3$ is close to 0.

Conclusions

A model to describe the texture formation in mesophase carbon fibers has been developed, implemented, and shown to replicate commonly observed cross-sectional carbon fiber textures of industrial relevance. The model is based on the classical Landau-de Gennes theory for liquid crystals and has been adapted to describe discotic carbonaceous mesophases. The model is able to predict the formation of planar radial and planar polar textures. The parametric conditions of their stability in terms of temperature and fiber radius have been computed. Lower temperature and thicker fibers tend to select the planar polar texture and higher temperature and thin fibers tend to promote the emergence of the planar radial texture, in agreement with [9]. The influence of elastic anisotropy to the fiber texture formation is thoroughly discussed. It is found that splay-bend anisotropy influences the fiber texture much more than the twist term. Splay (bend) avoidance leads to the planar radial (polar) texture. The importance of splay-bend anisotropy is completely explained by the Frank elastic theory. The new results presented in this paper contribute towards a better understanding of the principles that control the cross-section texture selection during the melt spinning of mesophase carbon.

Acknowledgement

This grant is supported by a grant from the Donors of The Petroleum Research Fund (PRF) administered by the American Chemical Society.

Bibliography

[1] McHugh, J. J., 1994, *Ph.D Thesis,* Clemson University.

[2] Hurt, R. H. and Chen, Z. Y., 2000, *Physics Today,* **March,** 39.

[3] Peebles, L. H. Jr., 1995, *Carbon Fibers-Formation, Structure, and Properties* (Boca Raton, FL: CRC).

[4] J. E. Zimmer and J.L. White, 1983, *Advances in Liquid Crystals*, **5**, 157.

[5] de Gennes, P. G. and Prost, J., 1993, *The Physics of Liquid Crystal* 2nd edn (Oxford: Clarendon).

[6] Sokalski, K. and Ruijgrok, T. W., 1982, *Physica,* **113A**, 126.

[7] N. Schopohl and T.J. Sluckin, 1987, *Phys. Rev. Letters*, 59, 2582.

[8] G.P. Crawford and S. Zumer, 1995, *Liquid Crystals* (World Scientific), 331.

[9] Sonnet, A., Kilian, A. and Hess, S., 1995, *Physical Review E,* **52,** 52.

[10] Longa, L., Monselesan, D. and Trebin, H. R., 1987, *Liquid Crystals,* vol. **2,** no. 6, 769.

[11] Berreman, D. W. and Meiboom, S., 1984, *Physical Review A*, vol. **30**, no. 6, 1955

[12] Schiele, K. and Trimper, S., 1983, *Phys. Stat. Sol. (b),* **118**, 267

[13] Tsuji, T. and Rey, A. D., 1997, *J. Non-Newtonian Fluid Mech.*, **73,** 127.

[14] Osipov, M. A. and Hess, S., 1993, *Molecular Physics*, **78**, No. 5, 1991

[15] Singh, A. P., 2000, *Ph.D Thesis,* Mcgill University.

[16] Beris, A. N. and Edwards, B. J., 1994, *Thermodynamics of flowing systems* (Oxford: Claredon).

[17] Doi, M. and Edwards, B. J., 1986, *The Theory of Polymer Dynamics* (Oxford: Clarendon).

[18] Chandrasekhar, S., 1992, *Liquid Crystals 2nd edn* (Cambridge University Press).

[19] Yan, J. and Rey, A. D., 2001, *Modeling Simul. Mater. Sci. Eng.*, (submitted).

[20] Wang, L. and Rey, A. D., 1997, *Modeling Simul. Mater. Sci. Eng.*, **5,** 67.

Chapter 4

Theory and Simulation of Texture Formation in Mesophase Carbon Fibers

4.1 Abstract

Carbonaceous mesophases are spun into high performance carbon fibers using the melt spinning process. The spinning process produces a wide range of different fiber textures whose origins are not well understood. Planar polar (PP) and planar radial (PR) textures are two ubiquitous ones. This paper presents the theory and simulations of the formation process of the PP texture using the Landau-de Gennes mesoscopic theory for discotic liquid crystals, including defect nucleation, defect migration, and overall texture geometry. The simulated PP texture geometry is thoroughly explained using analytical methods. The computed PP and PR textures phase diagram, given in terms of temperature and fiber radius, is used to establish the processing conditions and geometric factors that lead to the selection of these textures.

4.2 Introduction

Carbonaceous mesophase, such as coal tar and petroleum pitches, are used in the industrial manufacturing of mesophase carbon fiber. This relatively new carbon fiber is more competitive than the conventional one made from the acrylic precursors in several application areas [1]. The thermodynamic phase that describes carbonaceous mesophases is the discotic nematic liquid crystal state [2]. Liquid crystals are intermediate (i.e. mesophase) phases, typically found for anisodiametric organic molecules, which exist between the higher temperature isotropic liquid state and the lower temperature crystalline state. Carbonaceous mesophases are composed of disk-like molecules. Figure 4.1 shows the molecular geometry, positional disorder, and uniaxial orientational order of discotic nematic liquid crystals. The partial orientational order of the molecular unit normal **u** is along the average orientation or director **n** (**n**·**n**=1). The name discotic distinguishes the molecular geometry and the name nematic identifies the type of liquid crystalline orientational order.

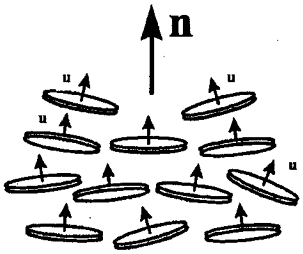

Figure 4.1: Definition of director orientation of a uniaxial discotic nematic liquid crystalline material. The director **n** is the average orientation of the unit normals to the disk-like molecules in a discotic nematic phase.

The industrial fabrication of mesophase carbon fiber using the conventional melt spinning process typically produces micrometer-sized cylindrical filaments whose cross sectional area displays a variety of transverse textures [3], that is, different spatial arrangements of the average orientation **n** on the plane perpendicular to the fiber axis. The selection mechanisms that drive the texture formation pattern are at present not well understood, but due to the strong structure-properties correlations, they are essential for product optimization.

Discotic nematic liquid crystals, such as carbonaceous mesophases, are anisotropic visco-elastic materials, whose properties depend on the average molecular orientation. A question of fundamental importance to the melt spinning of carbonaceous mesophases is to determine how elastic and viscous mechanisms affects the fiber process-induced structuring and cross-sectional fiber textures' selection. When considering elastic mechanisms, it is necessary to identify the three fundamental elastic modes of these materials. Figure 4.2 shows the three types of elastic deformations, known as splay, twist, and bend, and the corresponding modulus K_{11}, K_{22}, and K_{33}, known as Frank elasticity constants [4]. Note that in contrast to rod-like nematics, for disc-like nematics the bending disc's trajectories give rise to a splay deformation, and the splaying disc's trajectories give rise to a bend deformation; by disc trajectory it means the curve locally orthogonal to the director. For disc-like liquid crystals, it is known that the twist constant (K_{22}) is greater than the splay (K_{11}) and bend (K_{33}) constants [5].

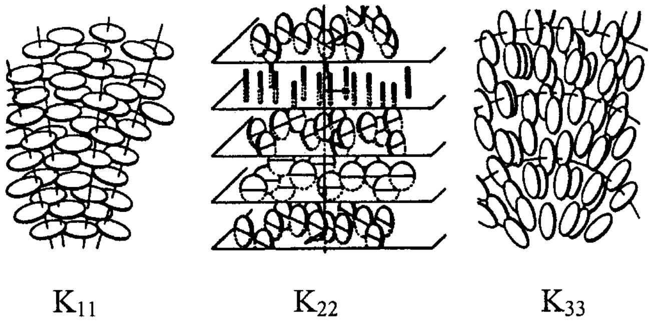

Figure 4.2: Schematics of the elastic splay (left), twist (center), and bend (right) deformation for uniaxial discotic nematics. Note that the splay (bend) mode involves bending (splaying) of the disk's trajectories, in contrast to the case of uniaxial rod-like nematics. A disk trajectory is a curve locally orthogonal to the director. Adapted from [5].

It has been known [3] that the observed cross-section fiber textures belong to a numbers of families, such as onion, radial, mixed, PAN-AM, to name a few. Figure 4.3 shows the schematics of two cross-sectional textures most commonly seen in mesophase carbon fibers. The dashed line indicates the trajectories of the molecular planes, (a) shows the planar radial (PR) texture, in which only the pure bend mode exists with one defect in the center of strength +1, and (b) shows the planar polar (PP) texture, in which two modes of deformation, splay and bend, couple in the system with two defects of the strength +1/2. The defects in these textures arise because in a cylindrical geometry, it is impossible to tangentially align the directors at the surface without introducing singularities. Defects are singularities in the director field and are characterized by strength (1/2, 1, ...) and sign (±)[4]. The strength of a disclination determines the amount of orientation distortion and the sign corresponds to the sense (i.e. clockwise or anti-clockwise) of orientation rotation while circling the defects. Since the energy of a defect scales with the square of a defect [4], the planar polar texture would seem to emerge, so as to minimize the elastic energy associate with defect distortions. In addition, defects of equal sign repel each other, while defects of different sign attract. As shown below, the PP texture, defect-defect interaction plays a critical role in the geometry of the texture.

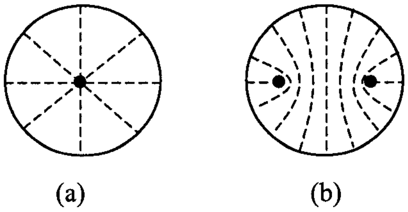

Figure 4.3: Schematics of transverse textures of actual mesophase carbon fibers. (a) The planar radial (PR) texture, in which the pure bend mode (K_{33}) exists with one defect in the center of strength +1. (b) The planar polar (PP) texture, in which two modes of deformation, splay (K_{11}) and bend (K_{33}), couple in the system with two defects of the strength +1/2.

Theory and simulation of liquid crystalline materials continues to be performed using macroscopic, mesoscopic, and molecular models [4]. Macroscopic models based on the Leslie-Erickson director equations are unsuitable to simulate texture formation because defects are singularities in the orientation field. On the other hand, mesoscopic model based on the second moment of the orientation distribution function is well suited to capture liquid crystalline textures, because defects are non-singular solutions to the governing equations. A very well established mesoscopic model in liquid crystalline materials is based on the Landau-de Gennes free energy [4] and is adopted and used in this work.

The objectives of this paper are:

(1) To simulate the transient formation of the planar polar texture that is commonly observed during the melt spinning of carbonaceous mesophase.

(2) To characterize the elastic driving forces those promote the selection of the planar polar texture.

(3) To provide a full geometric characterization of the planar polar textures in terms of defect locations.

(4) To present and discuss the planar radial-planar polar fiber texture phase diagram, given in terms of temperature and fiber radius, and to establish the geometric and operating conditions that lead to the characteristic textures.

This paper is organized as follows. Section 2 presents the theory and the Landau-de Gennes governing equations. Section 3 presents an analytic geometric analysis of the planar polar texture that yields closed form results. Section 4 shows the numerical solutions of our model that verify the analytical predictions we made in section 3, and also, discusses the characteristics of the texture evolution and the texture phase diagram. Finally conclusions are presented.

4.3 Theory and Governing Equations

In this section, we present the Landau-de Gennes theory for nematic liquid crystals, and the parametric equations used to describe mesophase fiber texture formation. As mentioned above, the theory is well suited to simulate texture formation since defects are non-singular solutions to the governing equations.

4.3.1 Definition of Orientation and Alignment

The microstructure of the discotic nematic liquid crystals is characterized by a second order symmetric and traceless tensor, known generally as tensor order parameter **Q** [10]:

$$\mathbf{Q} = \mathrm{S}(\mathbf{nn} - \frac{1}{3}\mathbf{I}) + \frac{1}{3}\mathrm{P}(\mathbf{mm} - \mathbf{ll}) \tag{1}$$

where the following restrictions apply:

$$\mathbf{Q} = \mathbf{Q}^{\mathrm{T}};\ \mathrm{tr}(\mathbf{Q}) = 0; -\frac{1}{2} \le \mathrm{S} \le 1; -\frac{3}{2} \le \mathrm{P} \le \frac{3}{2} \tag{2}$$

$$\mathbf{n}\cdot\mathbf{n}=\mathbf{m}\cdot\mathbf{m}=\mathbf{l}\cdot\mathbf{l}=1;\ \mathbf{nn}+\mathbf{mm}+\mathbf{ll}=\mathbf{I}=\begin{bmatrix}1 & 0 & 0\\ 0 & 1 & 0\\ 0 & 0 & 1\end{bmatrix} \tag{3}$$

the uniaxial director **n** corresponds to the maximum eigenvalue $\frac{2}{3}\mathrm{S}$, the biaxial director **m** corresponds the second largest eigenvalue $-\frac{1}{3}(\mathrm{S}-\mathrm{P})$, and the second biaxial director **l** (=**n**×**m**) corresponds to the smallest eigenvalue $-\frac{1}{3}(\mathrm{S}+\mathrm{P})$. The orientation is defined completely by the orthogonal director triad (**n**, **m**, **l**). The magnitude of the uniaxial scalar order parameter S is a measure of the molecular alignment along the uniaxial director **n**, and is given as $\mathrm{S}=\frac{3}{2}(\mathbf{n}\cdot\mathbf{Q}\cdot\mathbf{n})$. The magnitude of the biaxial scalar order parameter P is a measure of the molecular alignment in a plan perpendicular to the direction of uniaxial director **n**, and is given as $\mathrm{P}=\frac{3}{2}(\mathbf{m}\cdot\mathbf{Q}\cdot\mathbf{m}-\mathbf{l}\cdot\mathbf{Q}\cdot\mathbf{l})$. On the principal axes, the tensor order parameter **Q** is represented as:

$$\mathbf{Q}=\begin{bmatrix}-\frac{1}{3}(\mathrm{S}-\mathrm{P}) & 0 & 0\\ 0 & -\frac{1}{3}(\mathrm{S}+\mathrm{P}) & 0\\ 0 & 0 & \frac{2}{3}\mathrm{S}\end{bmatrix} \tag{4}$$

both S and P are positive for normal disc-like uniaxial nematic liquid crystals.

The Landau-de Gennes model uses the tensor order parameter to describe nematic ordering. According to equation (4), the model is able to describe biaxial ($\mathrm{S}\neq 0$, $\mathrm{P}\neq 0$), uniaxial ($\mathrm{S}\neq 0$, P=0), and isotropic (S=0, P=0) states. Defects are regions of molecular size in which orientational order (S, P) sharply decrease. These localized disordered regions are in principle captured by mesoscopic models since **Q** remains well behaved.

4.3.2 Landau-de Gennes Mesoscopic Model for Liquid Crystalline Materials

According to the Landau-de Gennes model, the bulk energy density of nematic liquid crystals (NLC) in the absence of external fields is given by [8]:

$$f_b = f_s + f_l \qquad (5)$$

where f_s is the short-range energy density, which is responsible for the nematic-isotropic phase transition, and f_l is elastic free energy density, also known as Frank energy, which contains long range gradient contributions to the system.

The dimensionless free energy densities f_s and f_l of thermotropic liquid crystals, in terms of the second order tensor **Q**, are given by:

$$f_s = \frac{3}{U}\left(\frac{1}{2}\left(1-\frac{1}{3}U\right)\mathbf{Q}:\mathbf{Q}-\frac{1}{3}U\mathbf{Q}:(\mathbf{Q}\cdot\mathbf{Q})+\frac{1}{4}U(\mathbf{Q}:\mathbf{Q})^2\right) \qquad (6a)$$

$$f_l = \frac{L_1}{2ckT^*}\left[\nabla\mathbf{Q}:(\nabla\mathbf{Q})^T\right]+\frac{L_2}{2ckT^*}(\nabla\cdot\mathbf{Q})\cdot(\nabla\cdot\mathbf{Q}) \qquad (6b)$$

where U is the nematic potential, which is related to the temperature in thermotropic liquid crystal, and c, k, T* are the number density of the discs, the Boltzmann's constant, and an absolute reference temperature just below the isotropic-nematic phase transition temperature respectively. The symbol L_1 and L_2 are Landau coefficients and are related to the Frank's constant of uniaxial LC's in the following way [11]:

$$L_1 = \frac{K_{22}}{2S^2} \quad L_2 = \frac{K-K_{22}}{S^2} \qquad (7a,b)$$

which implies the following elastic anisotropy restrictions: $K = K_{11} = K_{33} \neq K_{22}$. Thermodynamic stability restrictions impose the following inequality [9]:

$$L_1>0,\ 3L_1+5L_2>0 \qquad (8)$$

in addition, the molecular geometry involved in the discotic nematic phase requires that [10]:

$$L_2<0 \qquad (9)$$

Using the classical gradient flow model, the time dependent equation in terms of **Q** and $\nabla\mathbf{Q}$ is found to be [12]:

$$-\gamma(\mathbf{Q})\frac{d\mathbf{Q}}{dt}=\frac{\delta F}{\delta \mathbf{Q}}=\left(\frac{\partial f_s}{\partial \mathbf{Q}}-\nabla\cdot\frac{\partial f_l}{\partial \nabla \mathbf{Q}}\right)^{[s]} \tag{10}$$

where [s] indicates the symmetric and traceless, $\gamma(\mathbf{Q})$ is a phenomenological kinetic coefficient, and $\frac{\delta F}{\delta \mathbf{Q}}$ is the functional derivative of the total energy F. substituting equation (6) into equation (10) yields the following governing equations of $\mathbf{Q}(\mathbf{x},t)$:

$$\begin{aligned}\frac{d\mathbf{Q}}{dt}&=-6\overline{Dr}\frac{3}{U}\left[\left(1-\frac{1}{3}U\right)\mathbf{Q}-U\left(\mathbf{Q}\cdot\mathbf{Q}-\frac{1}{3}(\mathbf{Q}:\mathbf{Q})\mathbf{I}\right)+U(\mathbf{Q}:\mathbf{Q})\mathbf{Q}\right]\\&+6\overline{Dr}\left[\frac{L_1}{ckT^*}\nabla^2\mathbf{Q}+\frac{L_2}{2ckT^*}\left(\nabla(\nabla\cdot\mathbf{Q})+[\nabla(\nabla\cdot\mathbf{Q})]^T-\frac{2}{3}\mathrm{tr}[\nabla(\nabla\cdot\mathbf{Q})]\mathbf{I}\right)\right]\end{aligned} \tag{11}$$

$$\overline{Dr}\approx Dr\frac{1}{\left(1-(3/2)\mathbf{Q}:\mathbf{Q}\right)^2}\quad Dr=\frac{ckT}{6\eta}$$

where $\overline{Dr}$ is the microstructure dependent rotational diffusivity, Dr is the preaveraged rotational diffusivity or isotropic diffusivity, which is independent of $\mathbf{Q}$, and η is a viscosity. Non-dimensioning equation (11) yields:

$$\begin{aligned}\frac{d\mathbf{Q}}{dt^*}&=-\frac{1}{U}\frac{3}{U}\left[1-\frac{3}{2}(\mathbf{Q}:\mathbf{Q})\right]^{-2}\left[\left(1-\frac{1}{3}U\right)\mathbf{Q}-U\left(\mathbf{Q}\cdot\mathbf{Q}-\frac{1}{3}(\mathbf{Q}:\mathbf{Q})\mathbf{I}\right)+U(\mathbf{Q}:\mathbf{Q})\mathbf{Q}\right]+\\&\frac{\xi^2}{R^2}\frac{1}{U}\left[1-\frac{3}{2}(\mathbf{Q}:\mathbf{Q})\right]^{-2}\left\{\tilde{\nabla}^2\mathbf{Q}+\frac{\tilde{L}_2}{2}\left[\tilde{\nabla}(\tilde{\nabla}\cdot\mathbf{Q})+[\tilde{\nabla}(\tilde{\nabla}\cdot\mathbf{Q})]^T-\frac{2}{3}\mathrm{tr}[\tilde{\nabla}(\tilde{\nabla}\cdot\mathbf{Q})]\mathbf{I}\right]\right\}\end{aligned} \tag{12}$$

For facilitate the discussion, we define:

$$\mathbf{S}=-\frac{1}{U}\frac{3}{U}\left[1-\frac{3}{2}(\mathbf{Q}:\mathbf{Q})\right]^{-2}\left[\left(1-\frac{1}{3}U\right)\mathbf{Q}-U\left(\mathbf{Q}\cdot\mathbf{Q}-\frac{1}{3}(\mathbf{Q}:\mathbf{Q})\mathbf{I}\right)+U(\mathbf{Q}:\mathbf{Q})\mathbf{Q}\right] \tag{13a}$$

$$\mathbf{L}=\frac{\xi^2}{R^2}\frac{1}{U}\left[1-\frac{3}{2}(\mathbf{Q}:\mathbf{Q})\right]^{-2}\left\{\tilde{\nabla}^2\mathbf{Q}+\frac{\tilde{L}_2}{2}\left[\tilde{\nabla}(\tilde{\nabla}\cdot\mathbf{Q})+[\tilde{\nabla}(\tilde{\nabla}\cdot\mathbf{Q})]^T-\frac{2}{3}\mathrm{tr}[\tilde{\nabla}(\tilde{\nabla}\cdot\mathbf{Q})]\mathbf{I}\right]\right\} \tag{13b}$$

$$\frac{d\mathbf{Q}}{d\tilde{t}}=\mathbf{S}+\mathbf{L} \tag{13c}$$

where $t^*=t\frac{3ckT^*}{\eta}$ is dimensionless time, $U=\frac{3T^*}{T}$ is dimensionless temperature, $\xi=\sqrt{\frac{L_1}{ckT^*}}$ is molecular length scale, $\tilde{L}_2=\frac{L_2}{L_1}$ is dimensionless elastic coefficient, and

R is geometry length scale (i.e. the fiber radius), **S** is the short-range contribution, and **L** is the long-range distribution.

Here we discuss the main effects arising from **S** and **L**. As mentioned above, **S** represents the short-range elastic contribution, which governs the isotropic-nematic phase transition and tends to keep the molecular order (S, P) equal to that of the equilibrium state in a local domain. The second term **L** is the long-range order elastic effect of the molecular field to impose an energetic penalty for any spatial gradients ($\nabla\mathbf{Q} \neq 0$). As mentioned before, the long-range effect is known as the Frank elasticity. The dimensionless parameters of the model are: U, $\mathcal{R} = \frac{R}{\xi}$, and $\tilde{L}_2$. The nematic potential U is a dimensionless temperature that controls the equilibrium order parameter S_{eq} at the phase transition. According to the Doi-Edwards uniaxial nematic theory [12]:

$$S_{eq} = \frac{1}{4} + \frac{3}{4}\sqrt{\left(1 - \frac{8}{3U}\right)}, \quad U = \frac{3T^*}{T} \qquad (14a,b)$$

where T* is an absolute reference temperature just below the isotropic-nematic phase transition temperature like we defined before. For U<8/3 the stable phase is isotropic, for $8/3 \leq U \leq 3$ there is biphasic equilibrium, and for higher values of U the phase is uniaxial nematic. In this work, we have used $2.8 \leq U \leq 6.55$. The parameter $\mathcal{R} = \frac{R}{\xi}$ is the ratio of the fiber radius to the internal length scale (ξ). The internal length scale represents the characteristic size of a defect core and is usually much smaller than the system size R. In this work, we have used $0<\mathcal{R}<150$. When $\mathcal{R}<<1$, long-range energy dominates, spatial gradients are costly and homogeneous states are selected. On the other hand, when $\mathcal{R}>>1$, long-range elasticity is insignificant with respect to short-range elasticity and defects proliferate, since spatially, non-homogeneous states are energetically not costly. The dimensionless scale $\tilde{L}_2 = \frac{L_2}{L_1}$ is a measurement of elastic anisotropy. When $\tilde{L}_2$=0, the system is isotropic and all elastic modes have the same elastic modulus. The thermodynamic restrictions, equation (7b), yield [9]:

$$\tilde{L}_2 > -\frac{3}{5} \tag{15}$$

in addition, since for discotic nematics, it is well-known that $K_{22}>K_{11}$, and $K_{22}>K_{33}$ then

$$-\frac{3}{5} < \tilde{L}_2 \leq 0 \tag{16}$$

In this paper, we have used $\tilde{L}_2 = -0.5$ throughout.

The governing equation (12) is solved in the unit circle ($\tilde{r}$ =1) with the following boundary conditions:

t*>0, $\tilde{r}$ =0.5, **Q=Q$_{eq}$**

$$\mathbf{Q}_{eq} = S_{eq}\left(\boldsymbol{\alpha\alpha} - \frac{1}{3}\mathbf{I}\right) \tag{17}$$

The symbol $\tilde{r}$ is the dimensionless radial distance ($\tilde{r}$ = r/R), and $\tilde{r}$ =0 is the center of the computational domain (i.e. fiber axis). The Dirichlet boundary condition sets the eigenvalues of uniaxial tensor order parameter equal to its equilibrium value ($S=S_{eq}$), and the distinct eigenvector **n** parallel to the azimuthal ($\boldsymbol{\alpha}$) direction of the cylindrical coordinates system ($\tilde{r}$, α). The symbol $\boldsymbol{\alpha}$ represents the unit vector along the azimuthal α direction. The initial conditions are:

$$t^*=0,\ \mathbf{Q}_{ini} = S_{ini}(\mathbf{n}_{ini}\mathbf{n}_{ini} - \frac{1}{3}\mathbf{I}) + \frac{1}{3}P_{ini}(\mathbf{m}_{ini}\mathbf{m}_{ini} - \mathbf{l}_{ini}\mathbf{l}_{ini}) \tag{18}$$

where S_{ini} and P_{ini} are random and $S_{ini} \approx 0$, $P_{ini} \approx 0$, $\mathbf{n}_{ini}$, $\mathbf{m}_{ini}$, and $\mathbf{l}_{ini}$ are corresponding three random eigenvectors. The initial conditions represent an isotropic state (S=0, P=0) with thermal fluctuations in order (S, P) and orientation (**n, m, l**).

4.4 Geometric Analysis for Planar Polar Textures

In this section, we present a geometric analysis of the planar polar texture, with the objective of characterizing the distance d between the two +1/2 disclinations. To find a close form expression for d, we must assume isotropic elasticity, $\tilde{L}_2 = 0$. In addition, we shall assume that the tensor order parameter is uniaxial (i.e. P=0):

$$\mathbf{Q} = S\left(\mathbf{nn} - \frac{1}{3}\mathbf{I}\right) \tag{19}$$

the director **n** orientation in the PP texture is best analyzed using a polar cylindrical coordinate system (r, α). In this system, the spatial dependence of the order parameter is:

$$\mathbf{Q}(r,\alpha) = S(r,\alpha) \cdot \left(\mathbf{n}(r,\alpha)\mathbf{n}(r,\alpha) - \frac{1}{3}\mathbf{I} \right) \tag{20}$$

To satisfy the unit length restriction ($\mathbf{n} \cdot \mathbf{n} = 1$), we parameterize the director as follows:

$$\begin{cases} n_r = \cos\theta(r,\alpha) \\ n_\alpha = \sin\theta(r,\alpha) \end{cases} \tag{21}$$

assuming that outside the defect cores, the scalar order parameter is constant and equal to its equilibrium value, $S=S_{eq}$ (see equation (14)). Assuming steady state, the governing equation (12) then reduces to

$$\nabla^2\theta = 0 \tag{22}$$

A general singular defect solution of the Laplace equation to the director angle θ is:

$$\theta = s\alpha + c \tag{23}$$

where c is an arbitrary constant and *s* is the strength of the defect. Since the director orientation angle θ is governed by the linear Laplace operator (∇^2), the principle of superposition can be used to describe textures with two or more defects. The general solution in the presence of arbitrary number n of defects of strength s_i, at a point P, is:

$$\theta = \sum_{i=1}^{n} s_i \alpha_i + c \tag{24}$$

where α_i is the polar angle of the ray originating at the defect of strength s_i and ending at point P, c is a constant and θ is the director angle at point P. For the planar polar texture with 2 defects of strength s=+1/2, the director field is:

$$\theta = \frac{1}{2}(\alpha_1 + \alpha_2) + c \tag{25}$$

Next we use the generally valid equation (24) to analyze the planar polar texture for a fiber of radius R. Figure 4.4a shows the schematic of the fiber cross-section, and the coordinate system. The dots denoted I, II are the two-disclination lines parallel to the fiber texture axis. The x-axis is defined by α=0 in our polar coordinates. The geometric analysis consists of finding the dimensionless distance d* between two defects. According to Figure 4.3b, the director angle at the fiber surface is tangential. Thus at any arbitrary point P on the surface, the director angle θ measured with respect to the x-axis is

$$\theta = \frac{\pi}{2} + \alpha \tag{26}$$

Since equation (25) describes the director angle for a two defects texture without constraints, the effect of fixed boundary conditions given by equation (17) needs to be incorporated. Multiple defects solution in the presence of boundary constraints is best obtained using the method of images in which a surface orientation constraint is captured by an image defect. The method of images is widely used to obtain analytical defect solutions in liquid crystalline materials, and full details can be found in the literature [4]. Figure 4.4a shows the two image defects, denoted III and IV, for this particular problem. The strength s of the two image defects is again +1/2. Using equation (24) to take into account the contribution from the two defects, we find that the director orientation at an arbitrary point P lying on the fiber surface is

$$\theta_P = \frac{\pi}{2} + \alpha = s\left(\frac{\pi}{2}\right) + s(\beta) + s(\gamma) + s\left(\frac{\pi}{2} + \alpha\right) + c \tag{27}$$

where α, β, γ are clearly defined in figure 4.4a, and where c is an arbitrary constant. Figure 4.4b shows how the defect and image distances are related to the fiber axis. The two defects (I, II) are located at a distance x from the fiber axis and the two images (III, IV) are located at a distance ℓ for each defect. It turns out that to find x and define the geometry of the PP texture, ℓ must also be known. In our case, s=+1/2, c=0, and equation (27) then becomes:

$$\alpha = \gamma + \beta \tag{28}$$

According to equation (28), the relation between the angular coordinates is:

$$\tan\alpha = \tan(\gamma + \beta) = \frac{\tan\gamma + \tan\beta}{1 - \tan\gamma \cdot \tan\beta} \tag{29}$$

Using equation (29) in conjunction with the following trigonometric relations:

$$\begin{cases} \tan\gamma = \dfrac{R\sin\alpha}{1+x} \\ \tan\alpha = \dfrac{R\sin\alpha}{x} \\ \tan\beta = \dfrac{R\sin\alpha}{2x} \\ \sin^2\alpha + \cos^2\alpha = 1 \\ \cos\alpha = \dfrac{x}{R} \end{cases} \tag{30}$$

we finally get:

$$R^2 = x \cdot \ell \tag{31}$$

which relates the fiber radius R to the defect distance x, and image position ℓ. Since ℓ is unknown, another equation is needed. The additional equation needed to find $\ell(x)$ is the defect-defect force balance equation. To find the force of interaction between two defects of strength s_1 and s_2, the total energy W_{12} is found [4] by integrating the long-range energy f_ℓ (equation (6b)) and using equation (25) to obtain [4]:

$$W_{12} = -2\pi K s_1 s_2 \ln \frac{r_{12}}{r_c} \tag{32}$$

where r_{12} is the distance between defects and r_c is a lower cut-off distance. Then the force $\mathcal{F}_{12}$ between two defects is [4]:

$$\mathcal{F}_{12} = -2\pi k \frac{s_1 s_2}{r_{12}} \tag{33}$$

which shows that the force $\mathcal{F}_{12}$ is inversely proportional to their separation distance r_{12}. Employing the fomulation used to find equation (33), the force balance on defect I is:

$$\frac{1}{\ell - x} = \frac{1}{2x} + \frac{1}{\ell + x} \tag{34}$$

Coupling the equation (31) and equation (34) we finally get:

$$x = \frac{1}{\sqrt[4]{5}} R \tag{35}$$

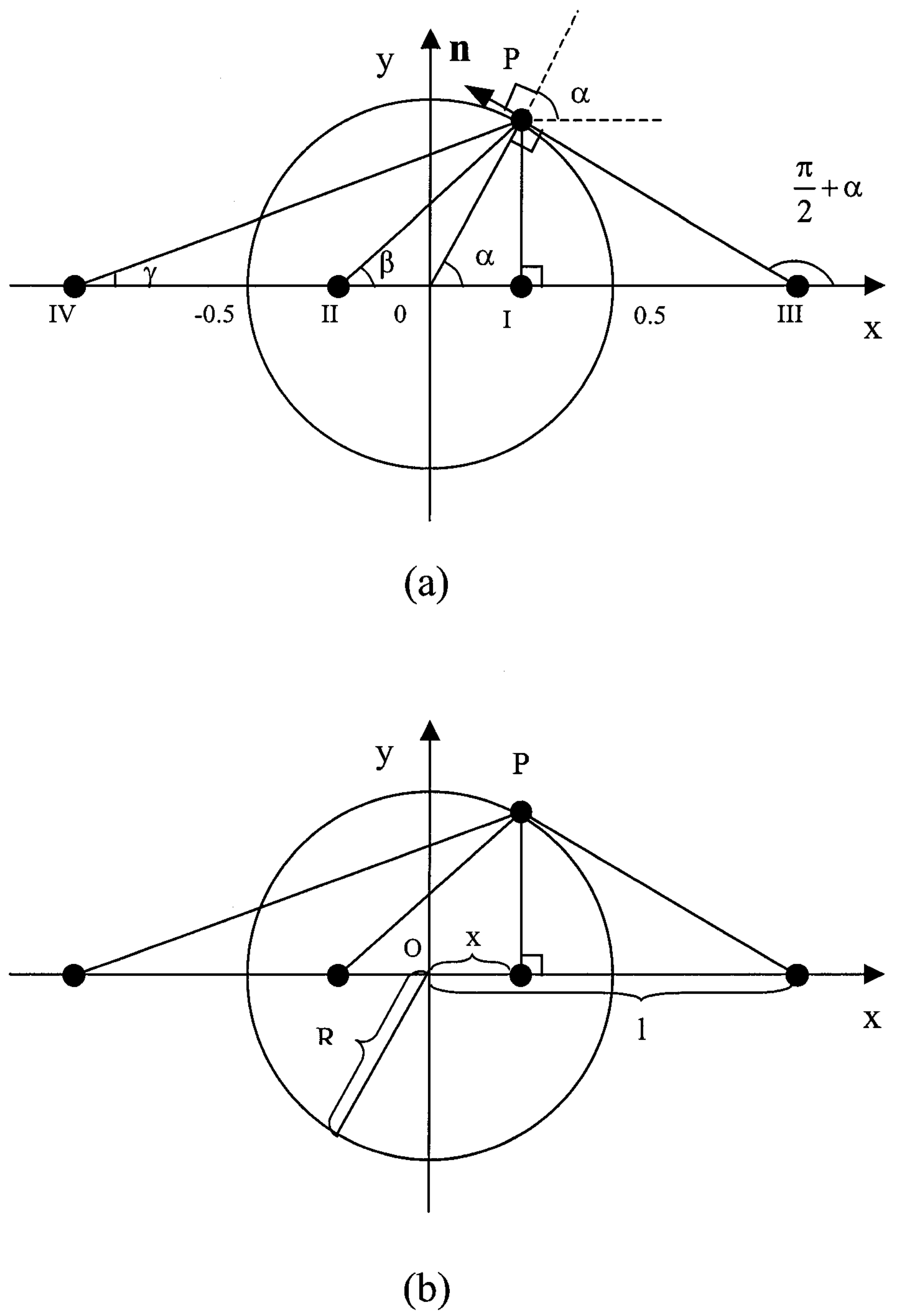

Figure 4.4: Schematic of fiber geometry. (a) The dots I and II are two defects of strength s=+1/2 in the computational domain and III and IV are two image defects of strength s=+1/2. P is an arbitrary point on the surface, on which the director **n** is tangential to the surface. (b) The distance between defect and coordinate origin is x, the distance between image and coordinate origin is ℓ, and the fiber radius is R.

which means that when the system reaches steady state, the two defects only lie on a circle of radius $\frac{1}{\sqrt[4]{5}}R$. Equation (35) is one of the main results of this paper. In the absence of elastic anisotropy (L_2=0), the distance between two defects is fixed by the fiber radius. The number $1/\sqrt[4]{5}$ arises due to the fiber geometry. In the rectangular geometry this factor is 0.5, but in the circular domain it is 0.66. Generalization of this analysis to other fiber geometries of industrial relevance, such as elliptical, is possible. Next we shall establish the accuracy and relevance of the theoretical results by comparing numerical solutions of the full non-linear system of parabolic partial deferential equations (12) with the theoretical prediction given in equation (35).

4.5 Modeling fiber texture behaviour

4.5.1 Computational Modeling

The model equation (12) is a set of six coupled non-linear parabolic partial differential equations, solved in the unit circle, subjected the auxiliary conditions (see equation (17) and (18)). The equations are solved using Galerkin Finite Elements with lagrangean linear basis functions for spatial discretization and a fifth order Runge-Kutta-Cash-Karp time adaptive method. Convergence and mesh-independence were established in all cases using standard methods. Spatial discretization was judiciously selected taking into account the length scale of our model. As mentioned above, the Landau-de Gennes model for nematic liquid crystals has an external length scale L_e and an internal length scale L_i as follows:

$$L_e=R,\ L_i=\xi=\sqrt{\frac{L_1}{ckT^*}} \qquad \text{(36a,b)}$$

where R is the fiber radius, and where in the length scale obeys $L_e \gg L_i$. If defects are present, the mesh size has to be commensurate with L_i. It should be noted that the external length scale governs the directors' orientation (**n, m, l**) while the internal length scale governs the scalar order parameter (S, P). In addition, care should be taken to select an appropriate time integration technique to overcome the intrinsic stiffness of the system. The model equations contain an internal time scale τ_i and an external time scale τ_e. The internal time scale governs the evolution of the scalar order parameters (S, P) and is given by

$$\tau_i = \frac{\eta}{ckT^*} \tag{37}$$

A much longer external time scale τ_e controls the evolution of the directors and is given by:

$$\tau_e = \frac{\eta L_e^2}{L_1} \tag{38}$$

The selected adaptive time integration scheme is able to efficiently take into account the stiffness that rises due to the disparity between time scale: $\tau_i << \tau_e$.

4.5.2 Results and Discussions

To efficiently visualize the solution vector **Q**, we represent **Q** by a cuboid whose axes are the directors (**n, m, l**) and whose sides are proportional to its eigenvalues. Since **Q** has negative eigenvalues, we visualize $\mathbf{M} = \mathbf{Q} + \frac{1}{3}\mathbf{I}$ instead of **Q**.

Figure 4.5a shows the computed texture phase diagram, given in terms of nematic potential $\frac{1}{U} = \frac{T}{3T^*}$ as a function of dimensionless fiber radius $\mathcal{R}$ = R/ξ for the auxiliary conditions (17, 18), and $2.8 \leq U \leq 6.55$, $0<\mathcal{R}<150$. The phase diagram identifies the stability of the textures as a function of temperature and fiber radius. Ultra thin fiber favor the PR texture while lower temperature and thicker fiber favors the stability of the PP texture. The full curved line indicates the PP and PR transition line. The area between the full curved and dashed line show bistability. This is due to the lack of numerical resolution beyond our available computational power. In this area either the PR and PP textures were obtained. The dot near the bottom of the diagram represents the parametric conditions used in obtaining Fig.4.5b. For U>8/3, the fiber is isotropic. The phase diagram shows the processing (temperature) and geometry (fiber radius) affect the texture selection process. Figure 4.5b is a representative typical steady state solution of the planar polar texture for U=6.55, $\mathcal{R}$=67, $\tilde{L}_2$=-0.5. It clearly shows the characteristic planar polar texture, with the two s=+1/2 defects collinear with the fiber axis. The orientation of the defect-defect axis is arbitrary since the system evolves from an isotropic state that contains no texture information. The simulations show the bending distortions close to the two defects and an aligned region between the two defects. Figure 4.5c-d shows a gray-scale plot and a surface plot of the uniaxial scalar order parameter S as a function of dimensionless distance (x*, y*). In the gray-scale plot a low order parameter ($S \approx 0$) is black and high order parameter ($S \approx 1$) is white. The dark dots in the figure correspond to the two s=+1/2 defects. The narrow peaks in the surface plots indicate the difference in scale between defect cores and fiber radius. At the defects core $S \approx 0$, as expected. Figures 4.5e-f show the corresponding gray-scale and surface plots of the biaxial order parameters P as a function of dimensionless distance (x*, y*). In the gray-scale plot, $P \approx 0$ corresponds to black and $P \approx 1$ to white. The figure clearly shows the biaxial eigenvalue of **Q** at the two defect cores. The corresponding surface plot shows that at the defects core $P \approx 0.4$ and strong biaxiality is present. The reason why s=+1/2 defects shows biaxial ordering is because this class of defect ($|s| = \frac{1}{2}$) lacks cylindrical symmetry and hence P must be non-zero.

Figure 4.6a-d show computed visualization of the evolution of the tensor order parameters **Q** for the same parametric conditions as in Fig. 4.5, for the following dimensionless times: (a) 200, (b) 400, (c) 800, (d) steady state. The figure shows that at early time the texture is close to the PR texture with the two defects close to the fiber axis, and as time proceeds the defects move away from each other and towards the fiber surface. The reason for the increase in the defect-defect distance is the mutual and equal repulsive force between two defects of equal sign and strength, which in this case is +1/2. The defects drift apart and eventually slow down and settle at a distance x from the fiber axis, because the repulsive image forces arising from the fixed boundary conditions (equation (17)). Figure 4.6e shows the corresponding total dimensionless long-range energy f_ℓ^* as a function of dimensionless time t^*. The total dimensionless long-range energy f_ℓ^* is obtained by:

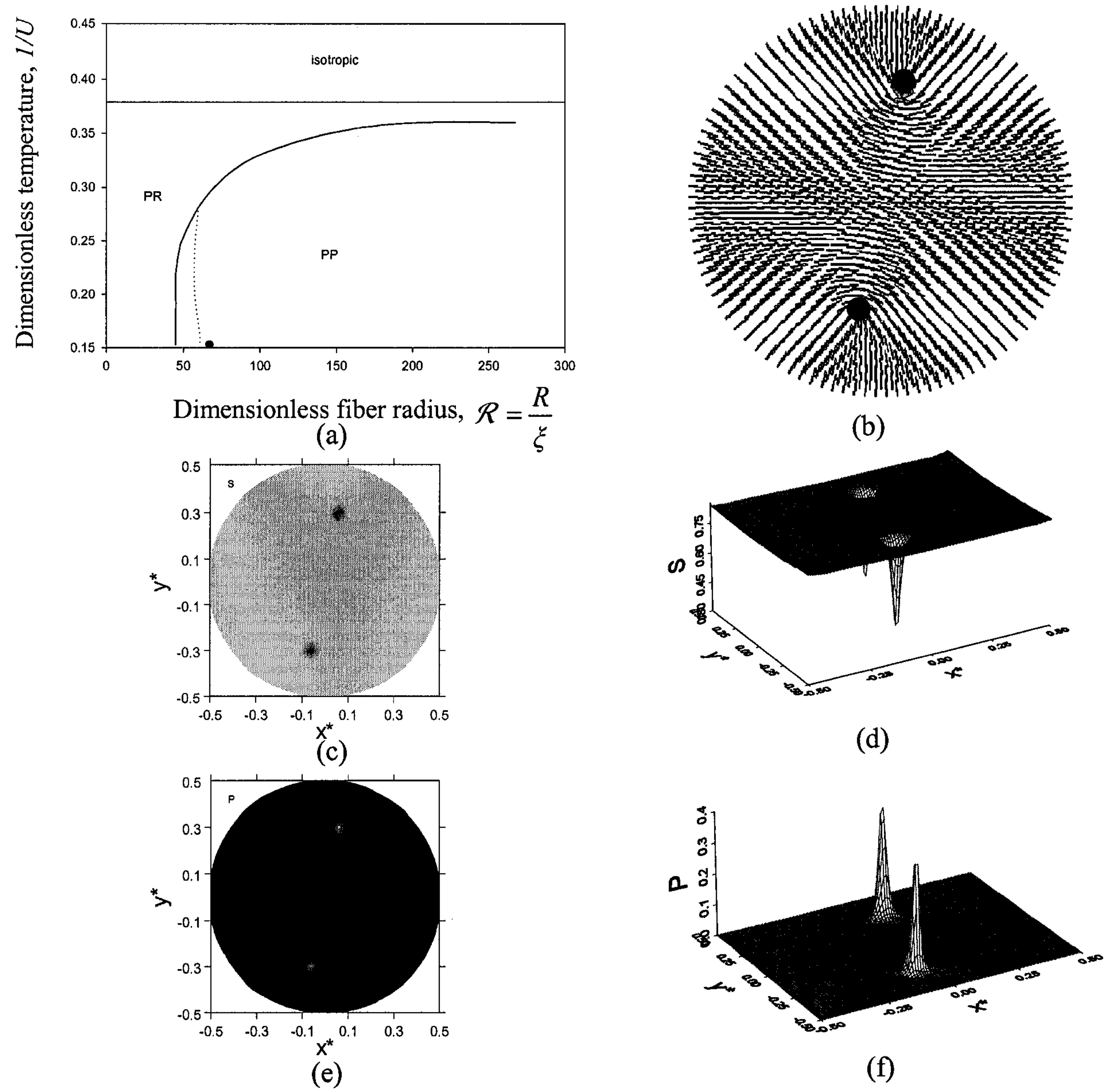

Figure 4.5: (a) Computed texture phase diagram, given in terms of nematic potential $1/U = T/3T^*$ as a function of dimensionless fiber radius $\mathcal{R} = R/\xi$ for the auxiliary conditions (equation (17) and (18), $2.8 \le U \le 6.55$, $0<\mathcal{R}<150$). Fig. 4.5(b) Steady state solution of the planar polar texture for U=6.55, $\mathcal{R}$=67, $\tilde{L}_2$=-0.5. Fig. 4.5(c)-(d) Gray-scale plot and surface plot of the uniaxial scalar order parameter S as a function of dimensionless distance (x*, y*). In the gray-scale plot a low order parameter ($S \approx 0$) is black and high order parameter ($S \approx 1$) is white. The dark dots in the figure correspond to the two s=+1/2 defects. The narrow peaks in the surface plots indicate the difference in scale between defect cores and fiber radius. At the defects core $S \approx 0$, as expected. Fig. 4.5(e)-(f) Gray-scale and surface plots of the biaxial order parameters P as a function of dimensionless distance (x*, y*). In the gray-scale plot, $P \approx 0$ corresponds to black and $P \approx 1$ to white. The figure clearly shows the biaxial eigenvalue of **Q** at the two defect cores. The corresponding surface plot shows that at the defects core $P \approx 0.4$ and strong biaxiality is present.

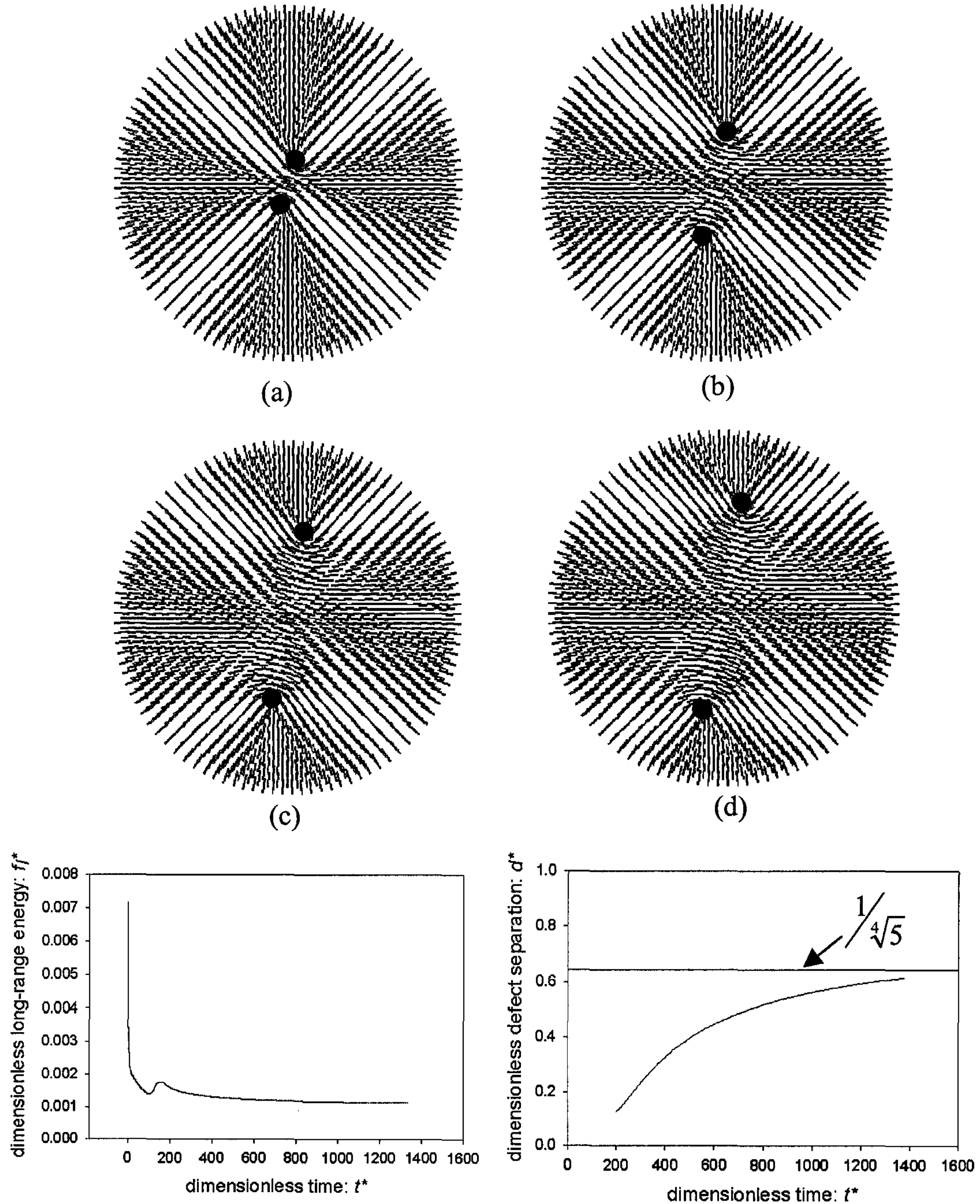
(a)
(b)
(c)
(d)
(e)
(f)

Figure 4.6: (a)-(d) Computed visualization of the evolution of the tensor order parameters Q for the same parametric conditions as in Fig. 4.5. Fig. 4.6e Total dimensionless long-range energy f_ℓ^* as a function of dimensionless time t*. the long-range energy decreases non-monotonically with time. The increase in f_ℓ^* at t*=180 indicates the following topological transformation: $s_1 \rightarrow 2s_2$. Fig. 4.6f Dimensionless defect separation distance d* as a function of dimensionless time t*. The horizontal line corresponds to the theoretical results derived in the previous section: $d^* = x/R = 1/\sqrt[4]{5}$ .Parametric conditions: U=6.55, $\mathcal{R}$=67, $\tilde{L}_2$=-0.5.

$$f_{\ell}^{*} = \frac{\xi^{2}}{2R^{2}} \iint_{A} \left\{ \tilde{\nabla}\mathbf{Q} \vdots (\nabla \mathbf{Q})^{T} + \tilde{L}_{2} \left(\tilde{\nabla} \cdot \mathbf{Q} \right) \cdot \left(\tilde{\nabla} \cdot \mathbf{Q} \right) \right\} \cdot dA \tag{39}$$

where *A* is the computational domain, and the dimensionless time is given by:

$$t^{*} = t \frac{3ckT^{*}}{\eta} \tag{40}$$

Figure 4.6e shows that the long-range energy decreases non-monotonically with time. The increase in f_{ℓ}^{*} at t*=180 indicates the following topological transformation:

$$s_1 \rightarrow 2s_2 \tag{41}$$

where s_1=+1 and s_2=+1/2. The driving force for this transformation is the reduction of the long-range elastic energy. The long-range elastic energy associated with a defect scales with the square of its strength and since $(s_1)^2 > 2(s_2)^2$, the emergence of two s=+1/2 defects lowers the energy. The local maximum in f_{ℓ}^{*} indicates the global dimensionless time t* at which the defect transformation (equation (41)) occurs. Figure 4.6f shows the corresponding dimensionless defect separation distance d* as a function of dimensionless time t*. The horizontal line corresponds to the theoretical results derived in the previous section: $d^{*} = \frac{x}{R} = \frac{1}{\sqrt[4]{5}}$ (see equation(35)). The figure clearly shows that as t* increases, the defect-defect separation distance increases and eventually asymptotes to the predicted value of $1/\sqrt[4]{5}$. Figure 4.7 shows the uniaxial scalar order parameter S (left) and biaxial order parameter P (right) as a function of dimensionless distance d*, for seven dimensionless times, t*: 100-1350, and the same parametric conditions as in Fig 4.5. The figure shows the details of the s=+1 defect nucleation and the $s_1 = +1 \rightarrow 2s_2 = +1/2$ defect splitting process. The early stage (100<t*<133) shows the continuous front propagation of S that leads to the nucleation of the s=+1 defect. At t*=133, a wide core s=+1 displaying weak biaxially starts to decay by core splitting. The core splitting process is clearly seen in the t*=178 frame. The defect core has spitted into two strongly biaxial localized peaks. As the time elapses, the two peaks corresponding to the +1/2 defects drift away from the fiber axis (d*=0) and towards the bounding surface.

Figure 4.8 shows the dimensionless defect separation distance d* as a function of dimensionless temperature $\frac{T}{3T^*}$, for $\mathcal{R}$=67. The solid line corresponds to the theoretical results, $d^*=1/\sqrt[4]{5}$. The results confirm the validity of the theoretical analysis.

Figure 4.9 shows the dimensionless defect separation distance d* as a function of dimensionless fiber radius $\mathcal{R}=\frac{R}{\xi}$, for U=3.55. The numerical results again confirm the validity of the theoretical results. It should be mentioned that derivation from the theoretical result are likely to originate from computational limitations that arise due to the inherent disparate length scales in the model. Also for the presented results and parametric conditions, anisotropic Frank elasticity has no effect on x. Nevertheless we expect that for higher U, the magnitude of $\tilde{L}_2$ will affect the ideal value of $x=1/\sqrt[4]{5}\,R$.

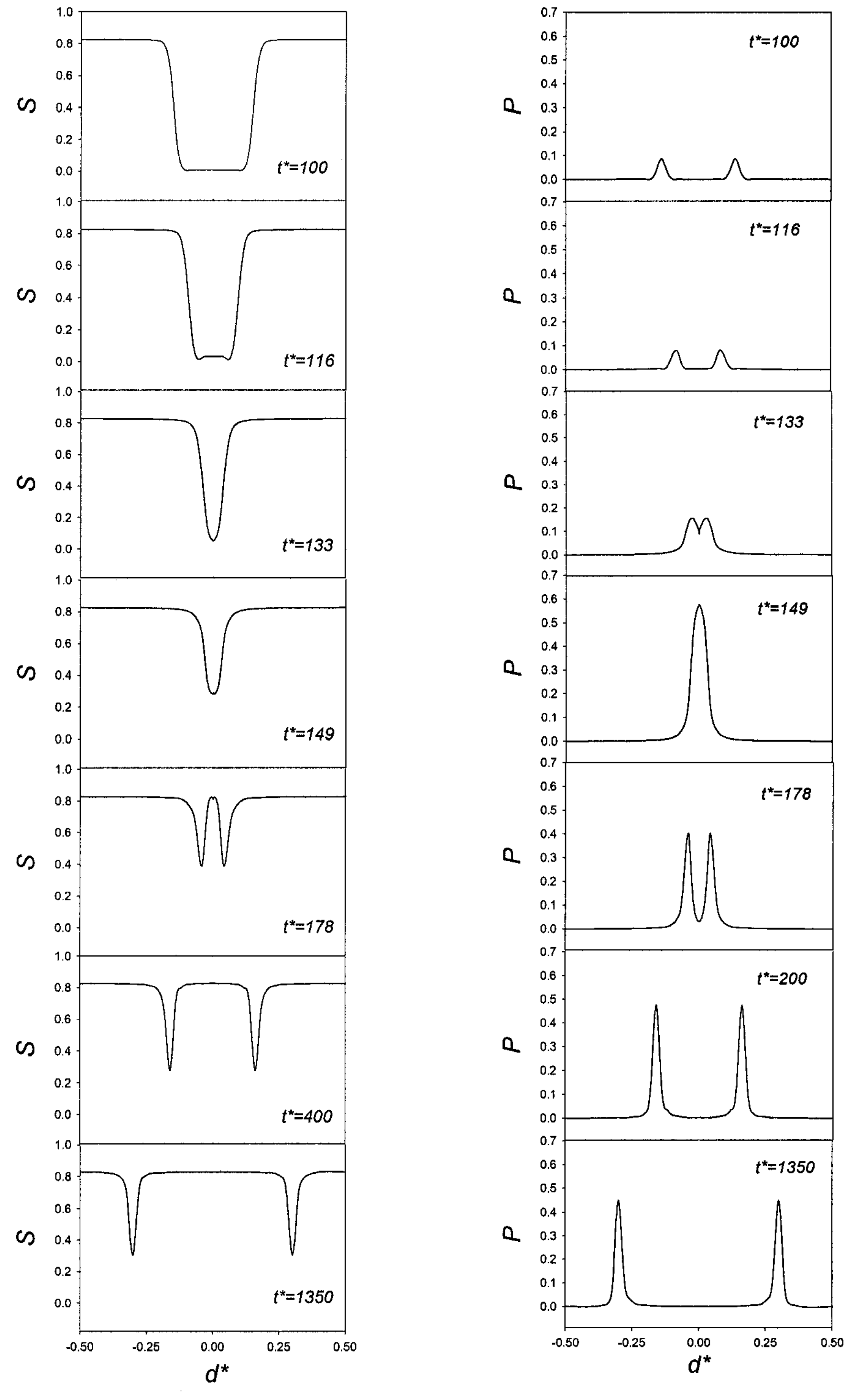

Figure 4.7: Uniaxial scalar order parameter S (left) and biaxial order parameter P (right) as a function of dimensionless distance d*, for seven dimensionless time, t*: 100-1350. Parametric conditions: U=6.55, $\mathcal{R}$=67, $\tilde{L}_2$=-0.5. The figures clearly capture the $s_1 \rightarrow 2s_2$ defect transformation.

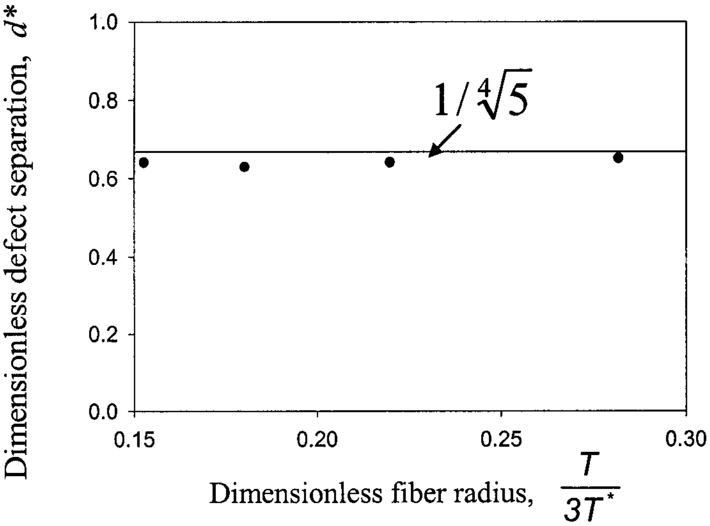

Figure 4.8: The dimensionless defect separation distance d* as a function of dimensionless temperature $\frac{T}{3T^*}$, for $\mathcal{R}$=67. The solid line corresponds to the theoretical results, d*=$1/\sqrt[4]{5}$.

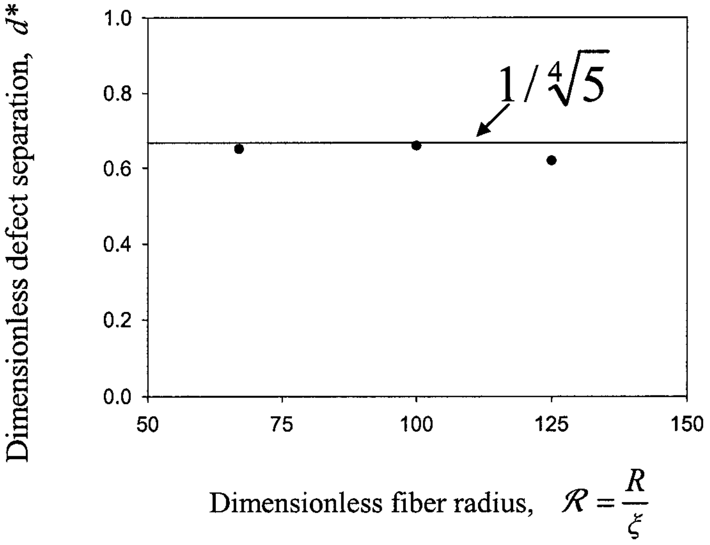

Figure 4.9: Dimensionless defect separation distance d* as a function of dimensionless fiber radius $\mathcal{R}=\frac{R}{\xi}$, for U=3.55. The solid line corresponds to the theoretical results, d*=$1/\sqrt[4]{5}$.

Conclusion

A model to describe texture formation in mesophase carbon fibers has been developed, implemented, and shown to replicate commonly observed cross-sectional carbon fiber textures of industrial relevance. The model is based on the classical Landau-de Gennes theory for liquid crystals and has been adapted to describe discotic mesophases. The model is able to predict the formation of planar radial and planar polar textures. The parametric envelope of their stability in terms of temperature and fiber radius has been computed. Lower temperature and thicker fiber tend to select the planar polar texture and higher temperature and thin fiber tend to promote the emergence of the planar radial texture. The geometric analysis of the planar polar texture has been performed and the defect separation distance is shown to be equal to $1/\sqrt[4]{5}$. Computational modeling of texture formation shows that the two defects in the planar polar texture arise from a topological transformation that involves the decay of a +1 defect into two +1/2 defects. The numerical results show that the computed defect separation distance equals to the theoretical results for different fiber radius and temperatures. The new results presented in this paper contribute towards a better understanding of the principles that control cross-section texture selection during the melt spinning of mesophase carbon.

Acknowledgement

This grant is supported by a grant from the Donors of The Petroleum Research Fund (PRF) administered by the American Chemical Society.

Bibliography:

[1] McHugh J. J., 1994, *PHD Thesis*, Clemson University.

[2] Hurt R. H. and Chen Z. Y., 2000, *Physics Today*, **March,** 39.

[3] Peebles L. H. Jr., 1995, *Carbon Fibers-Formation, Structure, and Properties* (Boca Raton, FL: CRC).

[4] de Gennes P. G. and Prost J., 1993, The *Physics of Liquid Crystal* 2nd edn (Oxford: Clarendon).

[5] Sokalski K. and Ruijgrok T. W., 1982, *Physica*, **113A,** 126.

[6] Wang L. and Rey A. D., 1997, *Modeling Simul. Mater. Sci. Eng.*, **5,** 67.

[7] Sonnet A., Kilian A. and Hess S., 1995, *Physical Review E*, **52,** 52.

[8] Tsuji T. and Rey A. D., 1997, *J. Non-Newtonian Fluid Mech.*, **73,** 127.

[9] Longa L., Monselesan D. and Trebin H. R., 1987, *Liquid Crystals*, **2**(6), 769.

[10] Singh A. P., 2000, *PHD Thesis*, Mcgill University.

[11] Beris A. N. and Edwards B. J., 1994, *Thermodynamics of flowing systems*, (Oxford: Claredon).

[12] Doi M. and Edwards B. J., 1986, *The Theory of Polymer Dynamics*, (Oxford: Clarendon).

Chapter 5

Modeling Elastic and Viscous Effects on the Texture Structure of Ribbon Shaped Carbonaceous Mesophase Fibers

5.1 Abstract

Carbonaceous mesophases are discotic nematic liquid crystals that are spun into high performance carbon fibers using the melt spinning process. The spinning process produces a wide range of different fiber textures and cross-sectional shapes. Circular planar polar (PP), circular planar radial (PR) textures, ribbon planar radial (RPR), and ribbon planar line (RPL) textures are ubiquitous ones. This paper presents, solves, and validates a model of mesophase fiber texture formation based on the classical Landau-de Gennes theory of liquid crystals, adapted here to carbonaceous mesophases. The effects of fiber cross-sectional shape and elongational flow on texture formation are characterized. Emphasis is on qualitative model validation using existing experimental data [1]. The role of elasticity and flow-induced orientation on texture selection mechanism on ribbon-shaped mesophase fibers is characterized. The model is able to predict the formation of the commonly observed line texture, and the fine structure of the line is reproduced and explained in terms of classical liquid crystal defect physics. The results provide additional knowledge on how to optimize and control mesophase fiber textures.

5.2 Introduction

Carbonaceous mesophases, such as coal tar and petroleum pitches, are used in the industrial manufacturing of high performance carbon fibers. This relatively new carbon fiber is more competitive than the conventional one made from the acrylic precursors in several application areas [2]. The thermodynamic phase that describes carbonaceous mesophases is the discotic nematic liquid crystal (DNLC) state [3]. Liquid crystals are intermediate (i.e. mesophase) phases, typically found for anisodiametric organic molecules, which exist between the higher temperature isotropic liquid state and the lower temperature crystalline state. Carbonaceous mesophases are composed of disk-like molecules. Figure 5.1 shows the molecular geometry, positional disorder, and uniaxial orientational order of discotic nematic liquid crystals. The partial orientational order of the molecular unit normal **u** is along the average orientation or director **n** (**n**·**n**=1). The name discotic distinguishes the molecular geometry and the name nematic identifies the type of liquid crystalline orientational order.

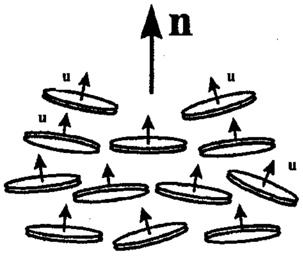

Figure 5.1: Definition of director orientation of a uniaxial discotic nematic liquid crystalline material. The director **n** is the average orientation of the unit normals to the disk-like molecules in a discotic nematic phase.

The industrial fabrication of mesophase carbon fiber using the conventional melt spinning process typically produces micrometer-sized cylindrical and ribbon filaments whose cross sectional area displays a variety of transverse textures [4], that is, different spatial arrangements of the average orientation **n** on the plane perpendicular to the fiber axis. The selection mechanisms that drive the texture formation pattern are at present not well understood, but due to the strong structure-properties correlations, they are essential for product optimization [2,4].

A question of fundamental importance to the melt spinning of carbonaceous mesophases is to determine how elastic and viscous mechanisms affects the fiber process-induced structuring and cross-sectional fiber textures' selection. When considering elastic mechanisms, it is necessary to identify the three fundamental elastic modes of these materials. Figure 5.2 shows the three types of elastic deformations, known as splay, twist, and bend, and the corresponding modulus K_{11}, K_{22}, and K_{33}, known as Frank elasticity constants [5]. The bulk elastic free energy density is given by:

$$f_n = \frac{1}{2}K_{11}(\nabla \cdot \mathbf{n})^2 + \frac{1}{2}K_{22}(\mathbf{n} \cdot \nabla \times \mathbf{n})^2 + \frac{1}{2}K_{33}\left|\mathbf{n} \times (\nabla \times \mathbf{n})\right|^2 \tag{1}$$

Thermodynamic stability requires:

$$K_{11} > 0; K_{22} > 0; K_{33} > 0 \tag{2}$$

In contrast to rod-like nematics, for disc-like nematics the bending disc's trajectories give rise to a splay deformation, and the splaying disc's trajectories give rise to a bend deformation; by disc trajectory it means the curve locally orthogonal to the director. For DNLCs the following inequalities hold [7]:

$$K_{22} > K_{11}; \quad K_{22} > K_{33} \tag{3a,b}$$

which indicates that planar director deformations are favored.

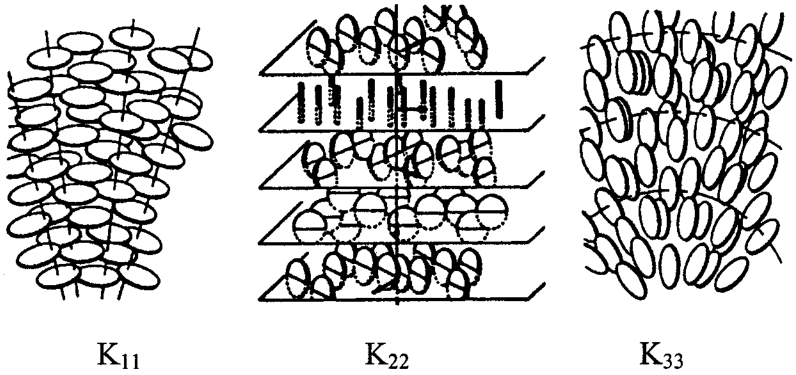

Figure 5.2: Schematics of the elastic splay (left), twist (center), and bend (right) deformation for uniaxial discotic nematics. Note that the splay (bend) mode involves bending (splaying) of the disk's trajectories, in contrast to the case of uniaxial rod-like nematics. A disk trajectory is a curve locally orthogonal to the director. Adapted from [6].

In addition to elastic effects, viscous mechanisms also affect texture formation and structure. When taken into account flow-induced orientation in complex processing flows, the orienting effects of shear and extensional flow have to be taken into account. The theoretical rheology of discotic nematic liquid crystals has been widely studied in the past [8-11]. Flow-aligning discotic nematic liquid crystals subjected to simple shear flow orient the director within the shear plane and close to the velocity gradient direction. Furthermore, the effect of uniaxial elongation flow is to align the director along the compression plane. These simple rules are sufficient to qualitatively predict flow-induced orientation. In processing flows, such as Jeffrey-Hamel flows [8], both shear and deformation are present, and prediction of flow-induced orientation is possible if one type of deformation, say extension, dominates over the others. In general, elongation flows are strongly orienting flows as compared to shear [12]. The validity of this dominant deformation type approach was demonstrated in the analysis of radial outflow of nematic liquid crystals [13], and will be used here to analyze flow-induced orientation in ribbon-shape fibers.

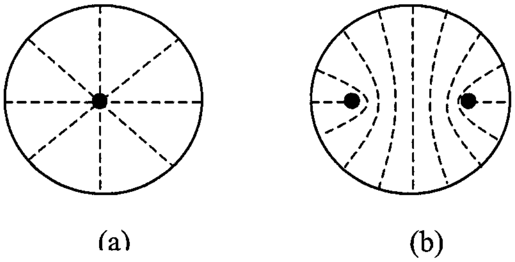
(a) (b)

Figure 5.3: Schematics of two circular cross-sectional textures most commonly seen in mesophase carbon fibers. The dashed line indicates the trajectories of the molecular planes, (a) shows the planar radial (PR) texture, in which only the pure bend mode exists with one defect in the center of strength S=+1, and (b) shows the planar polar (PP) texture, with splay and bend, and two defects of the strength S=+1/2. The corresponding director fields of the PP and PR textures are given by lines perpendicular to the average molecular trajectories. The defects arise due to the constraints of tangential boundary conditions and a planar 2D orientation field.

It is known [4] that the observed circular cross-section fiber textures belong to a numbers of families, such as onion, radial, mixed, PAN-AM, to name a few. Large-scale computer simulations of the radial and PAN-AM textures have been recently performed [14]. Figure 5.3 shows the schematics of two cross-sectional textures most commonly seen in mesophase carbon fibers. The dashed line indicates the trajectories of the molecular planes, (a) shows the planar radial (PR) texture, in which only the pure bend mode exists with one disclination line (singular defects) in the center of strength s=+1, and (b) shows the planar polar (PP) texture, in which two modes of deformation, splay and bend, exist with two disclination lines of the strength s=+1/2. The disclination lines arise due to the constraints of tangential boundary conditions and a planar 2D orientation field. Disclination lines are singularities in the director field and are characterized by strength (1/2, 1, ...) and sign (±) [15]. The strength of a disclination determines the amount of orientation distortion and the sign corresponds to the sense (i.e. clockwise or anti-clockwise) of orientation rotation while circling the defects. Since the energy of a defect scales with the square of the defect strength [16, 17], the planar polar texture would seem to emerge, so as to minimize the elastic energy associated with orientation distortions. In addition, defects of equal sign repel each other, while defects of different sign attract. In the PP texture, defect-defect interaction plays a critical role in the geometry of the texture [18].

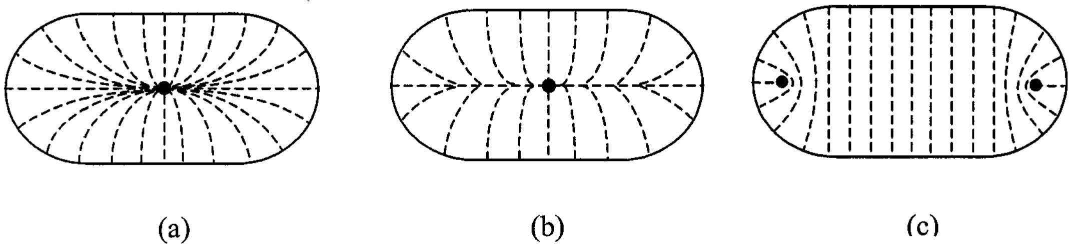

Figure 5.4: Schematics of three ribbon cross-sectional textures most commonly seen in mesophase carbon fibers. The dashed line indicates the trajectories of the molecular planes, (a) shows the ribbon planar radial (RPR) texture, in which splay-bend mode exists with one defect in the center of strength S=+1, (c) shows the ribbon planar line (RPL) texture, with a splay-bend inversion wall, and a defect of strength S=+1, and (c) the ribbon planar polar (RPP) texture with an aligned center region and two defects of strength s=+1/2. The corresponding director fields' of the textures are given by lines perpendicular to the average molecular trajectories.

The structure and formation of non-circular ribbon-shaped mesophase fibers have been characterized experimentally [1], but some features of the process remain poorly understood. Two characteristic cross-section textures of ribbon-shaped fibers are shown in Fig. 5.4. Figure 4a shows a ribbon planar radial (RPR) texture, with a defect of strength s=+1 at the center, which belongs to the same family as the PR texture. In fact a continuous distortion of the PR texture from a circular cross-section into a ribbon cross-section will be shown below to lead to the observed RPR tetxure. The right figure 4b shows the texture of the characteristic planar line (PL) texture, displaying two inversion walls at the center plane and a disclination line of strength s=+1 at the center. Inversion walls are non-singular two-dimensional defects, in which localized director gradients occur. For planar orientation (**n**=(n_x, n_y, 0)) there is no twist distortion and the inversion walls are known as splay-bend walls [19]. Moving across a vertical path off the center, the director rotates by + π radians on the left sector, and by – π radians on the right sector. The continuous rotation is localized in a thin region that defines the inversion wall. At the center, a defect is present to resolve the opposite sense of rotations between the left and right sectors. It should be mentioned that inversion walls can only end at bounding surfaces and other defects, or form closed loops. In the RPL texture each inversion wall ends at the bounding surfaces and starts at the s=+1 disclination line. Usually inversion walls arise in liquid crystals under orienting fields. The appearance and structure of the inversion walls in the RPL texture is virtually identical to those observed by Thomas and co-workers [20] during magnetic re-orientation of nematic liquid crystal polymers. Since the orienting effects of elongational flow and magnetic field are identical [19], the presence of inversion walls in ribbon-shaped mesophase fibers subjected to elongation flows in the converging section of the die and in the spin line is expected. Below we use a simple model that captures inversion-wall formation under extensional flow, and show that subjecting the RPR texture to a strong elongation flow produces the RPL texture. Finally, Fig. 5.4c shows the ribbon planar polar texture (RPP), which is predicted to exist [21], since it belongs to the same family as the PP texture present in circular fibers. This fiber is characterized by an oriented center-region, with two s=+1/2 defects close to the circular edges.

Theory and simulation of liquid crystalline materials continues to be performed using macroscopic, mesoscopic, and molecular models [16]. Macroscopic models based on the Leslie-Ericksen director equations are unsuitable to simulate texture formation because disclinations are singularities in the orientation field. On the other hand, mesoscopic models based on the second moment of the orientation distribution function is well suited to capture the formation of liquid crystalline textures, because disclinations are non-singular solutions to the governing equations. A very well established mesoscopic model in liquid crystalline materials is based on the Landau-de Gennes free energy [16, 22, 23] and is used in this work.

This paper is a continuation of our on-going work on theory and simulation of texture formation in mesophase fibers [14, 24, 25]. The objectives of this paper are:

(1) To simulate the transient formation of the RPR and RPL textures which are commonly observed during the melt spinning of carbonaceous mesophases with ribbon-shaped cross-sections, as well as the expected RPP texture.

(2) To find the mechanisms of RPR and PL texture selection.

This paper is organized as follows. Section 2 presents the theory, the Landau-de Gennes governing equations, and defines the length and time scales of the model. Section 3 flow-induced orientations. Section 4 presents the numerical solutions of our model, and also, discusses the characteristics of the textures. Finally conclusions are presented.

5.3 Theory and Governing Equations

In this section, we present the Landau-de Gennes theory for nematic liquid crystals, and the parametric equations used to describe mesophase fiber texture formation. As mentioned above, the theory is well suited to simulate texture formation since defects are non-singular solutions to the governing equations.

5.3.1 Definition of Orientation and Alignment

The microstructure of DNLCs is characterized by a second order symmetric and traceless tensor, known generally as tensor order parameter **Q** [26]:

$$\mathbf{Q} = \mathrm{S}(\mathbf{nn} - \frac{1}{3}\mathbf{I}) + \frac{1}{3}\mathrm{P}(\mathbf{mm} - \mathbf{ll}) \tag{4}$$

where the following restrictions apply:

$$\mathbf{Q} = \mathbf{Q}^{\mathrm{T}};\ \mathrm{tr}(\mathbf{Q}) = 0; -\frac{1}{2} \le \mathrm{S} \le 1; -\frac{3}{2} \le \mathrm{P} \le \frac{3}{2} \tag{5a,b,c,d}$$

$$\mathbf{n} \cdot \mathbf{n} = \mathbf{m} \cdot \mathbf{m} = \mathbf{l} \cdot \mathbf{l} = 1;\ \mathbf{nn} + \mathbf{mm} + \mathbf{ll} = \mathbf{I} = \begin{bmatrix} 1 & 0 & 0 \\ 0 & 1 & 0 \\ 0 & 0 & 1 \end{bmatrix} \tag{6a,b}$$

the uniaxial director **n** corresponds to the maximum eigenvalue $\mu_n = \frac{2}{3}\mathrm{S}$, the biaxial director **m** corresponds the second largest eigenvalue $\mu_m = -\frac{1}{3}(\mathrm{S} - \mathrm{P})$, and the second biaxial director **l** (=**n**×**m**) corresponds to the smallest eigenvalue $\mu_l = -\frac{1}{3}(\mathrm{S} + \mathrm{P})$. The orientation is defined completely by the orthogonal director triad (**n, m, l**). The magnitude of the uniaxial scalar order parameter S is a measure of the molecular alignment along the uniaxial director **n**, and is given as $S = \frac{3}{2}(\mathbf{n}\cdot\mathbf{Q}\cdot\mathbf{n})$. The magnitude of the biaxial scalar order parameter P is a measure of the molecular alignment in a plane perpendicular to the direction of uniaxial director **n**, and is given as $P = \frac{3}{2}(\mathbf{m}\cdot\mathbf{Q}\cdot\mathbf{m} - \mathbf{l}\cdot\mathbf{Q}\cdot\mathbf{l})$. On the principal axes, the tensor order parameter **Q** is represented as:

$$\mathbf{Q} = \begin{bmatrix} -\frac{1}{3}(S-P) & 0 & 0 \\ 0 & -\frac{1}{3}(S+P) & 0 \\ 0 & 0 & \frac{2}{3}S \end{bmatrix} \tag{7}$$

both S and P are positive for normal DNLCs. The Landau-de Gennes model uses the tensor order parameter to describe nematic ordering. According to equation (7), the model is able to describe biaxial ($S \neq 0,\ P \neq 0$), uniaxial ($S \neq 0$, P=0), and isotropic (S=0, P=0) states.

5.3.2 Definition of Coordinate System

Figure 5.5 shows the fiber geometry and the rectangular (x,y) dimensionless coordinate system used in this paper. The vertical distance y is scaled with R_y*: y*=2y/R_y*, and spans the interval: $-0.5 \leq y^* \leq +0.5$. The distance between the center of the two semi-circles of radius R_y*/2 is R_x*. The axial ratio is A_r= R_x*/R_y*. The horizontal distance x is scaled with R_y: x*=2x/R_y*, and spans the interval $-(A_r/2+0.5) \leq x^* \leq +(A_r/2+0.5)$. For a circular fiber A_r=0. For brevity we let R_y*/2=R.

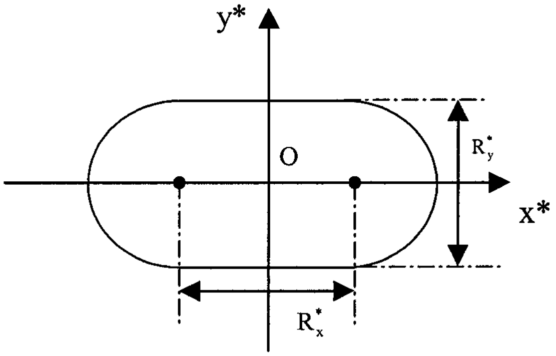

Figure 5.5: Definition of fiber geometry and rectangular (x, y) dimensionless coordinate system used in this paper. The vertical distance y is scaled with R_y: $y^*=2y/R_y$, and spans the interval: $-0.5 \le y^* \le +0.5$. The distance between the center of the two semi-circles of radius $R_y/2$ is R_x. The axial ratio is $A_r= R_x/R_y$. The horizontal distance x is scaled with R_y: $x^*=x/R_y$, and spans the interval: $-(A_r/2+0.5) \le x^* \le +(A_r/2+0.5)$. For a circular fiber $A_r=0$. For brevity we let $R_y/2=R$.

5.3.3 Landau-de Gennes Mesoscopic Model for Liquid Crystalline Materials

According to the Landau-de Gennes model, the bulk energy density of nematic liquid crystals (NLC) in the absence of external fields is given by [27,28]:

$$f_b = f_0 + f_s + f_\ell \quad ; \quad f_\ell = f_{\ell 2} + f_{\ell 3} \tag{8a,b}$$

$$f_s = A\mathbf{Q}:\mathbf{Q} + B\mathbf{Q}:(\mathbf{Q}\cdot\mathbf{Q}) + C(\mathbf{Q}:\mathbf{Q})^2 \tag{8c}$$

$$f_{\ell 2} = L_1 \nabla\mathbf{Q} : (\nabla\mathbf{Q})^T + L_2(\nabla\cdot\mathbf{Q})\cdot(\nabla\cdot\mathbf{Q}) \tag{8d}$$

$$f_{\ell 3} = L_3\mathbf{Q} : (\nabla\mathbf{Q} : \nabla\mathbf{Q}) + \cdots \tag*{8(e)}$$

where A, B, C, L_1, L_2, L_3, … are coefficients of the specified terms. f_0 is the free energy density of the isotropic state. The term is related to the conventional thermodynamic parameters, like temperature and pressure, and independent to **Q**. f_s is the short-range energy density, which is responsible for the nematic-isotropic phase transition, f_ℓ is the long range energy, $f_{\ell 2}$ is the second order long range free energy density, and $f_{\ell 3}$ is the third order contribution to the long range free energy density. By assuming that **Q** is uniaxial and comparing $f_{\ell 2}$ with f_n (eqn.(1)) it is found that $K_{11}=K_{33}$. To remove this restriction $f_{\ell 3}$ must be non-zero. It is known that there are six different third-order expressions. For rod-like nematics it was shown that representative experimental $\{K_{ii}\}$;

(ii=11, 22, 33) data is well captured by retaining only the term $L_3\mathbf{Q}_{\alpha\beta}\,\mathbf{Q}_{\gamma\delta\,,\alpha}\mathbf{Q}_{\gamma\delta\,,\beta}$ in the $f_{\ell 3}$ expression [29]. The same approach will be used in this paper. Using the one parameter Doi model for f_s [30], the dimensionless free energy densities are given by:

$$f_s^* = \frac{3}{U}\left(\frac{1}{2}\left(1-\frac{1}{3}U\right)\mathbf{Q}:\mathbf{Q}-\frac{1}{3}U\mathbf{Q}:(\mathbf{Q}\cdot\mathbf{Q})+\frac{1}{4}U(\mathbf{Q}:\mathbf{Q})^2\right) \tag{9a}$$

$$f_{\ell 2}^* = \frac{L_1}{2ckT^*R^2}\left[\tilde{\nabla}\mathbf{Q}:\left(\tilde{\nabla}\mathbf{Q}\right)^T\right]+\frac{L_2}{2ckT^*R^2}\left(\tilde{\nabla}\cdot\mathbf{Q}\right)\cdot\left(\tilde{\nabla}\cdot\mathbf{Q}\right) \tag{9b}$$

$$f_{\ell 3}^* = \frac{L_3}{2ckT^*R^2}\left[\mathbf{Q}:\left(\tilde{\nabla}\mathbf{Q}:\tilde{\nabla}\mathbf{Q}\right)\right] \tag{9c}$$

where U is the nematic potential, which is inversely proportional to the temperature in a thermotropic liquid crystal, and c, k, T* are the number density of discs, the Boltzmann's constant, and an absolute reference temperature just below the isotropic-nematic phase transition temperature, respectively. Comparing eqn.(1) the Landau coefficients $\{L_i\}$,i=1,2,3 are related to the Frank's constant of uniaxial LCs in the following way [5,29]:

$$L_1 = \frac{3K_{22}-K_{11}+K_{33}}{6S^2}\ ,\ L_2 = \frac{K_{11}-K_{22}}{S^2}, L_3 = \frac{K_{33}-K_{11}}{2S^3} \tag{10a, b, c}$$

$$K_{11} = S^2\left(2L_1+L_2-\frac{2}{3}SL_3\right) \tag{11a}$$

$$K_{22} = S^2\left(2L_1-\frac{2}{3}SL_3\right) \tag{11b}$$

$$K_{33} = S^2\left(2L_1+L_2+\frac{4}{3}SL_3\right) \tag{11c}$$

Using eqns.(11) and inequalities (2) the following restrictions have to be obeyed under uniaxial ordering:

$$2L_1+L_2-\frac{2}{3}SL_3\geq 0;\ 2L_1-\frac{2}{3}SL_3\geq 0;\ 2L_1+L_2+\frac{4}{3}SL_3\geq 0 \tag{12a, b, c}$$

In addition, since twist is the highest elastic constant in DNLCs, the Landau coefficient L_2 is negative [7, 26]:

$$L_2<0 \tag{13}$$

The governing equations for liquid crystal flows follow the dissipation function Δ:

$$\Delta = \mathbf{t}^{s} : \mathbf{A} + \mathrm{ckT}\mathbf{H}.\hat{\mathbf{Q}} \tag{14}$$

where $\mathbf{t}^{s}$ is the symmetric viscoelastic stress tensor, **A** is the symmetric traceless rate of deformation tensor, **H** is the molecular field, and $\hat{\mathbf{Q}}$ is the Jaumann derivative of the tensor order parameter, given by:

$$\mathbf{A} = \tfrac{1}{2}\left(\nabla\mathbf{v} + \nabla\mathbf{v}^{T}\right) \quad ;\hat{\mathbf{Q}} = \frac{\partial\mathbf{Q}}{\partial t} + (\mathbf{v}\cdot\nabla)\mathbf{Q} - \mathbf{W}\cdot\mathbf{Q} + \mathbf{Q}\cdot\mathbf{W}\,; \quad \mathbf{W} = \tfrac{1}{2}\left(\nabla\mathbf{v} - \nabla\mathbf{v}^{T}\right) \tag{15}$$

$$(\mathrm{ckT})\mathbf{H} = -\left[\frac{\delta F}{\delta\mathbf{Q}}\right]^{[s]} = \left[\frac{\partial f_b}{\partial\mathbf{Q}} - \nabla\cdot\frac{\partial f_b}{\partial\nabla\mathbf{Q}}\right]^{[s]} \tag{16}$$

where [s] indicates the symmetric and traceless, **A** is the rate of deformation tensor, **W** is the vorticity tensor, and $\frac{\delta F}{\delta\mathbf{Q}}$ is the functional derivative of the total energy F. Expanding the forces ($\mathbf{t}^{s}$, $\hat{\mathbf{Q}}$) in terms of fluxes (A, ckT**H**), and taking into account thermodynamic restrictions and the symmetry and tracelessness of the forces and fluxes we can obtain the equations for $\mathbf{t}^{s}$ and $\hat{\mathbf{Q}}$. The dynamics of the tensor order parameter is given by [22]:

$$\begin{aligned}
\hat{\mathbf{Q}} = {} & \tfrac{2}{3}\beta\mathbf{A} + \beta\left[\mathbf{A}\cdot\mathbf{Q} + \mathbf{Q}\cdot\mathbf{A} - \tfrac{2}{3}(\mathbf{A}:\mathbf{Q})\mathbf{I}\right] - \\
& \tfrac{1}{2}\beta\left[(\mathbf{A}:\mathbf{Q})\mathbf{Q} + \mathbf{A}\cdot\mathbf{Q}\cdot\mathbf{Q} + \mathbf{Q}\cdot\mathbf{A}\cdot\mathbf{Q} + \mathbf{Q}\cdot\mathbf{Q}\cdot\mathbf{A} - \{(\mathbf{Q}\cdot\mathbf{Q}):\mathbf{A}\}\mathbf{I}\right] \\
& - 6\overline{\mathrm{Dr}}\left\{\begin{array}{l} \frac{3}{U}\left[\left(1-\frac{1}{3}U\right)\mathbf{Q} - U\left(\mathbf{Q}\cdot\mathbf{Q} - \frac{1}{3}(\mathbf{Q}:\mathbf{Q})\mathbf{I}\right) + U(\mathbf{Q}:\mathbf{Q})\mathbf{Q}\right] \\ + \frac{L_3}{2\mathrm{ckT}^{*}}\left[(\nabla\mathbf{Q}:\nabla\mathbf{Q}) - \frac{1}{3}\mathrm{tr}(\nabla\mathbf{Q}:\nabla\mathbf{Q})\mathbf{I}\right] \end{array}\right\} \\
& + 6\overline{D_r}\left[\begin{array}{l} \frac{L_1}{\mathrm{ckT}^{*}}\nabla^{2}\mathbf{Q} + \frac{L_2}{2\mathrm{ckT}^{*}}\left(\nabla(\nabla\cdot\mathbf{Q}) + [\nabla(\nabla\cdot\mathbf{Q})]^{T} - \frac{2}{3}\mathrm{tr}[\nabla(\nabla\cdot\mathbf{Q})]\mathbf{I}\right) \\ + \frac{L_3}{\mathrm{ckT}^{*}}((\nabla\cdot\mathbf{Q})\cdot\nabla\mathbf{Q}) + \frac{L_3}{\mathrm{ckT}^{*}}(\mathbf{Q}:(\nabla\nabla\mathbf{Q})) \end{array}\right]
\end{aligned} \tag{17a}$$

$$\overline{D_r} \approx D_r\frac{1}{\left(1-(3/2)\mathbf{Q}:\mathbf{Q}\right)^{2}}, \quad D_r = \frac{\mathrm{ckT}}{6\eta} \tag{17b,c}$$

where β is a material shape parameter, $\overline{D_r}$ is the microstructure dependent rotational diffusivity, D_r is the preaveraged rotational diffusivity or isotropic diffusivity, which is independent of **Q**, and η is a viscosity. Non-dimensioning equation (17) yields:

$$\frac{d\mathbf{Q}}{dt^*} = \mathbf{S} + \mathbf{L} + \mathbf{F} \tag{18a}$$

$$\mathbf{S} = -\frac{1}{U}\frac{3}{U}\left[1-\frac{3}{2}(\mathbf{Q}:\mathbf{Q})\right]^{-2}\left[\left(1-\frac{1}{3}U\right)\mathbf{Q} - U\left(\mathbf{Q}\cdot\mathbf{Q}-\frac{1}{3}(\mathbf{Q}:\mathbf{Q})\mathbf{I}\right)+U(\mathbf{Q}:\mathbf{Q})\mathbf{Q}\right] \tag{18b}$$

$$\begin{aligned}\mathbf{L} = {} & \frac{\xi^2}{R^2}\frac{1}{U}\left[1-\frac{3}{2}(\mathbf{Q}:\mathbf{Q})\right]^{-2}\left\{\begin{array}{l}\tilde{\nabla}^2\mathbf{Q}+\frac{\tilde{L}_2}{2}\left[\tilde{\nabla}(\tilde{\nabla}\cdot\mathbf{Q})+\left[\tilde{\nabla}(\tilde{\nabla}\cdot\mathbf{Q})\right]^T-\frac{2}{3}\mathrm{tr}\left[\tilde{\nabla}(\tilde{\nabla}\cdot\mathbf{Q})\right]\mathbf{I}\right] \\ +\tilde{L}_3\left((\tilde{\nabla}\cdot\mathbf{Q})\cdot\tilde{\nabla}\mathbf{Q}\right)+\tilde{L}_3\left(\mathbf{Q}:(\tilde{\nabla}\tilde{\nabla}\mathbf{Q})\right)\end{array}\right\} \\ & -\frac{\xi^2}{R^2}\frac{1}{U}\frac{\tilde{L}_3}{2}\left[1-\frac{3}{2}(\mathbf{Q}:\mathbf{Q})\right]^{-2}\left[(\tilde{\nabla}\mathbf{Q}:\tilde{\nabla}\mathbf{Q})-\frac{1}{3}\mathrm{tr}(\tilde{\nabla}\mathbf{Q}:\tilde{\nabla}\mathbf{Q})\mathbf{I}\right]\end{aligned} \tag{18c}$$

$$\mathbf{F} = De\left\{\begin{array}{l}\frac{2}{3}\beta\tilde{\mathbf{A}}+\beta\left[\tilde{\mathbf{A}}\cdot\mathbf{Q}+\mathbf{Q}\cdot\tilde{\mathbf{A}}-\frac{2}{3}(\tilde{\mathbf{A}}:\mathbf{Q})\mathbf{I}\right]- \\ \frac{1}{2}\beta\left[(\tilde{\mathbf{A}}:\mathbf{Q})\mathbf{Q}+\tilde{\mathbf{A}}\cdot\mathbf{Q}\cdot\mathbf{Q}+\mathbf{Q}\cdot\tilde{\mathbf{A}}\cdot\mathbf{Q}+\mathbf{Q}\cdot\mathbf{Q}\cdot\tilde{\mathbf{A}}-\{(\mathbf{Q}\cdot\mathbf{Q}):\tilde{\mathbf{A}}\}\mathbf{I}\right]\end{array}\right\} \tag{18d}$$

where $t^* = t\frac{3ckT^*}{\eta}$ is dimensionless time, **S** is the short-range contribution, and **L** is the long-range distribution, **F** is the flow effect, $U = \frac{3T^*}{T}$ is dimensionless temperature, $\xi = \sqrt{\frac{L_1}{ckT^*}}$ is molecular length scale, $\tilde{L}_2 = \frac{L_2}{L_1}$ and $\tilde{L}_3 = \frac{L_3}{L_1}$ are ratios of elastic coefficients, R is geometry length scale (i.e. the fiber radius), $D_e = \dot{\gamma}\eta/ckT^*$ is the Deborah number, and $\dot{\gamma}$ is a characteristic deformation rate. Since all the flow effects we wish to discuss in this paper are captured by the leading order term in **F,** without loss of relevant physics we use:

$$\mathbf{F} = \tfrac{2}{3}\beta\tilde{\mathbf{A}}De = -D_e^*\tilde{\mathbf{A}} \qquad ;\ D_e^* = -\tfrac{2}{3}\beta De \tag{19}$$

The dimensionless parameters of the model are: U, $\mathcal{R} = \frac{R}{\xi}$, $\tilde{L}_2$, $\tilde{L}_3$, De, and the aspect ratio A_r of the ribbon fiber. The nematic potential U is a dimensionless temperature that controls the equilibrium order parameter S_{eq} at the phase transition. According to the Doi model of the short-range energy, the temperature dependence of S at equilibrium is [30]:

$$S_{eq} = \frac{1}{4} + \frac{3}{4}\sqrt{\left(1 - \frac{8}{3U}\right)}, \; U = \frac{3T^*}{T} \qquad (20a,b)$$

where T* is a reference temperature just below the isotropic-nematic phase transition temperature like we defined before. For U<8/3 the stable phase is isotropic, for $8/3 \le U \le 3$ there is biphasic equilibrium, and for higher values of U the phase is uniaxial nematic. In this work, we have used $2.7 \le U \le 6.55$. The parameter $\mathcal{R} = \frac{R}{\xi}$ is the ratio of the fiber radius to the internal length scale (ξ). The internal length scale represents the characteristic size of a defect core and is usually much smaller than the system size R. In this work, we have used $0<\mathcal{R} = \frac{R}{\xi}<250$. When $\mathcal{R} = \frac{R}{\xi}<<1$, long-range energy dominates, spatial gradients are costly and homogeneous states are selected. On the other hand, when $\mathcal{R} = \frac{R}{\xi}>>1$, long-range elasticity is insignificant with respect to short-range elasticity and defects proliferate, since spatially, non-homogeneous states are energetically not costly. The elastic constants ratios $\tilde{L}_2 = \frac{L_2}{L_1}$ and $\tilde{L}_3 = \frac{L_3}{L_1}$ are two measures of elastic anisotropy. When $\tilde{L}_2$, $\tilde{L}_3$ are equal to zero, all elastic modes (K_{11}, K_{22}, K_{33}) have the same elastic modulus. To satisfy the thermodynamic restrictions (12,13), we set $\tilde{L}_2 = -0.5$ throughout and limit the range of $\tilde{L}_3$ to: $-1.125 \le S\tilde{L}_3 \le 2.25$. The parameter De is the Deborah number and is the ratio of viscous effects to short range elasticity. In this paper 0<De<1, which means that flow is weak compared to short range elasticity, and hence in the absence of disclination lines the scalar order parameters remain equal to their equilibrium value. $S=S_{eq}$, P=0.

The governing equation (18) is solved in the ribbon geometry, shown in Fig. 5.5; in this paper we explore the following shapes: $0 \le A_r \le 1$. The boundary conditions of the model are:

$$t^*>0, \; \mathbf{x} = \mathbf{x}_b^*, \; \mathbf{Q}=\mathbf{Q}_{eq}$$

$$\mathbf{Q}_{eq} = S_{eq}\left(\mathbf{nn} - \frac{1}{3}\mathbf{I}\right) \qquad (21)$$

where $\mathbf{x}_b^*$ is the dimensionless position vector of the boundary. The Dirichlet boundary condition sets the eigenvalues of uniaxial tensor order parameter equal to its equilibrium value ($S=S_{eq}$), and the distinct eigenvector **n** is tangential to the ribbon surface. The initial conditions are:

$$t^*=0,\ \mathbf{Q}_{ini} = S_{ini}(\mathbf{n}_{ini}\mathbf{n}_{ini} - \frac{1}{3}\mathbf{I}) + \frac{1}{3}P_{ini}(\mathbf{m}_{ini}\mathbf{m}_{ini} - \mathbf{l}_{ini}\mathbf{l}_{ini}) \tag{22}$$

where the values of S_{ini} and P_{ini}, and $\mathbf{n}_{ini}$, $\mathbf{m}_{ini}$, and $\mathbf{l}_{ini}$ depend on the texture and will be explicitly defined below for each case.

The model equation (18) is a set of six coupled non-linear parabolic partial differential equations, solved in the circle, subjected the auxiliary conditions (see equations (21, 22). The equations are solved using Galerkin Finite Elements with Lagrangean linear basis functions for spatial discretization and a fifth order Runge-Kutta-Cash-Karp time adaptive method [31]. Convergence and mesh-independence were established in all cases using standard methods. Spatial and temporal discretization was judiciously selected taking into account the shortest length and smallest time scales of our model, as discussed below.

5.3.4 Length and Time Scales in the Landau-de Gennes Model

The formation and structure of mesophase fiber textures is better understood by considering the governing time and length scales included in the Landau-de Gennes model. The Landau-de Gennes model for nematic liquid crystals has an external length scale L_e and an internal length scale L_i as follows:

$$L_e=R,\ L_i = \xi = \sqrt{\frac{L_1}{ckT^*}} \tag{23a,b}$$

where R is the characteristic ribbon fiber half-thickness, and where the length scales obey $L_e >> L_i$. If defects are present, the mesh size has to be commensurate with L_i. It should be noted that the long external length scale governs the directors' orientation **(n, m, l)** while the short internal length scale governs the scalar order parameter (S, P). In addition, care should be taken to select an appropriate time integration technique to overcome the intrinsic stiffness of the system. The model equations contain an internal time scale τ_i

and an external elastic time scale τ_e and an external flow time scale τ_f. The internal time scale governs the evolution of the scalar order parameters (S, P) and is given by

$$\tau_i = \frac{\eta}{ckT^*} \tag{24}$$

A much longer external elastic time scale τ_e controls the evolution of the directors and is given by:

$$\tau_e = \frac{\eta L_e^2}{L_1} \tag{25}$$

The selected adaptive time integration scheme is able to efficiently take into account the stiffness that rises due to the disparity between time scale: $\tau_i << \tau_e$. In addition the external flow time scale τ_f is just the reciprocal of the flow deformation rate. For example in shear flow with a shear rate $\dot{\gamma}$ the flow time scale is $\tau_f=1/\dot{\gamma}$. Flow-induced orientation occurs when:

$$\tau_i << \tau_f < \tau_e; \qquad D_e << 1 < \frac{\tau_e}{\tau_f} \tag{26a, b}$$

As mentioned above, in this regime the flow affects the eigenvectors of **Q**, but does not affect the eigenvalues of **Q**. For the flow to change the scalar order parameters (S, P), the time scale τ_i has to be fast enough such that $\tau_f < \tau_i$. Thus the effect flow on texture formation is captured through flow-induced orientation.

5.4 Flow-Induced Orientation

This subsection presents analytical results of flow-induced orientation pertinent to the analysis of the ribbon planar line texture. Since in the flow-regime of interest the eigenvalues of the tensor order parameter remain unaffected by the flow, the governing eqn. (18) can be simplified if the following assumptions hold: (a) no disclination lines are present, (b) the flow is sufficiently weak such that inequalities (26) hold, (c) the system is spatially homogeneous. In this case the tensor order parameter simplifies to:

$$\mathbf{Q} = S_{eq}(\mathbf{nn} - \mathbf{I}/3) \tag{27}$$

Substituting this expression into eqn. (18) we obtain the dynamical equation DE for the tensor **nn**. To obtain the dynamical equation for the director **n** we proceed as follows. (1)

Take the dot product of the DE for **nn** with **n**, and (2) project the resulting equation with the projection tensor **(I-nn)**. The resulting equation is the dynamical equation for the director in the absence of long range and short range elasticity, as follows:

$$\mathbf{N} = \frac{\partial \mathbf{n}}{\partial t} + \mathbf{v}.\nabla\mathbf{n} + \mathbf{W}.\mathbf{n} = \lambda(\mathbf{A}.\mathbf{n} - \mathbf{A}:\mathbf{nnn}); \qquad \lambda = -\frac{\gamma_2}{\gamma_1} = \frac{\beta(4+2S-S^2)}{6S} \qquad (28a, b)$$

where λ is the reactive parameter, which for DNLC is negative [26]: $\lambda<0$, γ_1 is the rotational viscosity, and γ_2 is the irrotational torque coefficient. The equation predicts the following steady state flow-induced orientation results, in a rectangular (x, y, z) coordinate system. We shall consider the case of $\lambda<-1$, when the aligning effect of the rate of deformation tensor **A** overcomes the tumbling effect of the vorticity tensor **W**.

(a) Steady Simple Shear Flow Alignment

For steady simple shear between two parallel flat plates, the velocity profile is $\mathbf{v} = (\dot{\gamma}y, 0, 0)$. Considering in-plane 2D orientation, the director field is: **n**= (cosθ, sinθ, 0). Substituting **v**, and **n** in the governing eqn. (28) we find that a stable steady state orientation at:

$$\cos 2\theta_L = -\frac{1}{\lambda}; \qquad \lambda < -1; \qquad \frac{\pi}{2} < \theta_L < \frac{3\pi}{4} \qquad (29)$$

where θ_L is the Lelsie angle, which usually is close to $\pi/2$, since λ is close to -1. Thus a simple shear flow of a DNLC aligns the director close to the velocity gradient (y) direction. We recall that in shear flow two particles that were separated at a distance l_o, after being subjected to a shear rate of $\dot{\gamma}$ for time t, the separation distance *l* is $l = l_o$ t. Due to the linear time increase in separation shear flows are considered weak flows as compared with elongational flows.

(b) Elongational Flow Alignment

Shear-free elongational flows have the following velocity profiles:

$$\mathbf{v} = \begin{pmatrix} v_x \\ v_y \\ v_z \end{pmatrix} = \begin{pmatrix} -\frac{1}{2}\dot{\varepsilon}(1+b)x \\ -\frac{1}{2}\dot{\varepsilon}(1-b)y \\ \dot{\varepsilon}z \end{pmatrix} \qquad (30)$$

According to the values of the two parameters the following elongational flows arise: (1) uniaxial elongational flow, b=0, $\dot{\varepsilon} > 0$; (2) biaxial stretching flow, b=0 $\dot{\varepsilon} < 0$, (3) planar elongational flow, b=1, $\dot{\varepsilon} > 0$. In elongational flows the vorticity is zero, **W**=0, and the rate of deformation **A** is a diagonal tensor:

$$\mathbf{A} = \begin{bmatrix} -\frac{1}{2}\dot{\varepsilon}(1+b) & 0 & 0 \\ 0 & -\frac{1}{2}\dot{\varepsilon}(1-b) & 0 \\ 0 & 0 & \dot{\varepsilon} \end{bmatrix} \tag{31}$$

The eigenvectors of this tensor are: (**i, j, k**) the three unit vectors of the rectangular coordinate system. Under elongational flows, the director dynamical eqn. (28) simplifies to:

$$\mathbf{0} = \lambda(\mathbf{A.n} - \mathbf{A:nnn}) \tag{32}$$

which is satisfied only if the director **n** is along the eigenvectors (**i, j, k**) of **A**,

$$\mathbf{A.n} = (\mathbf{A:nn})\mathbf{n} = \mu\mathbf{n} \tag{33}$$

where μ represents an eigenvalue of **A**. It turns out the selected stable unit vector(s) is (are) the one (ones) corresponding to the compression direction (plane) of the elongational flow. For the defined elongational flows the compression directions (or planes) are: (1) uniaxial elongational flow: x-y plane, (2) biaxial stretching flow: z-axis, (3) planar elongational flow: x-axis. Hence the stable director orientations are: (1) uniaxial elongational flow: $\mathbf{n}\perp\mathbf{k}$ (2) biaxial stretching flow: $\mathbf{n}//\mathbf{k}$, (3) planar elongational flow, $\mathbf{n}//\mathbf{i}$. We recall that in elongational flow two particles that were separated at a distance l_o, after being subjected to a elongation rate of $\dot{\varepsilon}$ for time t, the separation distance l is $l=l_o\exp(\dot{\varepsilon}t)$. Due to the exponential time increase in separation shear flows are considered strong flows as compared with shear flows.

(c) Mixed Elongational-Shear Flow Alignment

Simulations of microstructure evolution in non-viscometric flows of aligning nematics using the LE equations have been performed for Jeffrey-Hamel [32] and radial out-flow flow between disks [13]. Viscous torques includes shear and elongation, and the stable orientation is achieved by balancing the two torques. The Jeffrey-Hamel flow geometry is best described in (r, ψ, z) cylindrical coordinates. The shear plane is spanned by (r, ψ), and z is along the vorticity axis. The IP director angle is θ and the director and velocity fields are $\mathbf{n}(\psi)=(\cos\theta, \sin\theta, 0)$; $\mathbf{v}(\psi)=(u,0,0)$. For converging (diverging) flow $u < 0$ ($u > 0$). The stable centerline director is along the compresion direction, which for converging (diverging) flow is along radial azimuthal (radial) direction. The viscous torque balance yields, at steady state, the following director equation:

$$[\lambda\cos 2\theta - 1]\,\frac{u'}{2} + [\lambda \sin 2\theta]\, u = 0 \tag{34}$$

The stable solutions, consistent with the centerline orientations for diverging and converging flows, are, respectively:

$$\psi > 0,\ \ \theta_a^+ = \tan^{-1}\left[\frac{2\lambda\ u - \sqrt{4\lambda^2 u^2 + \left(\lambda^2 - 1\right)u'^2}}{u'(1+\lambda)}\right]; \psi < 0,\ \ \theta_a^- = -\pi - \theta_a^+ \tag{35a}$$

$$\psi > 0,\ \ \theta_a^+ = \tan^{-1}\left[\frac{2\lambda\ u + \sqrt{4\lambda^2 u^2 + \left(\lambda^2 - 1\right)u'^2}}{u'(1+\lambda)}\right]; \psi < 0,\ \theta_a^- = -\theta_a^+ \tag{35b}$$

In the centerline (wall) region elongation (shear) dominates. Both shear and extension promote aligning close to the azimuthal direction for converging flow, while for diverging flow shear promotes azimuthal alignment and elongation radial alignment. Thus, at high flow rates, converging (diverging) flows have weak (strong) orientation gradients. These results are a consequence of the fact that extension and compression are co-planar with shear, and their magnitudes have the same radial dependence.

Mixed elongational-shear flows such as the converging rectangular channel flow present in the processing of the ribbon-shaped mesophase fibers is a complex 3D flow, where $\mathbf{W} \neq \mathbf{0}$, and $\mathbf{A}$ is a full matrix. Exact solutions for converging and/or diverging channel flows, of interest in this paper, do not exists and numerical solutions are required. Nevertheless based on the existing experimental data on rectangular converging die flow [1] some qualitative predictions on converging channel flow-induced orientation can be made based on the previous discussion. Assuming a rectangular (x, y) cross section and primary flow in the z-direction the rate of deformation tensor $\mathbf{A}$ is:

$$\mathbf{A} = \begin{bmatrix} A_{xx} & 0 & A_{xz} \\ 0 & A_{yy} & A_{yz} \\ A_{xz} & A_{yz} & -(A_{xx}+A_{yy}) \end{bmatrix} \tag{36}$$

The compression directions are the x and y-axes, and the velocity gradient directions are also the x and y-axes. Thus in this type of mixed elongation-shear converging channel flow the preferred orientation is the x-y plane.

The experimental results [1] on mesophase carbon fibers of ribbon cross-section indicate that the structure was subjected to a strong orienting field, thus creating an inversion wall. Based on the above discussions, since converging channel flow produces a planar 2D orientation the structuring must then occur by a nearly planar extensional flow in the spin line, in which the ratio of the long to short axes of the ribbon is reduced, thus creating a compression field that orients the director.

5.5 Computational Results and Discussion

This section presents representative computational results obtained by solving the model eqns. (18). To visualize the fiber textures we use the computed solution tensor **Q**, and represent the discotic mesophase by a cuboid **C** whose axes are normal to the directors (**n**, **m**, **l**) and sides are proportional to its eigenvalues. Since **Q** has negative eigenvalues, we use $\mathbf{M} = \mathbf{Q} + \frac{1}{3}\mathbf{I}$ instead of **Q**. In what follows the horizontal semi axis (along x*) is refereed as the fiber's long semi axis, and the vertical semi axis (along y*) as the fiber's short semi axis.

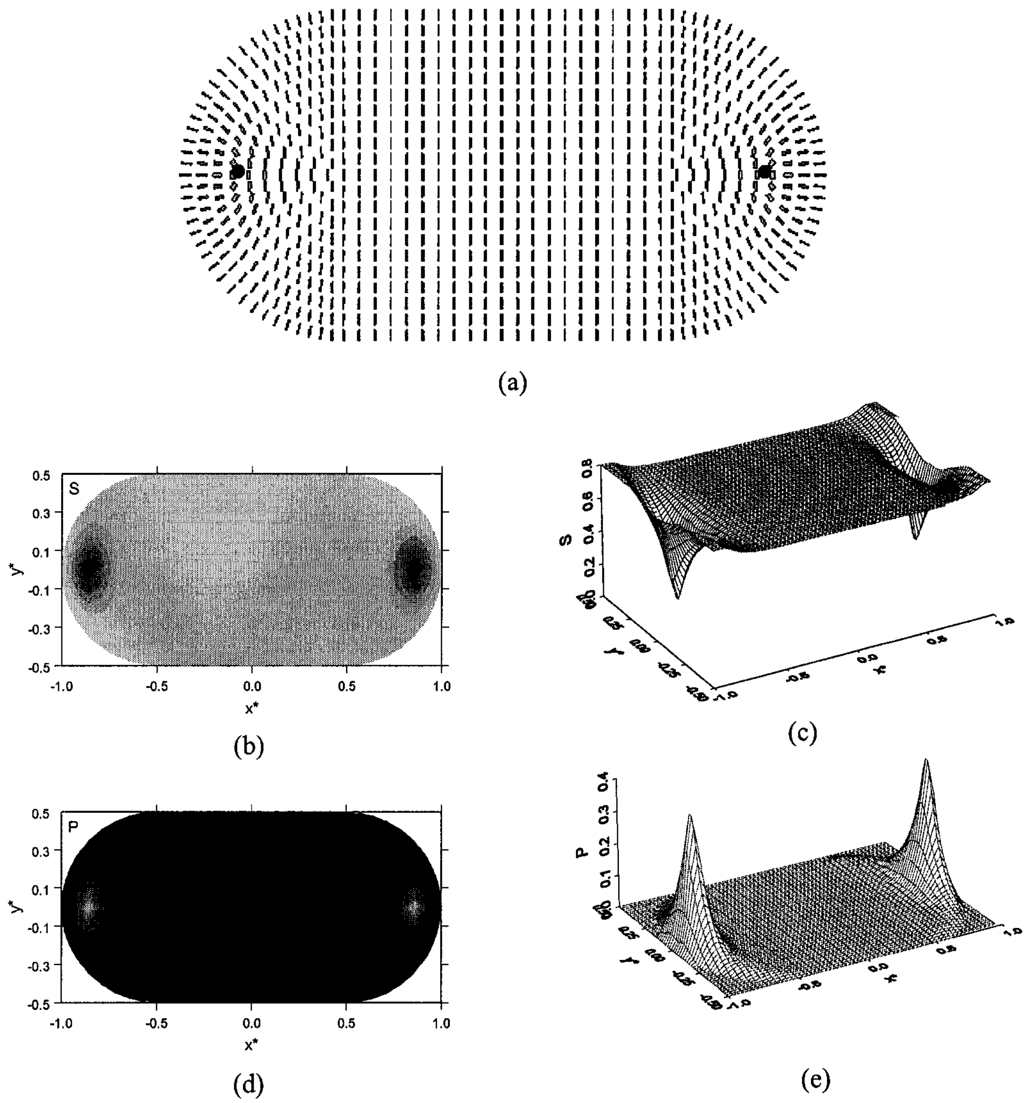

Figures 5.6: Computed visualizations of a representative steady state RPP texture, for U=4.55, $\mathcal{R}=10$, $\tilde{L}_2=-0.5$, $\tilde{L}_3=0$, De=0, and A_r=1. Figure 5.6a is a representative typical steady state visualization of tensor order parameter **C**. It clearly shows the molecular orientation of planar polar texture, with the two s=+1/2 defects collinear with the fiber long axis. Figures 5.6b, 5.6c show a gray-scale plot and a surface plot of the uniaxial scalar order parameter S as a function of dimensionless position (x*, y*). In the gray-scale plot a low order parameter ($S \approx 0$) is black and high order parameter ($S \approx 1$) is white. The dark dots in the figure correspond to the two s=+1/2 defects. Figures 5.6d, 5.6e shows a gray-scale plot and a surface plot of the biaxial scalar order parameter P as a function of dimensionless position (x*, y*). In the gray-scale plot a low order parameter ($P \approx 0$) is black and high order parameter ($P \approx 1$) is white. The dark dots in the figure correspond to the two s=+1/2 defects.

5.5.1 Formation and Structure of the Ribbon Planar Polar Texture

Figures 5.6 show computed visualizations of a representative steady state RPP texture, for U=4.55, $\mathcal{R}=10$, $\tilde{L}_2=-0.5$, $\tilde{L}_3=0$, De=0, and A_r=1. Figure 6a is a representative typical steady state visualization of tensor order parameter **C**. It clearly shows the molecular orientation of planar polar texture, with the two s=+1/2 defects collinear with the fiber long axis. The simulations show the bending distortions close to the two defects and an aligned region between the two defects. Figures 5.6b, 5.6c shows a gray-scale plot and a surface plot of the uniaxial scalar order parameter S as a function of dimensionless position (x*, y*). In the gray-scale plot a low order parameter ($S \approx 0$) is black and high order parameter ($S \approx 1$) is white. The dark dots in the figure correspond to the two s=+1/2 defects. The narrow peaks in the surface plots indicate the difference in scale between defect cores and fiber radius. At the defects' core S is small, as expected. Figures 5.6d, 5.6e show the corresponding gray-scale and surface plots of the biaxial order parameters P as a function of dimensionless position (x*, y*). In the gray-scale plot, $P \approx 0$ corresponds to black and $P \approx 1$ to white. The figure clearly shows the biaxial eigenvalues of **Q** at the two defect cores. The corresponding surface plot shows that at the defects core $P \approx 0.3$. Far from the disclination the state is uniaxial. Biaxiality arises because it reduces long range elasticity.

Figure 5.7 shows the formation kinetics and structural evolution of the ribbon planar polar texture, for U=4.55, $\mathcal{R}=50$, $\tilde{L}_2=-0.5$, $\tilde{L}_3=0$, De=0, and A_r=1. Figure 5.7a-d show visualizations of **M** as a function of increasing dimensionless time t*: (a). 50, (b) 70, (c) 80, and (d) steady state. The orientation develops as a moving front towards the interior. Figure 5.7e shows the dimensionless long range free energy f_l^* as a function of dimensionless time t*. The energy decreases, until it reaches plateau (corresponding to Fig. 5.7c), and then the residual energy from gradients at the centerline (y*=0) vanishes leading to a homogeneous well-aligned region (corresponding to Fig. 5.7d). Note that the energy does not relax to zero because bend distortions remain in the semi-circular end-regions. Note that at t*=70 the fiber texture is very similar to the ribbon planar line texture, but since a lower energy state is available with no energy of activation barriers, the selected fiber is the ribbon planar polar texture.

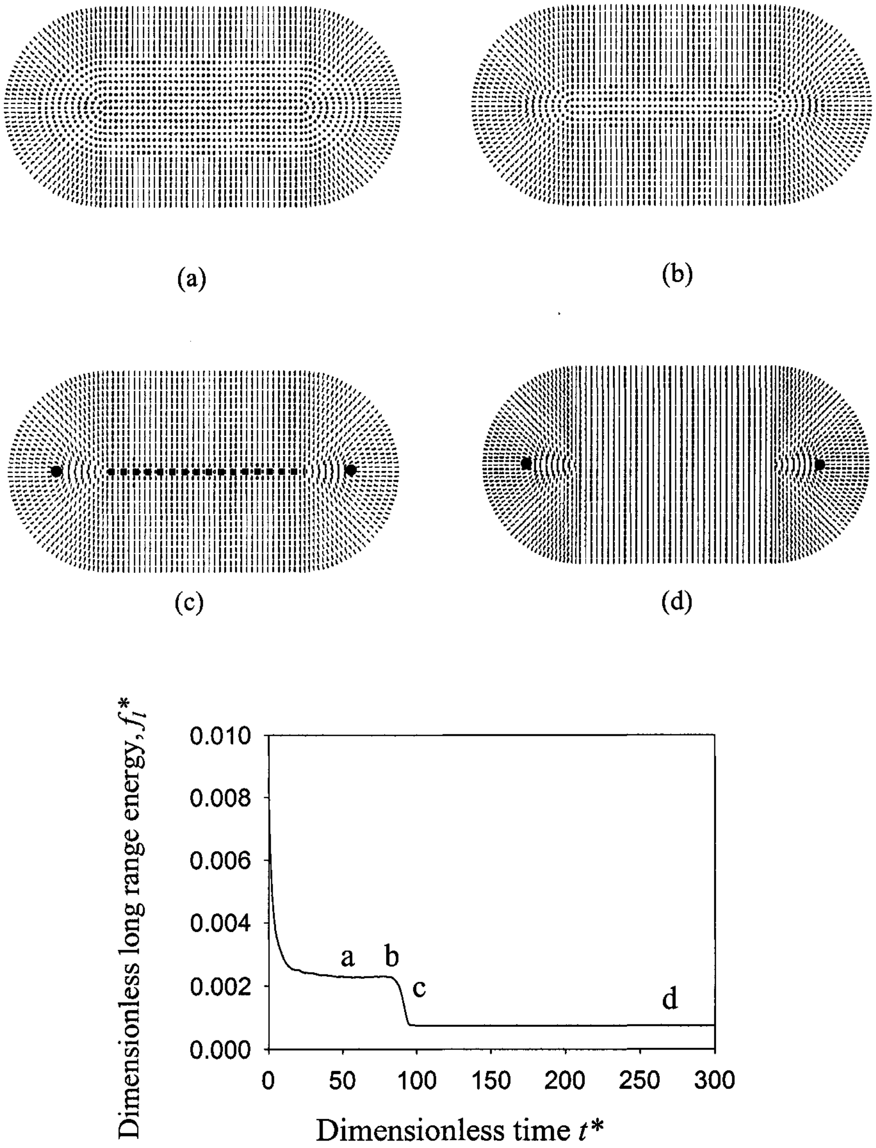

(a) (b)

(c) (d)

Figure 5.7: Formation kinetics and structural evolution of the ribbon planar polar texture, for U=4.55, $\mathcal{R} = 50$, $\tilde{L}_2 = -0.5$, $\tilde{L}_3 = 0$, De=0, and A_r=1. Figure 5.7a-d show visualizations of M as a function of increasing dimensionless time t*: (a). 50, (b) 70, (c) 80, and (d) steady state. The orientation develops as a moving front towards the interior. Figure 5.7e shows the dimensionless long range free energy f_l^* as a function of dimensionless time t*. The energy decreases, until it reaches plateau (corresponding to Fig. 5.7c), and then the residual energy from gradients at the centerline (y*=0) vanishes leading to a homogeneous well-aligned region (corresponding to Fig. 5.7d).

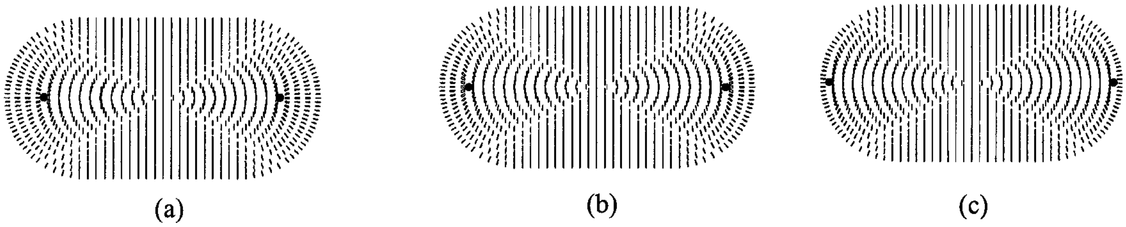

(a) (b) (c)

Figure 5.8: Computed visualizations of the tensor order parameter C of representative steady state RPP textures, for U=4.55, $\mathcal{R}=10$, $\tilde{L}_2=-0.5$, $\tilde{L}_3=0$, A_r=1, for a planar extensional flow, (a) De*=0, (b) De*= 0.03, (c) De*=0.1. The figures show that the effect of elongation is to displace the defects towards the rims of the fiber, and increasing the degree of director orientation along the fiber's long axis.

Figure 5.8 shows computed visualizations of the tensor order parameter **C** of representative steady state RPP textures, for U=4.55, $\mathcal{R}=10$, $\tilde{L}_2=-0.5$, $\tilde{L}_3=0$, A_r=1, for a planar extensional flow, (a) De*=0, (b) De*= 0.03, (c) De*=0.1. The figures shows that the effect of elongation is to displace the defects towards the rims of the fiber, and increasing the degree of director orientation along the fiber's long axis.

In general our model easily selects the RPP texture at low temperatures or when the long range elasticity is significant. The prevalence of the RPP texture is due to the fact that the oriented section in the mid-region is perfectly aligned, and hence has no elastic distortions. The transient texture that leads to the RPP texture has structural features very close to the RPL texture.

5.5.2 Formation and Structure of the Ribbon Planar Radial Texture

As indicated above the RPR texture belongs to the same family as the planar radial texture observed in fibers of circular cross-section. The characteristic feature of these textures is the presence of disclination line of strength s=+1. In our previous work we have found that the planar radial texture appears at higher temperatures [14]. The RPR texture has been observed experimentally [1] by using a converging die. Up-stream of the converging die, the mesophase flows in a capillary geometry, and assuming a radial texture emerges there, the question we wish to address is what will be the effect of geometric transition (circular cross-section → ribbon like cross-section) on the main features of the radial texture. To answer this question we performed a parametric study on the cross-section shape by continuously increasing the aspect ratio A_r from zero to one. For A_r=0 (circular fiber) the initial conditions correspond to the isotropic state, with (S,P) nearly zero, and with randomly oriented (**n**,**m**,**l**) eigenvectors. After achieving steady state, the aspect ratio A_r is increased and a new steady state is achieved. In this way a continuous family of steady state radial textures is generated.

Figure 5.9 shows computed visualizations of the tensor order parameter **C** as a function of aspect ratio, for U=4.55, $\mathcal{R} = 10$, $\tilde{L}_2 = -0.5$, $\tilde{L}_3 = -1.3$, De*=0, A_r=0 (a), 0.5 (b), and 1.0 (c). The figures show that increasing shape anisotropy the disclination line of strength s=+1 remains at the center of the fiber. In addition the pure bend distortion that exists in the circular fiber (Ar=0) becomes a splay-bend distortion in the ribbon shaped fiber (A_r=1). The figures show that the geometric change $A_r = 0 \rightarrow A_r = 1$, produces the textural change $PR \rightarrow RPR$. The orientation features shown in Fig. 5.9c are consistent with experimentally characterized ribbon fibers [1].

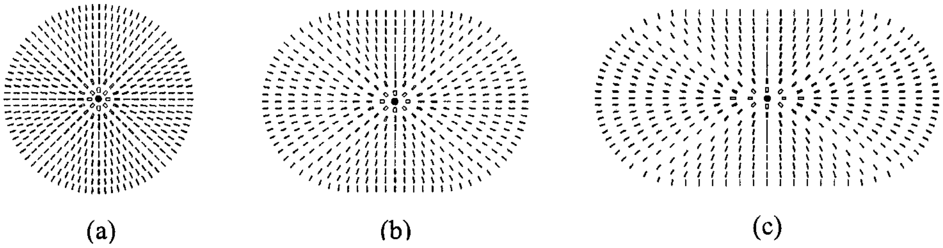

Figure 5.9: Computed visualizations of the tensor order parameter C, for U=4.55, $\mathcal{R} = 10$, $\tilde{L}_2 = -0.5$, $\tilde{L}_3 = -1.3$, De*=0, A_r=0 (a), 0.5 (b), and 1.0 (c). The figures shows that increasing shape anisotropy the disclination line of strength s=+1 remains at the center of the fiber. In addition the pure bend distortion that exist in the circular fiber (A_r=0) becomes a splay-bend distortion in the ribbon shaped fiber (A_r=1). The figures show that the geometric change $A_r = 0 \rightarrow A_r = 1$ produces the textural change $PR \rightarrow RPR$. The orientation features shown in Fig. 5.9c are consistent with experimentally characterized ribbon fibers [1].

5.5.3 Formation and Structure of the Ribbon Planar Line Texture

As mentioned above the main characteristic of the ribbon planar line texture is the presence of a line feature at y*=0, and a strongly oriented bulk, with the director parallel to the long semiaxis (x*) of the ribbon-shaped fiber. Another important feature is that both the x* axis and the y* axis are lines of mirror symmetry. For increasing y*, the director rotates anticlockwise for x*>0 but clockwise for x*<0. The crossing of the two mirror axes and the incompatible direction of director rotation is resolved by a disclination line of strength s=+1. Since all fibers with a disclination line of strength s=+1 belong to the same family, it follows that the ribbon planar line texture belongs to the same family as the planar radial and ribbon planar radial textures. Since the bulk of the texture is strongly oriented along x*, it follows that the RPL texture is the result of a compressive deformation along x*. This compression can appear at the exit of the converging die, since the axial ratio A_r is substantially reduced when going from the die exit to the final fiber shape. Thus we simulate the evolution of the ribbon planar radial texture under the influence of a steady planar elongational flow, to see whether the resulting texture share the experimentally observed features.

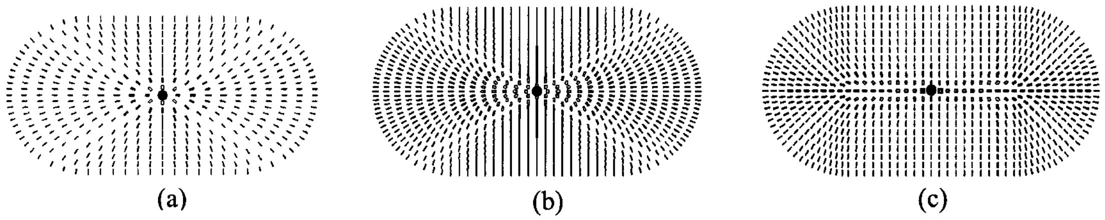
(a) (b) (c)

Figure 5.10: (a) Computed visualization of the tensor order parameter C for the ribbon planar line texture, for U=4.55, $\mathcal{R}=10$, $\tilde{L}_2=-0.5$, $\tilde{L}_3=-1.3$, De*=0 (a), De*=0.03 (b), De*=0.06 (c) and A_r=1, at steady state. The texture was obtained by restricting the director orientation along y*, such that for $x^* \neq 0$ the director is vertical: n=(0,1,0). The effect of planar elongation strength on the structural features of the texture is shown. The smooth homogeneous distortion at low De* becomes localized at greater De*, and if De* is sufficiently large it leads to the line texture. The figure shows a texture in qualitative agreement with experiments. In particular the line feature at y*=0, the sense of rotation in the orientation of the director next to the line, and the strong alignment in the bulk are captured by the simulation.

Figure 5.10 shows computed visualization of the tensor order parameter **C**, for U=4.55, $\mathcal{R}=10$, $\tilde{L}_2=-0.5$, $\tilde{L}_3=-1.3$, U=4.55, $\mathcal{R}=10$, $\tilde{L}_2=-0.5$, $\tilde{L}_3=-1.3$, De*=0 (a), De*=0.03 (b), De*=0.06 (c) and A_r=1, at steady state. The texture was obtained by restricting the director orientation along $y^*=0$ such that the director is vertical: **n**=(0,1,0). The effect of planar elongation strength on the structural features of the texture is shown. The smooth homogeneous distortion at low De* becomes localized at greater De*, and if De* is sufficiently large it leads to the line texture. The figure shows a texture in qualitative agreement with experiments. In particular the line feature at y*=0, the sense of rotation in the orientation of the director next to the line, and the strong alignment in the bulk are captured by the simulation. If the director restriction at y*=0 was not imposed, the texture evolves towards the lower energy ribbon planar polar texture, by the following disclination reaction [15]:

$$s=+1\rightarrow 2s=+1/2 \qquad (37)$$

It should be noted that due to computational limitations the value of $\mathcal{R}=\frac{R}{\xi}$ used in this work is unrealistically low, and hence processes such as disclination reactions, dominated by short energy, have no energy of activation barriers, and hence dominate the texture evolution. In real life $\mathcal{R}=\frac{R}{\xi}>>10^5\text{-}10^6$, and disclinations of s=+1 may persist [15], because the decay into two s=+1/2 disclinations requires a high energy of activation.

The emergence of the inversion walls by subjecting the ribbon planar radial texture to planar elongational flow is another example of inversion wall created by orienting fields commonly observed in other thermotropic rod-like nematic materials [17]. A very transparent view of the structure and characteristics of the inversion wall can be obtained by comparing our computational results) with theoretical results obtained from a simplified version of the model eqn. (18). Since the inversion wall is an orientation process and not a molecular process, we only retain the long range energy contribution. Implementing the following assumptions in eqn. (18):

(a) uniaxial tensor order parameter: $\mathbf{Q}=S_{eq}(\mathbf{nn}-\mathbf{I}/3)$, (b) equal splay and bend constants: L_3=0, (c) steady state: $\partial\mathbf{Q}/\partial t^*=0$, (d) planar director orientation given by: $\mathbf{n}(y^*)=(\cos\theta\,,\sin\theta\,,0)$, (e) planar elongational flow:

$$\mathbf{A}=\dot{\varepsilon}\;\tilde{\mathbf{A}};\qquad \tilde{\mathbf{A}}=\begin{bmatrix}-1 & 0 & 0\\ 0 & 0 & 0\\ 0 & 0 & 1\end{bmatrix} \qquad (38)$$

the governing equation (18) reduces to the following director angle equation:

$$\frac{d^2\theta}{dy^{*2}} + E_e \sin\theta\cos\theta = 0; \qquad E_e = \frac{\gamma_2 \dot{\varepsilon} R_y^2}{K};$$

$$\gamma_2 = -\frac{2\beta\eta S_{eq}}{3}\left(2 + S_{eq} - \frac{S_{eq}^2}{2}\right); \quad K = \left(L_2 + 2L_1\right)S_{eq}^2 \tag{39}$$

where E_e is the Ericksen number or ratio of elongational flow effect to elastic effect on orientation. In terms of (De), the Ericksen number is:

$$E_e = \frac{\gamma_2 \dot{\varepsilon} R_y^2}{K} = -\frac{3}{2\beta} D_e^* \mathcal{R}^2 \left[\frac{\gamma_2}{\eta} \frac{L_1}{\left(L_2 + 2L_1\right)}\right] = D_e^* \mathcal{R}^2 \left\{ S_{eq}\left(2 + S_{eq} - \frac{S_{eq}^2}{2}\right)\left[\frac{1}{\left(\tilde{L}_2 + 2\right)}\right]\right\} \tag{40}$$

The solution to eqn.(39) :

$$\tan\left(\frac{\theta}{2}\right) = \exp\left(-y^* \sqrt{E_e}\right) \tag{41}$$

describes a splay-bend inversion wall produced by the planar elongational flow. For y*>0 and far from the wall the director angle is $\theta=0$, while for y*<0 and far from the wall the director angle is $\theta = \pi$ (this corresponds to the x*<0 section). As y* increases the director rotates clockwise and all the rotation is concentrated across the thickness of the wall d*:

$$d^* = \frac{2}{\sqrt{E_e}} \tag{42}$$

The mirror image solution where the director rotates anti-clockwise (this corresponds to the x*>0 section), when traversing the inversion wall is given by:

$$\tan\left(\frac{\pi - \theta}{2}\right) = \exp\left(-y^* \sqrt{E_e}\right) \tag{43}$$

Figure 5.11a shows the computed director angle θ as a function of dimensionless distance y*, for U=4.55, $\mathcal{R} = 15$, $\tilde{L}_2 = -0.5$, $\tilde{L}_3 = 0$, A_r=1, De*=0.06 (E_e=16.6), for three values of the x* coordinates, using the full tensor order model eqns.(18). The figure shows that as x* decreases (closer to the bounding surface at x*=-(R_x*+R_y*)) the wall thickness increases because of the boundary effect. The structure of the inversion wall is clear; all the director rotation occurs within a small region of thickness $d^*=2/(E_e)^{0.5}=2\times0.24$, and the rotation is clockwise. The mirror symmetric solution is not shown. Figure 5.11b shows the analytical solutions given by eqn. (43), for E_e=5, 10, and 20, where the effect of increasing E_e on the wall thickness is clearly shown. The figures show that the 2D steady state computational solution of the tensor order parameter **Q**(x*,y*) agrees very well with the 1D analytical solution. The small differences between computed and theoretical solutions are due to the y* dependence of the **Q** solutions.

Figure 5.12 shows a summary of the computed results in terms of computed visualizations of the tensor order parameter. The left column corresponds to higher temperatures and to the family of radial textures, while the left corresponds to lower temperatures and to the family of polar textures. The left column shows that the circle to ribbon transformation distorts the texture and creates splay distortions, but the disclination line remains at the center. A subsequent planar elongational flow creates two mirror image inversion walls that meet at the disclination. The thickness of the wall decreases with increasing elongation rate. The texture transformation cascade is:

$$\text{planar radial}\,(\text{RP}) \overset{\text{geometry}}{\rightarrow} \text{ribbon planar radial}\,(\text{RP}) \overset{\text{flow}}{\rightarrow} \text{ribbon planar line}\,(\text{RPL}) \qquad (44)$$

At lower temperatures the selected family is the planar polar texture. Geometrical deformations increase the alignned center-region, while the imposition of planar elongation flow move the defects towards the bounding surfaces. The texture transformation cascade is:

$$\text{planar polar}\,(\text{PP}) \overset{\text{geometry}}{\rightarrow} \text{ribbon planar polar}(\text{RPP}) \overset{\text{flow}}{\rightarrow} \text{ribbon planar polar}\,(\text{RPP}) \qquad (45)$$

Finally, our model also predicts the ribbon planar radial – ribbon planar polar transition, but as mentioned above this is due to the low value of $\mathcal{R}$ used in the simulations, as imposed by computational limitations. Under realistic higher values the transition may not occur, because of the high energy of activation required.

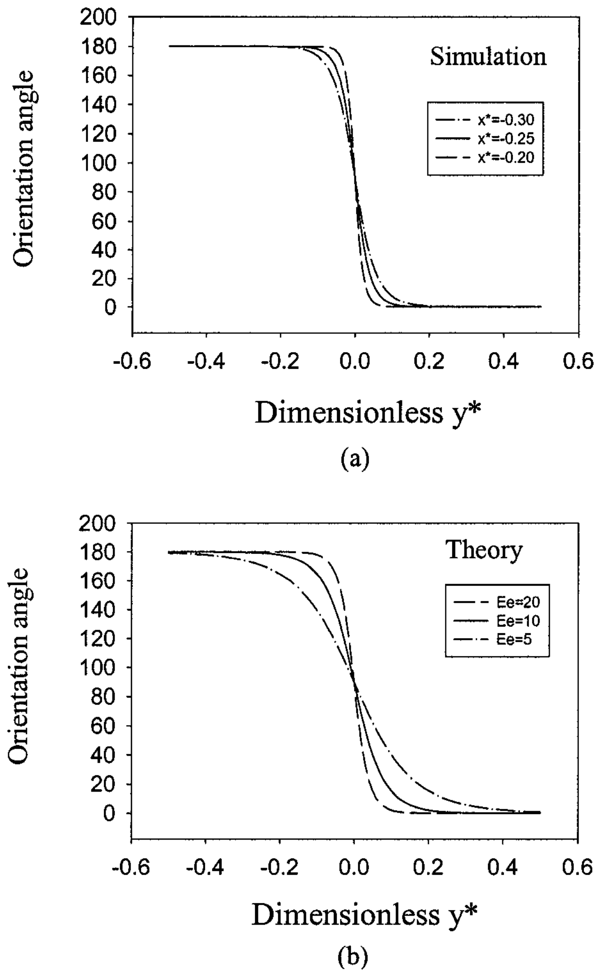

Figure 5.11: (a) Computed director angle θ as a function of dimensionless distance y*, for U=4.55, $\mathcal{R} = 15$, $\tilde{L}_2 = -0.5$, $\tilde{L}_3 = 0$, A_r=1, De*=0.06 (E_e=16.6), for three values of the x* coordinates, using the full tensor order model eqns. (18). The figure shows that as x* decreases (closer to the bounding surface at x*=-(R_x*+R_y*)) the wall thickness increases because of the boundary effect. The structure of the wall is clear; all the director rotation occurs within a small region of thickness d*=2/(E_e)$^{0.5}$=2×0.24, and the rotation is clockwise. The mirror symmetric solution is not shown. Figure 5.11b shows the analytical solutions given by eqn. (43), for E_e=5, 10, and 20, where the effect of increasing E_e on the wall thickness is clearly shown. The figures show that the 2D steady state computational solution of the tensor order parameter **Q** (x*, y*) agrees very well with the 1D analytical solution.

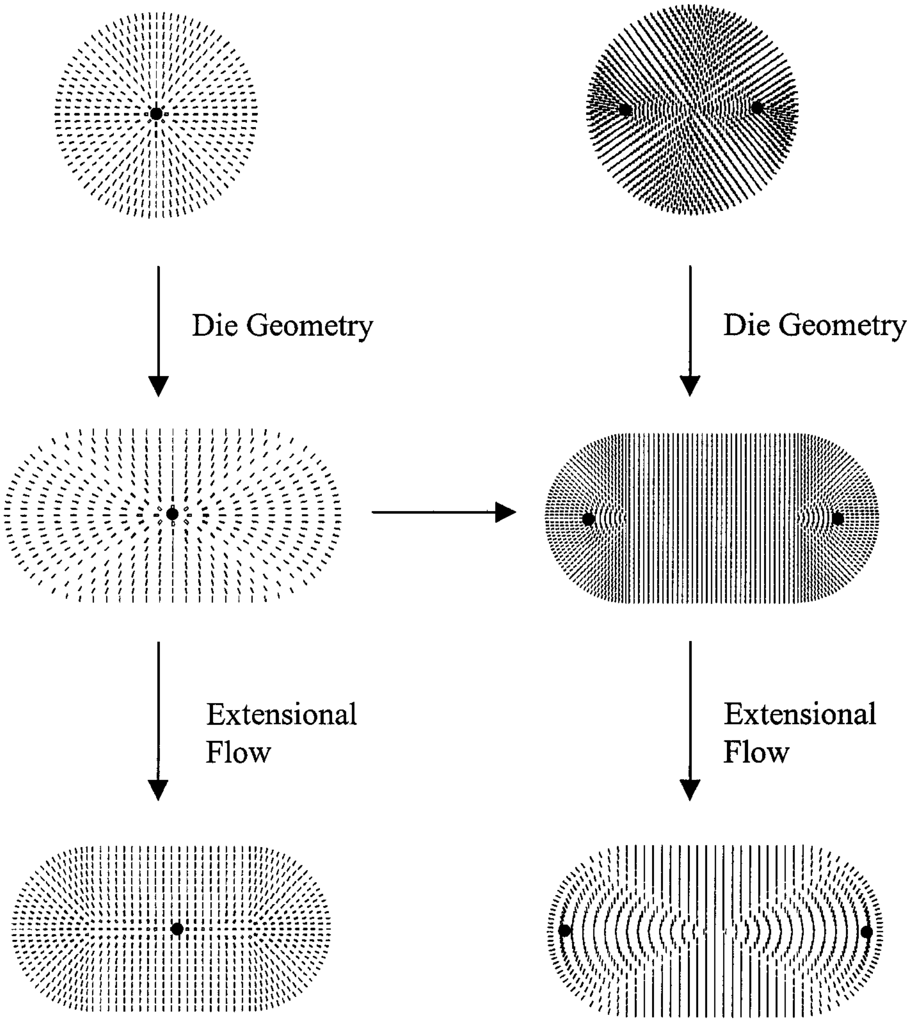

Figure 5.12: Geometry and flow-induced textural transformation. The left column corresponds to higher temperatures and to the family of radial textures, while the left corresponds to lower temperatures and to the family of polar textures. The left column shows circle to ribbon transformation, distorts the texture and creates splay distortions, but the disclination line remains at the center. A subsequent planar elongational flow creates two mirror image inversion walls that meet at the disclination. The texture transformation cascade is:

$$\text{planar radial}\,(\text{RP}) \overset{\text{geometry}}{\rightarrow} \text{ribbon planar radial}\,(\text{RP}) \overset{\text{flow}}{\rightarrow} \text{ribbon planar line}\,(\text{RPL})$$

At lower temperatures the selected family is the planar polar texture. Geometrical deformations increase the aligned center-region, while the imposition of planar elongation flow moves the defects towards the bounding surfaces. The texture transformation cascade is:

$$\text{planar polar}\,(\text{PP}) \overset{\text{geometry}}{\rightarrow} \text{ribbon planar polar}(\text{RPP}) \overset{\text{flow}}{\rightarrow} \text{ribbon planar polar}\,(\text{RPP})$$

Conclusions

A model to describe the texture formation in mesophase carbon fibers of ribbon shape cross-section has been developed, implemented, and shown to replicate commonly observed cross-sectional carbon fiber textures of industrial relevance. The model is based on the classical Landau-de Gennes theory for liquid crystals and has been adapted to describe discotic carbonaceous mesophases. The model is able to predict the formation of ribbon planar radial, ribbon planar polar textures, and ribbon planar line texture. Higher temperatures tend to select radial textures, characterized by a disclination line of strength $s=+1$. Lower temperatures tend to select polar textures, characterized by two disclinations of strength $s=+1/2$. Cross-section shape distortions from a circle towards a ribbon do not change the essential nature of the texture but distort the orientation. Thus the planar radial texture becomes the ribbon planar radial texture, while the planar polar texture becomes the ribbon polar texture. The effect of planar elongational flow on ribbon textures has been characterized. Subjecting a ribbon planar radial texture to elongational flow produces the ribbon planar line texture, whose distinguishing feature is the presence of two inversion walls along the mid-plane. On traversing the inversion walls, the director rotates by π radians. These localized distortions frequently arise in other liquid crystalline materials when subjected to strong orienting fields, and the visual traits of the ribbon line texture in carbonaceous mesophase fibers [1] is virtually identical to that of a liquid crystal polyether subjected to a magnetic field [20]. The computed solutions of the line texture are shown to be in agreement with analytical solutions. Subjecting a ribbon planar polar textures to planar elongation flow only increases the distance of the two defects but does not produce any line feature.

The computational and theoretical results characterize the main elastic and flow effects on ribbon-like mesophase fibers and shed new light on how to control and optimize texture selection mechanisms of interest to the industrial production of carbon fibers.

Acknowledgement

This grant is supported by a grant from the Donors of The Petroleum Research Fund (PRF) administered by the American Chemical Society.

Bibliography

[1] Edie D.D., Robinson K.E., Fleurot O., Jones S.P. and Fain C.C., 1994, *Carbon*, **32**(6), 1045; Robinson K.E. and Edie D.D., 1996, *Carbon*, **34**(1), 13..

[2] McHugh J.J., 1994, *Ph.D Thesis,* Clemson University.

[3] Hurt R.H. and Chen Z.Y., 2000, *Physics Today,* **March,** 39..

[4] Peebles L.H. Jr., 1995, *Carbon Fibers-Formation, Structure, and Properties*, (Boca Raton, FL: CRC).

[5] Beris A.N. and Edwards B.J., 1994, *Thermodynamics of flowing systems,* (Oxford: Claredon).

[6] Sokalski K. and Ruijgrok T.W., 1982, *Physica,* **113A,** 126.

[7] Osipov M.A. and Hess S., 1993, *Molecular Physics*, **78**, No. 5, 1991.

[8] Ho A.S.K. and Rey A.D, 1991, *Rheologica Acta*, **30**, 77.

[9] Farhoudi Y. and Rey A.D., 1993, *Rheologica Acta*, **32**, 207.

[10] Singh A.P., Rey A.D., 2000, *Journal of Non-Newtonian Fluid Mechanics*, **94**, 87.

[11] Singh A.P. and Rey A.D., 1999, *Liquid Crystals*, **26**, 999.

[12] Morrison F.A., 2001, *Understanding Rheology*, Oxford University Press, New York.

[13] Rey A.D., 1990, *J. of Rheology*, **34**, 425.

[14] Yan J., Rey A.D., 2001, *Physical Review E*, submitted.

[15] Zimmer J.E. and White J.L., 1983, *Advances in Liquid Crystals*, **5**, 157.

[16] De Gennes P.G. and Prost J., 1993, *The Physics of Liquid Crystal 2nd edn*, Oxford: Clarendon.

[17] Chandrasekhar S., 1992, *Liquid Crystals 2nd edn ,* Cambridge University Press.

[18] Yan J., Rey A.D., 2001, *Modeling and Simulation in Materials Science and Engineering*, submitted.

[19] Rey A.D., 1990, *Liquid Crystals*, **7**(3), 315.

[20] O'Rourke M.J.E., Ding D.K., Thomas E.L., 2001, *Macromolecules*, **34**, 6658.

[21] Bharadwaj R.K., Bunning T.J. and Farmer B.L., 2000, *Liquid Crystals*, **27**(5), 591.

[22] Tsuji T., and Rey A.D., 1998, *Macromolecular Theory and Simulation*, **7**, 623.

[23] Tsuji T., and Rey A.D., 2000, *Phys. Rev. E*, **62**,8141.

[24] Wang L. and Rey A.D., 1997, *Theory and Simulation in Material Science and Engineering*, **5**, 67.

[25] Rey A.D., 1995, *Phys. Rev. E.*, **51**, 6278.

[26] Singh A.P., 2000, *Ph.D Thesis,* Mcgill University.

[27] Longa L., Monselesan D. and Trebin H.R., 1987, *Liquid Crystals,* **2**(6), 769.

[28] Berreman D.W. and Meiboom S., 1984, *Physical Review A*, **30**(6), 1955.

[29] Schiele K. and Trimper S., 1983, *Phys. Stat. Sol. (b),* **118**, 267.

[30] Doi M. and Edwards B.J., 1986, *The Theory of Polymer Dynamics,* Oxford: Clarendon.

[31] Press W.H., Teukolsky S.A., Vetterling W.T., and Flannery B.P., 1992, *Numerical Recipes in Fortran 77, The Art of Scientific Computing, 2nd edition*, Cambridge University Press.

[32] Rey A.D. and Denn M.M., 1988, *J. Non-Newt. Fluid Mechanics*, **27**, 375.

Chapter 6

Conclusions

A model to describe the texture formation in mesophase carbon fibers of circular and ribbon shaped cross-sections has been formulated, solved, and validated with available experimental/industrial data. The simulations replicate commonly observed cross-sectional carbon fiber textures of industrial relevance. The model is based on the classical Landau-de Gennes theory for anisotropic textured viscoelastic liquid crystals and has been adapted to describe discotic carbonaceous mesophases.

For cylindrical fibers, the model is able to predict the formation of planar radial and planar polar textures. The parametric conditions of their stability in terms of temperature and fiber radius have been computed. Lower temperature and thicker fibers tend to select the planar polar texture and higher temperature and thin fibers tend to promote the emergence of the planar radial texture, in agreement with experiments. A geometric analysis of the planar polar texture has been performed and the defect separation distance is shown to be equal to $1/\sqrt[4]{5}$ under elastic isotropy. Computational modeling of texture formation shows that the two defects in the planar polar texture arise from a topological transformation that involves the decay of a +1 defect into two +1/2 defects. The numerical results show that the computed defect separation distance is consistent with the theoretical results, for different fiber radius and temperatures. Furthermore, The influence of elastic anisotropy to the fiber texture formation is thoroughly characterized. It is found that splay-bend anisotropy influences the fiber texture much more than the twist term. Splay (bend) avoidance leads to the planar radial (polar) texture. The importance of splay-bend anisotropy is completely explained by the Frank elastic theory.

The model is able to predict the formation of ribbon planar radial, ribbon planar polar, and ribbon planar line textures. Higher temperatures tend to select radial textures, characterized by a disclination line of strength s=+1. Lower temperatures tend to select polar textures, characterized by two disclinations of strength s=+1/2. Cross-section shape distortions from a circle towards a ribbon do not change the essential nature of the texture but distort the orientation. Thus under a circle-to-ribbon shape transformation the planar radial texture transforms into the ribbon planar radial texture, while the planar polar texture transforms into the ribbon polar texture. The effect of planar elongational flow on ribbon textures has been characterized. Subjecting a ribbon planar radial texture to elongational flow produces the ribbon planar line texture, whose distinguishing feature is the presence of two inversion walls along the mid-plane. On traversing the inversion walls, the director rotates by π radians. These localized distortions frequently arise in other liquid crystalline materials when subjected to strong orienting fields, and the visual traits of the ribbon line texture in carbonaceous mesophase fibers is virtually identical to that of a liquid crystal polyester subjected to a magnetic field. The computed solutions of the line texture are shown to be in agreement with analytical solutions. Subjecting a ribbon planar polar textures to planar elongation flow only increases the distance of the two defects but does not produce any line feature.

The computational and theoretical results presented in this thesis characterize the main mechanisms that control texture selection in mesophase fibers of circular and ribbon shapes, and hence provide new knowledge on how to control and optimize texture selection mechanisms of interest to the industrial production of carbon fibers.